



**AN ANALYSIS OF MULTIPLE CONFIGURATIONS OF NEXT-GENERATION
CATHODES IN A LOW POWER HALL THRUSTER**

THESIS

John E. Rotter, Lieutenant Commander, USN

AFIT/GA/ENY/09-M07

**DEPARTMENT OF THE AIR FORCE
AIR UNIVERSITY**

AIR FORCE INSTITUTE OF TECHNOLOGY

Wright-Patterson Air Force Base, Ohio

APPROVED FOR PUBLIC RELEASE; DISTRIBUTION UNLIMITED

The views expressed in this thesis are those of the author and do not reflect the official policy or position of the United States Air Force, Department of Defense, or the U.S. Government.

AFIT/GA/ENY/09-M07

**AN ANALYSIS OF MULTIPLE CONFIGURATIONS OF NEXT-GENERATION
CATHODES IN A LOW POWER HALL THRUSTER**

THESIS

Presented to the Faculty

Department of Aeronautics and Astronautics

Graduate School of Engineering and Management

Air Force Institute of Technology

Air University

Air Education and Training Command

In Partial Fulfillment of the Requirements for the
Degree of Master of Science in Astronautical Engineering

John E. Rotter, BS

Lieutenant Commander, USN

March 2009

APPROVED FOR PUBLIC RELEASE; DISTRIBUTION UNLIMITED


AFIT/GA/ENY/09-M07

**AN ANALYSIS OF MULTIPLE CONFIGURATIONS OF NEXT-GENERATION
CATHODES IN A LOW POWER HALL THRUSTER**

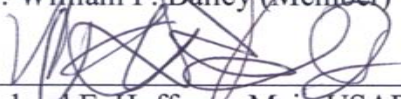
John E. Rotter, BS


Lieutenant Commander, USN

Approved:


Richard D. Branam, Lt. Col., USAF (Chairman)


Dr. William F. Bailey (Member)


Richard E. Huffman, Maj., USAF (Member)


Dr. William A. Hargus Jr. (Member)

6 Mar 09
Date

6 Mar 09
Date

5 Mar 09
Date

5 Mar 09
Date

Abstract

The research presented here is an effort to integrate an existing hollow cathode design with a low power production Hall thruster in multiple geometries. Both externally- and internally-mounted cathodes were fabricated and operated in conjunction with a Busek BHT-1500 Hall thruster. Three insert materials were evaluated; Cerium Hexaboride (CeB_6), Lanthanum Hexaboride (LaB_6), and impregnated tungsten. The thruster was operated at a single operating condition for all testing. The operating specifications for the discharge were 300 V and 2.25 A, giving a total power of 675 W.

The boride-based cathodes were tested in both geometries while the tungsten-based cathode was only tested in an external configuration. A Faraday probe was used to measure current density in the plume and a single Langmuir probe was used to characterize the plasma. The charge state of the ions was measured with an ExB probe. All assembly and testing occurred at the Air Force Institute of Technology's (AFIT) Space Propulsion Analysis and System Simulation (SPASS) lab facility.

The thruster's performance with the externally-mounted boride-based cathodes installed demonstrated the highest levels of efficiency and performance. The thruster's performance with the tungsten-based cathode installed was slightly less than with the externally-mounted boride-based cathodes. The lowest thruster performance occurred with the internally-mounted cathodes installed. The primary loss mechanism observed was an increase in multiply-ionized propellant with the internally-mounted cathodes.

Acknowledgments

I must first thank God for the grace He has shown me in this very challenging and rewarding endeavor. I have learned much about electric propulsion and have become a firm believer in the opportunities it presents. For his guidance and support, I would like to thank LtCol Richard Branam, my thesis advisor, whose trust in me was both confidence inspiring and, at times, scary. His enthusiasm and flexibility have brought this work to fruition. For their willingness to always be on call, Dr. John Williams and Dr. Casey Farnell have my utmost gratitude and respect. They helped build, install, and troubleshoot our beam profiler, without which this work would have much less substance. The team of lab technicians led by Jay Anderson; John Hixenbaugh, Wilbur Lacy, Barry Page, and Chris Zickefoose provided outstanding support and guidance whenever it was needed. For his outstanding technical support, Bruce Pote of Busek deserves much credit for helping us through the growing pains of thruster development and testing. Despite the distance from here to Edwards AFB, Dr. William Hargus always made sure we had what we needed to conduct our research. Thanks also Dr. Glen Perram of the AFIT Physics Department for allowing me to use their Langmuir probe. For journeying with me, I thank Capt Bryan Morgan and Garret Willis, my fellow SPASS lab warriors, whose encouragement and suggestions were always welcome. A special thanks too, to 1st Lt Dustin Warner whose work I built upon and who was always there to answer my questions as they came up. I must thank my parents, especially my dad, who, along with his siblings, have fostered in me a love of science and engineering and a desire to “get my hands dirty” while advancing knowledge. Finally, I cannot begin to express to my wife the gratitude that she deserves. She has spent the last 18 months supporting my efforts here at AFIT; during which time we have had two of our three children and she completed her master’s degree. There is no way I would have accomplished as much as I have without her unfathomable support.

John E. Rotter

Table of Contents

	Page
Abstract	iv
Acknowledgments	v
Table of Contents	vi
List of Figures	ix
List of Tables	xv
I. Introduction	16
Motivation	16
Problem Statement	18
Research Objectives	19
Research Focus	19
Investigative Questions	20
II. Literature Review	22
Hall Thruster Applications	22
Hall Thruster Theory of Operation	25
Cathode Technology	28
Hollow Cathode Theory of Operation	32
Cathode Insert Materials	34
Center-Mounted Cathode Studies	37
Experimental Considerations	38
Performance Measurement and Plasma Diagnostics	40
Efficiency Determination	41

	Page
III. Methodology	45
Vacuum Facility	45
Test Assembly	49
Hall Thruster.....	51
Hollow Cathode Assembly.....	54
Data Acquisition and Measurement Equipment.....	61
Langmuir Probe	62
Beam Profiler.....	67
Faraday Probe.....	68
ExB Probe.....	70
Hall Thruster and Cathode Operation Test Points.....	73
IV. Analysis and Results.....	78
Thruster-Cathode Integration	78
Thruster Operation.....	79
Steady-State Power Consumption	81
Faraday Probe Analysis.....	83
Langmuir Probe Analysis.....	100
ExB Probe Analysis.....	116
V. Conclusions and Recommendations	124
Conclusions of Research	124
Recommendations for Future Research.....	127

	Page
Appendix A. Thruster Operating Procedures.....	129
Appendix B. Faraday Probe Data	132
Appendix C. Langmuir Probe Data	137
Appendix D. ExB Probe Data.....	140
Vita	149

List of Figures

	Page
Figure 1. NASA NSTAR Ion Thruster [4].....	17
Figure 2. Fakel SPT-100 Hall Thruster [7]	18
Figure 3. Schematic of a Hall thruster showing both internally and externally mounted cathode configurations. [10].....	27
Figure 4. Tungsten filament cathode and LaB ₆ single crystal emitter. [29]	29
Figure 5. Hollow Cathode Schematic [9]	31
Figure 6. SPASS lab vacuum chamber and associated components.	46
Figure 7. Screenshot of VacuumPlus software.	48
Figure 8. Photo showing thruster, pointing vertically, along with truss structure and Aerotech® translation stages.	49
Figure 9. PPU and power supplies used to power thruster and cathode.	51
Figure 10. The BHT-1500-C Hall thruster. [50].....	53
Figure 11. Screenshot of BPU-600 Host Simulator, version 4.	54
Figure 12. Hollow Cathode Assembly.....	55
Figure 13. Cathode Inserts: a. LaB ₆ , b. CeB ₆ , c. impregnated Tungsten.....	56
Figure 14. Molybdenum cathode tube (long) and mounting flange.	57
Figure 15. Assembled (long) cathode tube with heater wire installed.....	58
Figure 16. Cathode tube (short) with heater wire and tantalum foil, mounted to base plate	58
Figure 17. Cathode keepers; short and long.....	59

	Page
Figure 18. Parts breakdown for cathodes—keeper and cathode tubes for both long and short cathodes shown.	60
Figure 19. Assembled Cathode (short)	60
Figure 20. Electrical schematic of thruster and cathode.	61
Figure 21. Installed Langmuir probe and Busek BHT-1500-C Hall thruster.	62
Figure 22. I-V Characteristic Curve.....	64
Figure 23. Spatial data collection points (edge-mounted cathode).....	67
Figure 24. Faraday probe and schematic. [59].....	69
Figure 25. Faraday probe data acquisition setup.	70
Figure 26. ExB probe with cover removed. [60]	71
Figure 27. Schematic of ExB probe. [60]	72
Figure 28. ExB data collection scheme.....	73
Figure 29. BHT-1500-C thruster with two edge-mounted cathodes installed.	74
Figure 30. BHT-1500-C thruster with single edge-mounted cathode installed.	75
Figure 31. BHT-1500-C thruster with center-mounted cathode installed.	76
Figure 32. BHT-1500-C operating with externally-mounted cathode.....	80
Figure 33. Current Density at 70 cm Axial Distance.....	84
Figure 34. Current Density at 60 cm Axial Distance.....	85
Figure 35. Current Density at 50 cm Axial Distance.....	85
Figure 36. Current Density with Externally-Mounted Cathodes at 70 cm Axial Distance	87

Figure 37. Current Density with Externally-Mounted Cathodes at 60 cm Axial Distance	87
Figure 38. Current Density with Externally-Mounted Cathodes at 50 cm Axial Distance	88
Figure 39. Current Density with Internally-Mounted Cathodes at 60 cm Axial Distance	89
Figure 40. Current Density with CeB ₆ cathode at 70 cm Axial Distance	90
Figure 41. Current Density with CeB ₆ cathode at 60 cm Axial Distance	91
Figure 42. Current Density with CeB ₆ cathode at 50 cm Axial Distance	91
Figure 43. Current Density with LaB ₆ cathode at 70 cm Axial Distance	92
Figure 44. Current Density with LaB ₆ cathode at 60 cm Axial Distance	93
Figure 45. Current Density with LaB ₆ cathode at 50 cm Axial Distance	93
Figure 46. Total Beam Current vs. Axial Distance for Externally-Mounted CeB ₆	95
Figure 47. Total Beam Current vs. Axial Distance for Internally-Mounted CeB ₆	95
Figure 48. FWHM Plume Angle for Externally-Mounted CeB ₆	97
Figure 49. FWHM Plume Angle for Externally-Mounted LaB ₆	97
Figure 50. FWHM Plume Angle for Externally-Mounted Tungsten	98
Figure 51. FWHM Plume Angle for Internally-Mounted CeB ₆	98
Figure 52. FWHM Plume Angle for Internally-Mounted LaB ₆	99
Figure 53. Plasma Potential at 15 cm Axial Distance	101
Figure 54. Plasma Potential at 30 cm Axial Distance	102
Figure 55. Plasma Potential at 50 cm Axial Distance	103

	Page
Figure 56. Average Beam Potential	104
Figure 57. Average Beam Velocity versus Axial Distance	105
Figure 58. Total Ion Count versus Axial Distance	106
Figure 59. Ions/sr versus Axial Distance	107
Figure 60. Ion Number Density at 15 cm Axial Distance.....	108
Figure 61. Ion Number Density at 30 cm Axial Distance.....	109
Figure 62. Ion Number Density at 50 cm Axial Distance.....	109
Figure 63. Ion Number Density with Externally-Mounted Cathodes at 15 cm Axial Distance.....	110
Figure 64. Ion Number Density with Externally-Mounted Cathodes at 50 cm Axial Distance.....	111
Figure 65. Ion Number Density with Internally-Mounted Cathodes at 50 cm Axial Distance.....	112
Figure 66. Ion Number Density with CeB ₆ cathode at 15 cm Axial Distance.....	113
Figure 67. Ion Number Density with LaB ₆ cathode at 15 cm Axial Distance.....	113
Figure 68. Ion Number Density with CeB ₆ cathode at 50 cm Axial Distance.....	114
Figure 69. Ion Number Density with LaB ₆ cathode at 50 cm Axial Distance.....	114
Figure 70. Ion Number Density Profile with Externally-Mounted CeB ₆ cathode	115
Figure 71. Ion Number Density Profile with Internally-Mounted CeB ₆ cathode	116
Figure 72. ExB Data for Externally-Mounted CeB ₆	117
Figure 73. ExB Data for Externally-Mounted LaB ₆	118

	Page
Figure 74. ExB Data for Externally-Mounted Tungsten	118
Figure 75. ExB Data for Internally-Mounted Cathodes.....	119
Figure 76. Normalized ExB Data for CeB ₆	120
Figure 77. Normalized ExB Data for LaB ₆	121
Figure 78. Current Density for Externally-Mounted CeB ₆	132
Figure 79. Current Density for Externally-Mounted LaB ₆	132
Figure 80. Current Density for Externally-Mounted Tungsten	133
Figure 81. Current Density for Internally-Mounted CeB ₆	133
Figure 82. Current Density for Internally-Mounted LaB ₆	134
Figure 83. Total Beam Current vs. Axial Distance for Externally-Mounted LaB ₆	134
Figure 84. Total Beam Current vs. Axial Distance for Externally-Mounted Tungsten..	135
Figure 85. Total Beam Current vs. Axial Distance for Internally-Mounted LaB ₆	135
Figure 86. Current Density with Internally-Mounted Cathodes at 70 cm Axial Distance	136
Figure 87. Current Density with Internally-Mounted Cathodes at 50 cm Axial Distance	136
Figure 88. Ion Number Density with Externally-Mounted Cathodes at 30 cm Axial Distance.....	137
Figure 89. Ion Number Density with Internally-Mounted Cathodes at 15 cm Axial Distance.....	137

	Page
Figure 90. Ion Number Density with Internally-Mounted Cathodes at 30 cm Axial Distance.....	138
Figure 91. Ion Number Density with CeB ₆ cathode at 30 cm Axial Distance.....	138
Figure 92. Ion Number Density with LaB ₆ cathode at 30 cm Axial Distance.....	139
Figure 93. Cathode Side ExB Data for Externally-Mounted Cases.....	140
Figure 94. Opposite Side ExB Data for Externally-Mounted Cases	140

List of Tables

	Page
Table 1. Component and total power consumption for each test case.....	82
Table 2. Integrated Beam Current (Amps)	96
Table 3. FWHM Plume Angles (degrees).....	99
Table 4. Beam Voltage (V), Efficiency, and Velocity.....	105
Table 5. Ion Species Fractions	122
Table 6. Ion Velocity (km/s) for Externally-Mounted Cathodes	123
Table 7. Ion Velocity (km/s) for Internally-Mounted Cathodes	123
Table 8. Efficiency and Performance Results	124
Table 9. Ion Generation Potential (V) for Externally-Mounted Cathodes.....	141
Table 10. Ion Generation Potential (V) for Internally-Mounted Cathodes.....	141

AN ANALYSIS OF MULTIPLE CONFIGURATIONS OF NEXT-GENERATION CATHODES IN A LOW POWER HALL THRUSTER

I. Introduction

Motivation

In any engineering endeavor, greater efficiency and performance are always desirable. The goals of greater efficiency and performance are magnified in the realm of rocket propulsion, as the cost of placing a spacecraft in orbit is quite expensive. Any increase in the efficiency or performance of a propulsion system should allow the payload or mission mass to increase as well. The goal of the Integrated High Payoff Rocket Propulsion Technology Program (IHRPT), which began its execution phase in 1996, has been to improve U.S. rocket technology, doubling its performance by 2010. [1] The goals of the IHRPT Program include booster and orbit transfer applications as well as spacecraft propulsion applications. Booster applications are exclusively in the realm of chemical propulsion and while alternative propulsion technologies are being evaluated for orbit transfer applications, they are still primarily affected by chemical rocket technologies. In-space propulsion, however, allows us to venture beyond the realm of the chemical rocket.

Electric Propulsion (EP) has shown much promise in achieving the goals set forth by the IHRPT Program. While EP has been in use for decades, its use today has been highlighted by the achievements of several noteworthy missions. NASA's Deep Space 1 (DS1) mission provided the technology validation for the NASA Solar electric propulsion Technology Applications Readiness Project (NSTAR). [2] DS1 carried an ion engine

based EP system utilizing xenon as a propellant. A nearly identical system is installed aboard NASA's DAWN spacecraft whose mission is still underway. [3]



Figure 1. NASA NSTAR Ion Thruster [4]

Aboard Earth-orbiting satellites, a propulsion system is needed to allow for orbital maneuvering and station keeping. In the case of geostationary satellites, ever more precise station keeping is desired to enable the number of satellites occupying the geostationary belt to increase without risk of a collision. EP, specifically Hall thrusters, provides a low-thrust and very efficient solution to satisfy the needs of Earth-orbiting satellites. Russia has been flying Hall thruster systems for nearly 30 years. Today, the Russian SPT-100 Hall thruster, manufactured by Fakel, has flown aboard numerous western satellites. [5] The first U.S. company to build a Hall thruster to be flight qualified was Busek. Their BHT-200, a 200 W Hall thruster, was flown aboard the Air Force's TacSat-2, which launched in December 2006. [6] The research continues, updating existing designs and developing new ones, to improve both the efficiency and performance of EP systems.

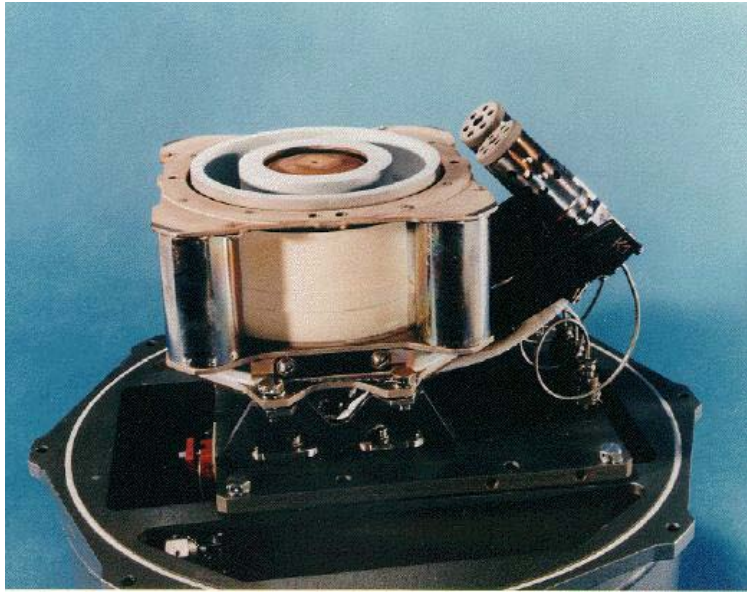


Figure 2. Fakel SPT-100 Hall Thruster [7]

Problem Statement

Most hollow cathode designs for space propulsion in use today utilize a tungsten-based impregnated emitter which is highly susceptible to poisoning. Poisoning from water vapor or oxygen can seriously degrade the performance of these types of emitters. Another limiting factor for impregnated emitters is their lifetime, governed by the rate at which the impregnate evaporates. In a high-current application, the lifetime of an emitter is considerably shorter than in low-current applications.

Both the SPT-100 and BHT-200 mentioned above utilize an external cathode for electron production. Since both of these thrusters are relatively compact, this generally poses no major integration issues. As Hall thrusters increase in size, however, the overall form factor of the thruster becomes increasingly important. Any real estate on a satellite bus utilized by a Hall thruster system cannot be used for other necessary subsystems such as thermal, power, or communications. The Hall thruster's plume divergence is another

issue that must be carefully evaluated when a Hall thruster system is being integrated into a satellite. It is highly undesirable to have high energy particles from the thruster's exhaust plume striking solar arrays, communications antennas, or the satellite bus itself. Thruster plume symmetry and divergence need to be evaluated as the scale of the thruster increases.

Research Objectives

The objectives of this research are to integrate an existing low-current cathode design into a low-power production Hall thruster. Additionally, two geometries for cathode placement and three insert materials are evaluated to determine the combination of geometry and emitter material that delivers the best thruster efficiency for a specified operating condition.

Research Focus

This research seeks to quantify the differences in the performance of a Hall thruster, operating at a specified condition, depending on the cathode emitter material and cathode geometry. The centerpiece of this research was a Busek BHT-1500 Hall thruster. The thruster has been modified by Busek to accept a center-mounted cathode of a low-current design. The cathode design, referred to as a hollow cathode owing to its tube-like geometry, is based on the Goebel and Watkins design developed at the Jet Propulsion Labs. [8] The emitters installed in the hollow cathodes included Lanthanum Hexaboride (LaB_6), Cerium Hexaboride (CeB_6), and Barium Oxide (BaO) impregnated tungsten emitters. Both LaB_6 and CeB_6 are desirable as emitters in a hollow cathode design due to their resistance to poisoning. There has been research done on cathodes utilizing LaB_6 ,

but virtually no research exists on the feasibility of CeB_6 as an emitter for hollow cathode applications. [9]

To minimize the number of variables, a single operating condition was selected for both the BHT-1500 Hall thruster and for the cathodes being evaluated. In addition to the multiple emitters being evaluated, two cathode geometries were evaluated to determine what performance differences, if any, could be observed. A more traditional edge-mounted geometry was tested along with a geometry where the cathode was mounted internal to the thruster along its central axis. Limited research on the effects of an internally mounted cathode has been published and more research into this configuration is needed. [10] To affect the performance and efficiency analysis a number of operating parameters were observed and recorded. Input power to the thruster's anode and magnets as well as to the cathode keeper was tracked to determine the overall input power. Multiple instruments were utilized to determine the properties of the plasma plume generated by the Hall thruster. All measurements were taken under assumed steady-state conditions; no frequency-domain effects were evaluated.

Investigative Questions

The primary question this research seeks to answer is what combination of emitter material and cathode geometry will yield the best performance and efficiency for the specified operating conditions. The power input to the thruster and the power output of the plume must be quantified to determine the efficiency of the thruster. To determine the power output in the plume the characteristics of the plasma need to be observed and quantified. The next logical question is what effect does the choice of emitter material or cathode geometry have on the plume itself. Comparative spatial measurements of the

plume are recorded for each of the possible configurations in order to evaluate the plume. Finally, a center-mounted cathode has never been tested with a BHT-1500 Hall thruster, so a feasibility study of using the specified hollow cathode design is required.

II. Literature Review

Hall Thruster Applications

Even though Hall thrusters have been around for quite a long time, their use operationally and even experimentally aboard spacecraft has been somewhat limited. The Russian heritage of Hall thruster development is being taken advantage of now in the West. The Russian SPT series of thrusters, of which the SPT-100 mentioned above is one variant, have demonstrated 7,000 hours of operational life on orbit. [11] The nomenclature for the Russian thrusters comes from their designation as *stationary plasma thrusters* in the Russian literature; to differentiate them from pulsed plasma thrusters. In an SPT or Hall thruster the plasma is quasi-static. Most of the Russian Hall thrusters flown have been used for North-South station keeping (NSSK) operations on geosynchronous satellites.

The performance ranges for Hall thrusters vary greatly. The thrust levels for Hall thrusters range from the mN range all the way up to >1 Newton. Corresponding I_{sp} values range from ~1,500 sec. up to ~3,000 sec. [12] [13] [14] Efficiency values for Hall thrusters are generally around 50% with this efficiency increasing as the thruster's size and I_{sp} are increased. [11] The efficiency of Hall thrusters is generally less than that of ion engines, but Hall thrusters tend to be significantly lighter than their ion counterparts, especially in the low power thruster regime. [14] Mission requirements and constraints would dictate whether the selection of an ion thruster or a Hall thruster would be most beneficial. Ion engines are comparatively better for missions with large ΔV requirements whereas Hall thrusters are generally more ideal for time constrained missions. [15]

Due to operational lifetime considerations, missions such as NSSK are ideal for Hall thrusters, as they are not needed to operate continuously for the life of the satellite. This is not, however, the only mission being considered for Hall thruster use. NASA began its Hall thruster program in the early 1990's by looking at Russian Hall thruster technology. [16] Much work was done to increase the power and I_{sp} of Hall thrusters as well as to determine the operational lifetime of various designs utilizing various materials. Electric propulsion as a whole was advanced tremendously through the successful flight test of the NSTAR ion engine aboard NASA's DS1 spacecraft. This mission proved the viability of electric propulsion for deep space missions. The NSTAR system aboard DS1 provided a ΔV of 4.5 km/s using only 80 kg of xenon while operating, for a large portion of the mission, at a 99% duty cycle. [17] The Dawn mission, currently underway, seeks to utilize EP in an even more aggressive manner. The Dawn spacecraft carries three NSTAR engines capable of a total ΔV of over 11 km/s. This is necessary as Dawn's mission duration is slated for 10 years and includes rendezvous with two asteroids, Ceres and Vesta. [18]

Hall thruster in-flight experience has not been limited to Earth orbiting satellites. The European Space Agency's SMART-1 (Small Mission for Advanced Research in Technology) operated from 2003 to 2005. During this time, it traversed from Earth orbit to lunar orbit by means of a Hall thruster. SMART-1 carried a PPS-1350-G Hall thruster built by SNECMA motors. [19] The PPS-1350-G is based on the Russian Fakel SPT-100 design and is comparable in performance. [5] During the mission, the Hall thruster aboard the SMART-1 spacecraft was operated for nearly 5,000 hours to include over 800 engine startups and shutdowns. The SMART-1 mission demonstrated the ability to

throttle a Hall thruster and, using onboard instrumentation, was able to characterize the plasma to a limited degree. Additionally, the PPS-1350-G allowed the mission to be extended by a year as it was used to maintain its final lunar orbit (station keeping). Finally, in a remarkable demonstration of reliability, the PPS-1350-G operated as specified every time it was commanded, achieving a 100% reliability rate. [19]

Quite a few studies have looked at using EP for solar system exploration. In one of these studies, Manzella, Oh, and Aadland looked specifically at the feasibility of using a Hall thruster for a notional asteroid sample return mission to the asteroid Nereus. [20] Their work included development and testing of a prototype Hall thruster with a 10:1 throttle range at NASA's Glenn Research Center. A deep space mission using Hall thrusters, especially where any sort of rendezvous is required, would require a degree of throttle-ability. Their work concluded that using a throttle-able Hall thruster, a 70 kg increase in spacecraft mass could be achieved relative to a mission utilizing an NSTAR ion thruster system. [20] In another study, Witzberger and Manzella directly compared the use of Hall thrusters versus NASA's Evolutionary Xenon Thruster (NEXT), an ion propulsion system. In their study, which used the Solar-Electric Propulsion Trajectory Optimization Program (SEPTOP), developed by Jet Propulsion Labs (JPL), they analyzed deep space missions to Jupiter, Saturn, and Neptune. Based on their analysis, a spacecraft utilizing Hall thrusters would be able to carry at least 200 kg more payload than a spacecraft utilizing the NEXT system. [21] Additional studies by Brophy and others have looked at numerous missions, to include a Mars sample return mission, a Europa orbiter, and a Pluto/Kuiper flyby to name a few, where EP, either ion engines or Hall thrusters, would be the enabling technology. [22] [23] [24]

Hall Thruster Theory of Operation

A Hall thruster is an electromagnetic EP device sharing some similarities with ion thrusters. The Hall thruster's ion production method is quite different than an ion thruster as it relies on a magnetic field to trap electrons used to ionize the propellant. In order to generate thrust both thrusters rely on electrostatic potential, but the Hall thruster must have a number of components in a very different configuration. The first component is the cathode, electrically heated to produce electrons. A portion of the propellant flow, generally around 10% for low power applications, is sent through the cathode to help sustain the production of electrons in the cathode. Cathode operation will be discussed in further detail below. Figure 3 gives a schematic representation of a Hall thruster showing both an externally-mounted cathode and a center-mounted cathode.

A Hall thruster's geometry generally consists of a shallow cylindrical channel with a propellant feed system and an anode at the upstream end with a series of electromagnets arrayed along both the outside and inside of the channel. These electromagnets produce a radial magnetic field. The anode at the upstream end of the channel is biased positive. The electrons emitted from the cathode are attracted to the anode. This current flow also creates an electric field from the downstream electrons produced by the cathode to the positively biased anode upstream. Once the electrons enter the channel, however, they are trapped by the radial magnetic field and held in the channel as they spiral around the magnetic field lines. The crossed electric and magnetic fields in the channel cause an azimuthal motion or drift of the electrons. This azimuthal motion of the electrons produces what is known as the *Hall current*, which is where the

Hall thruster gets its name. Hall thrusters are also referred to as *closed-drift* thrusters in some of the literature.

In order to remain in the channel the electrons need some sort of restoring force to counteract the centrifugal force they feel. This restoring force is generated through the “wall sheath electric fields and the force associated with the magnetic gradient in the radial direction of the channel.” [5] The radius at which the electrons circle the magnetic field lines is referred to as the electron Larmor radius and is given by;

$$r_L = \frac{v_{\perp}}{\omega_e} = \frac{1}{B} \sqrt{\frac{2mV_{\perp}}{e}} \quad (1)$$

where v_{\perp} is the velocity perpendicular to the magnetic field line, ω_e is the cyclotron frequency, and V_{\perp} is the perpendicular voltage. The corresponding azimuthal drift velocity is given by;

$$\mathbf{v} = \frac{\mathbf{E} \times \mathbf{B}}{B^2} \quad (2)$$

In order for the Hall thruster to operate, the electron Larmor radius must be smaller than the depth of the channel so they do not travel to the anode before they can be used to ionize the propellant. In a similar fashion the ion Larmor radius must be much larger than the “characteristic channel length”, which corresponds to the depth of the channel, “so that the ion can be accelerated out of the channel by the applied electric field.” [5]

When the Hall current is established in operation, the propellant is then ionized and accelerated to produce thrust. A non-reactive gas, noble gases being preferred, is injected into the upstream portion of the thruster near the anode. Xenon is the most common propellant as it is the heaviest of the stable noble gases and can therefore provide the most thrust. Additionally, xenon has a “low ionization energy per unit

propellant mass, due to both a moderate ionization energy and a high atomic weight.”

[25] As the gas molecules encounter the electrons travelling azimuthally they are efficiently ionized through collisions with the trapped electrons. Once ionized, the molecules come under the influence of the axial electric field created by the anode upstream and the electrons emitted by the cathode downstream. Being positively ionized, the propellant molecules quickly accelerate and form the plume of the thruster. The plume is neutralized by the electrons emitted by the cathode. The thrust generated by a Hall thruster is a combination of Newtonian and Maxwellian effects resulting in a net force on the spacecraft.

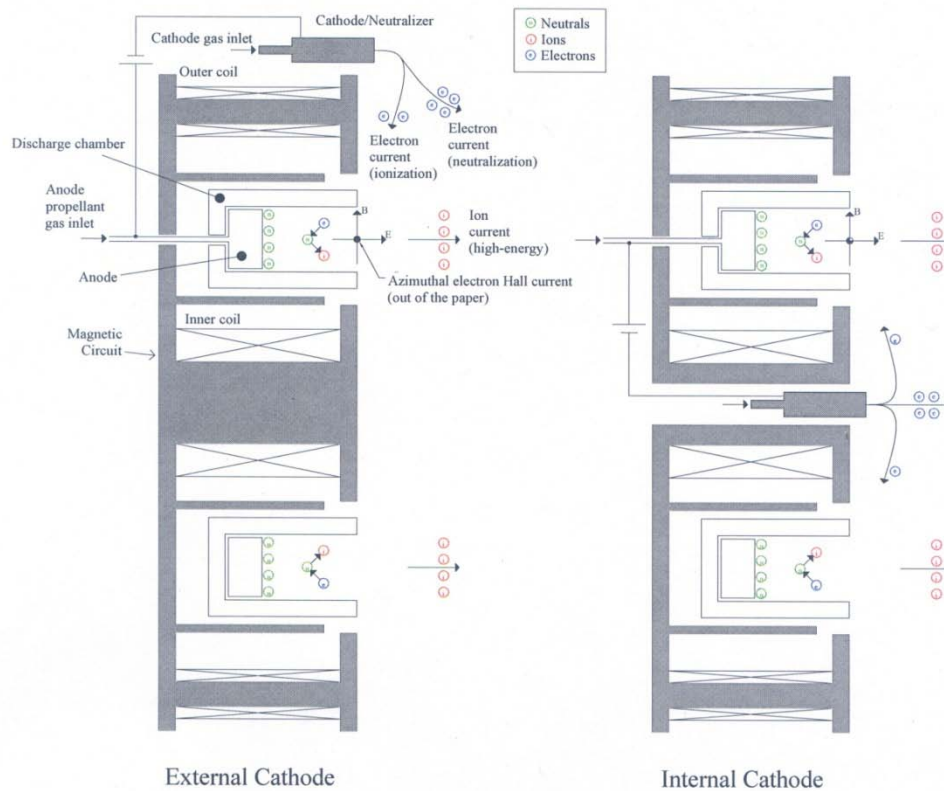


Figure 3. Schematic of a Hall thruster showing both internally and externally mounted cathode configurations. [10]

It often helps to think of the space within the channel as two separate, but overlapping, regions. The first, upstream region, can be referred to as the ionization region. The second, downstream, region is the acceleration region corresponding to the electric field, which peaks near the exit plane of the thruster. This overlapping of regions is one cause of beam divergence in Hall thrusters. [5]

There are two main classes of Hall thrusters. The more common type has a channel fabricated from a dielectric material such as boron nitride designed to withstand ion bombardment and limit the sputter erosion occurring because of it. The other type of Hall thruster is called a thruster with anode layer or TAL thruster. In this type of Hall thruster, the walls of the channel are made conductive and the anode is centered in the channel, which is typically only half as deep as the channel for thrusters with dielectric walls. [5] The metallic walls of a TAL thruster are also much more susceptible to secondary electron emission resulting in higher electron temperatures. Additionally, the acceleration region of a TAL thruster is about eight times smaller than a thruster with dielectric walls. [26] The Hall thruster used in this research is of the dielectric wall type.

Cathode Technology

The cathode is a fundamental component of a Hall thruster. Without it, the thruster cannot be started nor can its operation be sustained. In low power Hall thruster applications the design and performance of the cathode is of even more importance as its power and propellant requirements can significantly reduce the overall efficiency of the thruster. The fundamental purpose of a cathode is to produce electrons. In the Hall thruster, these electrons serve two purposes. First, they are required to produce the Hall current within the channel, the driving mechanism for propellant ionization. Second, the

electrons in the plume serve to neutralize the ions once they have been accelerated out of the thruster.

There are several types of cathodes. The simplest type of cathode is a wire, which has enough current flowing through it to allow the material to emit electrons. A tungsten filament would be one example of this type of cathode. The single crystal emitter is another type of cathode. This type of cathode is often used in electron microscopes as well as for lithography and electron beam welding, to name a few applications. It has also been considered for EP applications as well, but to a lesser extent. [27] The most common materials used for single crystal emitter-type cathodes include both Lanthanum-Hexaboride (LaB_6) and Cerium-Hexaboride (CeB_6), but tungsten can be used as well. [28] Figure 4 below depicts both a tungsten filament cathode and a single-crystal emitter.

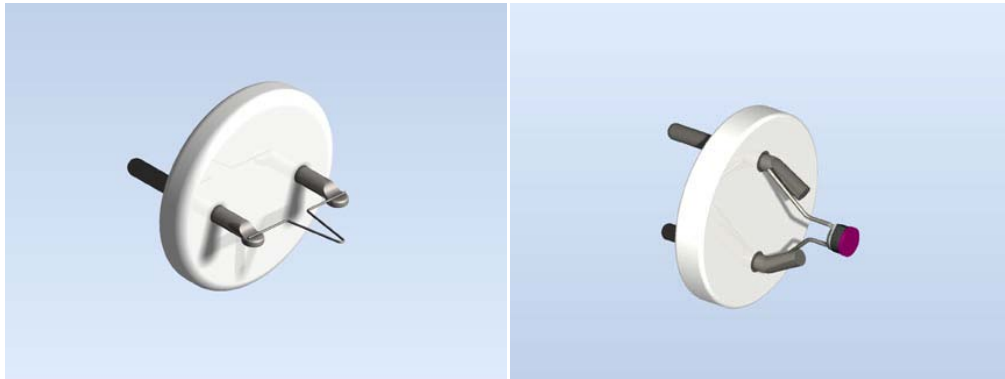


Figure 4. Tungsten filament cathode and LaB_6 single crystal emitter. [29]

Both filament and single crystal-type cathodes use Ohmic heating to induce electron emission. The current that a filament or crystal can emit by thermionic emission at a specified temperature is given by the Richardson-Dushman equation; [5]

$$j = AT^2 e^{\frac{-q\phi}{kT}} \quad (3)$$

Where A is the Richardson coefficient and ϕ is the work function of the emitter, material specific properties. In this relationship, increasing the temperature would suggest an easy method to increasing the required current. Obviously an upper limit would be the melting point of the material due to ohmic heating. Minimizing the energy required to produce a working current is paramount to keeping the overall device efficiency high. Therefore, a lower work function is desirable to increase the current density.

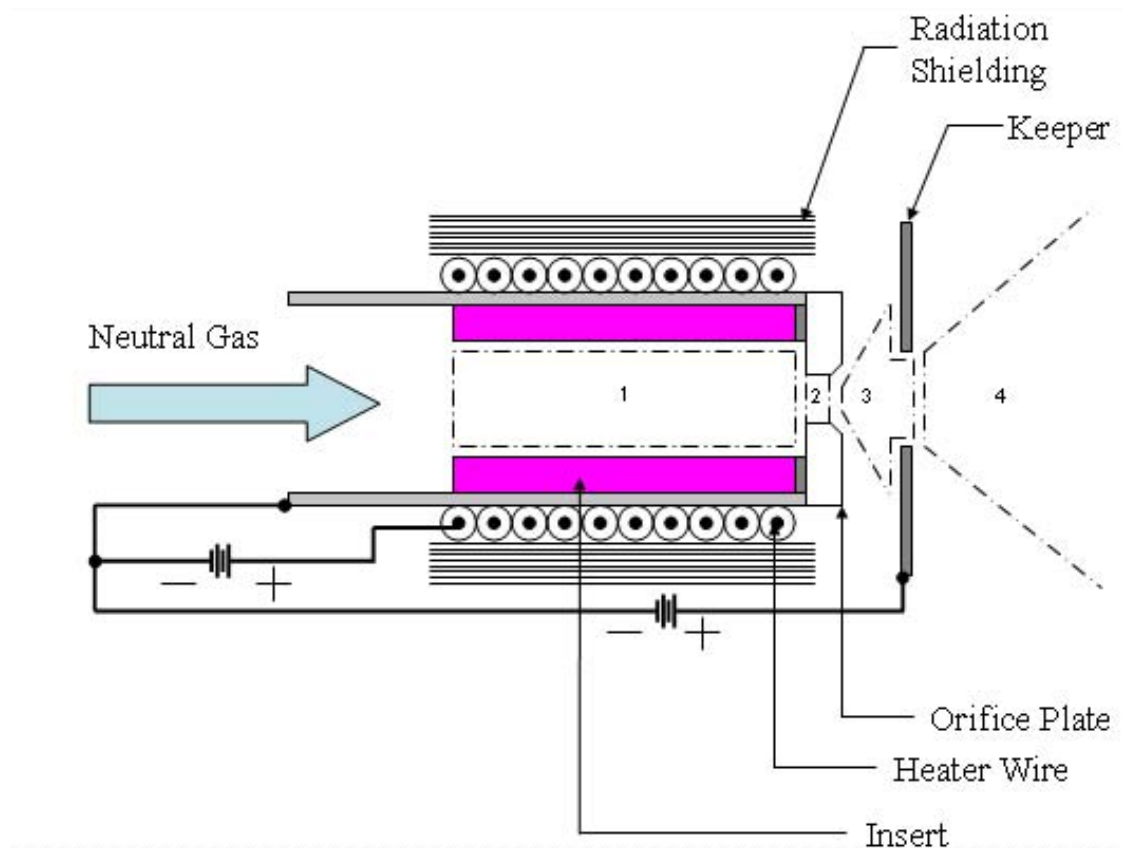
Since a cathode is usually immersed in a plasma, the “space-charge limit” must also be considered. Equation (4) below gives the maximum electron current density that can be accepted by a plasma due to space-charge effects; also known as the “cathode sheath.” [5] [27]

$$J_e = \frac{\kappa}{2} n_i e \sqrt{\frac{kT_e}{m}} \approx \frac{1}{4} n_e e \sqrt{\frac{kT_e}{m}} \quad (4)$$

It can be seen that the maximum emission current density depends on the ion density, n_i , as well as the electron temperature, T_e . κ is a constant whose value is usually about 0.5. [27] Knowing the characteristics of the plasma, equations (3) and (4) allow us to determine the best emitter for a given application.

The final type of cathode to be examined is the hollow cathode. The centerpiece of a hollow cathode is what is known as the insert. This is the material actually emitting the electrons during cathode operation. It is an open cylinder made of a material with a suitably low work function. Tungsten impregnated with other materials to lower its work function, along with LaB_6 and CeB_6 , have all be used as insert materials in various studies. [8] [27] [30] In contrast to the filament and single-crystal cathodes described above, hollow cathodes do not utilize Ohmic heating. An external heater filament heats

the insert through radiation and conduction. The insert is contained within a tube of a suitable high-temperature, non-reactive material around which the heater filament is wrapped. A neutral gas flows through the insert where plasma is created. Downstream of the insert is a positively biased electrode known as a keeper which serves to extract the electrons from the region inside the insert. Figure 5 shows the basic components of a hollow cathode as well as several additional design aspects described below.



1. Insert Region
2. Orifice Region
3. Cathode-to-Keeper Region
4. Coupling Region

Figure 5. Hollow Cathode Schematic [9]

There have been many different hollow cathode designs developed and tested. A common feature for hollow cathodes designed for EP applications is to use an orifice plate at the downstream end of the insert. The orifice plate is simply a disk of suitable material with a hole in the center, generally smaller than the inner diameter of the insert itself. The thickness of the orifice plate, along with the diameter and geometry of the hole, can affect the power consumption and minimum flow rates that a hollow cathode can handle. [31] In order to make the heater filament more efficient, it is often wrapped with a foil made from a refractory metal, such as tantalum, to reduce the radiative losses.

The keeper can also be fabricated in a variety of ways. Since the keeper simply acts as an anode to the plasma being generated inside the insert, it does not need to be overly complex. A simple piece of suitable material with a hole in it for the electrons and plasma to pass through, with a positive bias applied, is all that is needed. This simplest of designs is often referred to as an open-geometry cathode or keeper. [32] Both metals and graphite materials have been used for keepers. A somewhat more common design is to enclose the heater, insert, and other components within the electrically isolated keeper. In this design, the keeper is an open cylinder, completely open at the upstream end, where it would attach to the base of the cathode, and orificed at the downstream end, where the plasma and electrons are emitted.

Hollow Cathode Theory of Operation

In contrast to filament and single-crystal-type cathodes where Ohmic heating is the driving mechanism for electron emission, hollow cathodes take advantage of what is referred to as “field-enhanced emission” by virtue of the electric field present between

the plasma internal to the insert and the keeper. This phenomenon is also known as the Schottky effect and effectively lowers the work function of the insert material. [5]

$$\phi_{eff} = \phi - \sqrt{\frac{q|E|}{4\pi \cdot \epsilon_0}} \quad (5)$$

Equation (5) shows the relationship between the effective work function, ϕ_{eff} , and the electric field, E. ϵ_0 is the permittivity of free space.

Hollow cathode operation begins with the application of current to the heating element wrapped around the cathode tube containing the insert. Once the insert reaches sufficient temperature, it begins to emit electrons from its inner surface. These electrons impart a negative charge at the insert surface and form a double sheath there. [5] [9] Once the electrons are emitted, they interact with the neutral gas flowing through the cathode, ionizing it, and creating a very dense plasma inside the insert. The potential created by the keeper electrode causes the electrons to be accelerated away from the insert towards the thruster plume.

One of the advantages of hollow cathodes is their ability to operate in a self-heating mode. Once the cathode has been lit and is operating satisfactorily, the external heater element can be turned off and the cathode will continue to produce electrons and generate plasma. This obviously increases efficiency, as no energy is required to run the heating element continuously. The self-heating of the insert is due to three separate mechanisms. [5] The first is orifice heating. The high plasma pressures inside the insert induce a highly resistive plasma at the orifice. Through convection, much of the power in the orifice plasma is transferred to the orifice plate. The power absorbed by the orifice plate is then conducted or radiated to the insert. Since ions are produced inside the insert

and there exists a negative bias at the internal surface of the insert, ion bombardment of the insert's surface is the second form of self-heating. Finally, at high plasma pressures and high discharge currents, electron heating can occur whereby electrons with enough energy to pass through the wall sheath are created and then impact the internal surface of the insert, depositing their energy there.

Cathode Insert Materials

There have been many materials utilized for the fabrication of inserts. Pure tungsten has been utilized as an insert material, but it has many drawbacks. Its work function is 4.55 eV, considerably higher than many other insert materials. Therefore, pure tungsten must be heated to very high temperatures before emitting electrons. Much more common are impregnated tungsten inserts. Initially, compounds such as Barium Oxide were deposited on the surface of the tungsten to lower the work function, but the surface deposits were quickly depleted through ion bombardment. This gave rise to the impregnated inserts where the low work function surface layer could be continuously replenished by the material fabricated into the tungsten substrate. [5] A typical impregnate may consist of Barium Oxide (BaO), Calcium Oxide (CaO), and Aluminum Oxide (Al_2O_3) used in various ratios. [27] [33] By impregnating a tungsten insert with the materials mentioned, the surface work function can be lowered to ~ 2 eV subsequently requiring less heater power to induce thermionic emission. [5] [27] Most impregnated tungsten inserts are designed to operate around 1000 C.

The main drawback to tungsten-based inserts, both pure tungsten and impregnated inserts, is their susceptibility to poisoning. Water vapor and oxygen are the two most harmful contaminants to an impregnated insert, with oxygen being the most

harmful. Oxygen at partial pressures as low as $\sim 4 \times 10^{-7}$ torr can completely stop plasma generation inside the cathode. [34] Over time, a poisoned insert will need to be heated to higher and higher temperatures to begin emitting electrons, likely eventually exceeding the capability of the external heater element or the material properties of cathode components. To mitigate the effects of poisoning requires numerous conditioning and startup procedures. Special handling of tungsten-based inserts when exposed to atmosphere or maintaining them in an inert environment can reduce the possibility of poisoning to a degree, but there are efforts to reduce this requirement in order to make the integration and test of EP systems utilizing tungsten-based cathodes easier. [33] Additionally, extremely pure propellant is required as impurities in the propellant gas can react with the insert. Typically 99.9995% pure xenon is used, costing considerably more than standard xenon. Finally, extended conditioning procedures whereby the insert is slowly heated to its operating temperature over several hours reduces the possibility of poisoning. Conditioning procedures and the monitoring of the laboratory vacuum environment, using a residual gas analyzer, for example, allows for the possibility of poisoning to be minimized. Conditioning procedures may pose no major problems in a laboratory vacuum facility, where there are no time constraints, but if an EP device needs to be operational shortly after launch for on-orbit maneuvers in low-Earth orbit, a long conditioning procedure may not be ideal.

Much research has been done in the pursuit of more robust insert materials. Several boride-based compounds, primarily LaB_6 , have been extensively tested. [5] [8] [27] [30] Some recent work has also been done using CeB_6 as an insert material. [9] [27] [35] The work functions of single crystal LaB_6 and CeB_6 were experimentally determined

to be 2.70 and 2.62 eV respectively by Swanson and McNeely. [36] Similar results for LaB_6 were obtained by Jacobson and Storms. [37] Hollow cathode inserts cannot generally be fabricated from a single crystal, due mainly to machining requirements and overall size. Boride-based hollow cathode inserts are polycrystalline, being manufactured by press sintering powdered material into rods that are then machined into the required dimensions for the application. [8] [30] The work functions for boride-based inserts vary from insert to insert due to dimensional differences and density variations, but a typical value for a LaB_6 hollow cathode insert would be ~ 2.67 eV. [5] [8] [30] Despite the limited work done on CeB_6 as a hollow cathode insert material, several studies have shown the work function of CeB_6 to be slightly lower than that of LaB_6 for single crystal specimens. [27] [38] These same studies indicate CeB_6 has a lower evaporation rate than LaB_6 and is less susceptible to poisoning as well.

Both LaB_6 and CeB_6 operate at higher temperatures than impregnated tungsten inserts, but are still capable of operating in self-heating mode. [9] This would require more heater power to allow the insert to reach its emission temperature, but this drawback is mitigated by the boride-based inserts' reduced susceptibility to poisoning. The poisoning of LaB_6 has been studied and has shown it is capable of maintaining its emissive characteristics at partial pressures several orders of magnitude greater than that of impregnated inserts. [34] [39] Oxygen is still the primary catalyst for poisoning, but the boride-based inserts' ability to operate at the higher partial pressures relaxes the requirement for ultra-high purity propellant gases. Finally, the lower evaporation rate for CeB_6 , coupled with its lower work function, makes it even more attractive as an insert material for long-duration hollow cathode applications. [27] [38]

Center-Mounted Cathode Studies

Two studies have been completed that investigate the effects of mounting a cathode internally, along the central axis of the Hall thruster. Both of these studies, however, utilized high power Hall thrusters. Hoefer, et al. tested a Busek BHT-8000, 8 kW Hall thruster using two insert materials. [10] It was operated with an external hollow cathode using LaB_6 as the insert material and with an internally-mounted hollow cathode using impregnated tungsten as the insert material. McDonald and Gallimore tested a 6 kW Hall thruster (designated H6) with both external and internal cathodes that each used LaB_6 as the insert material. [40] Their study also involved varying the location of the cathode in the axial and radial direction as well as the rotation of the cathode axis from 0 to 90 degrees. The 0 degree setting corresponded to the cathode axis being parallel to the axial direction of the thruster and the 90 degree setting corresponded to the cathode axis being coincident with the radial axis of the thruster.

Both studies demonstrate a center-mounted cathode improves the performance of the Hall thruster. Hoefer, et al. showed a center-mounted cathode gives a more collimated and symmetric plume than an external cathode. [10] The more collimated plume improves performance in a variety of ways. There are fewer losses due to plume divergence and likely less erosion of the discharge chamber due to asymmetries in the plasma. This equates to extended thruster lifetimes and more accurate models for thruster lifetime. The more collimated plume also means fewer integration issues for a spacecraft. As mentioned in the introduction, the high-energy particles emanating from the thruster would negatively impact spacecraft components, so a more tightly collimated thruster plume would reduce these effects. Finally, the better symmetry means more accurate

numerical models can be developed based on the data collected from Hall thrusters operating with center-mounted cathodes.

McDonald and Gallimore used their results from the center-mounted cathode to compare the various geometries they studied for the external cathode. Despite the wide range of geometries for the external cathode they tested, the Hall thruster's performance with the center-mounted cathode was consistently at least 3% more efficient than with the external cathode. [40] Again, both of these studies utilized high power Hall thrusters. To the author's knowledge, no work has been done to integrate a center-mounted cathode into a low power Hall thruster. Additionally, neither of the studies mentioned above directly compares the performance of external or internal cathodes operated with different insert materials against one another and neither tested a CeB_6 -based cathode in any configuration. With the benefits of a center-mounted cathode readily apparent, it makes engineering sense to develop and test a center-mounted cathode that can be integrated into a low power Hall thruster to improve its performance.

Experimental Considerations

There are many variables that must be controlled or tracked when testing a Hall thruster. When looking at performance and more specifically, efficiency, the inputs to and outputs from, the thruster must be quantifiable in some form. A short list of factors to observe or control would include; propellant flow rates, thruster operating parameters, cathode geometry, cathode insert material properties, and the properties of the plasma that makes up the exhaust plume.

Propellant flow rates and thruster operating parameters are closely interrelated. Propellant will be required for both the cathode and for the thruster, with the thruster

requiring approximately 90% of the overall propellant flow. Precision mass flow controllers provide a means to accurately control and monitor the flow of propellant to both the cathode and the thruster. Manufacturers of Hall thrusters will characterize their thrusters' performance in a variety of ways and specify the conditions for optimal performance. Some of these conditions include propellant flow rates, anode discharge voltage, magnet current, and possibly keeper and cathode heater currents. Thrusters can be designed to operate at a single set point or to a specified thrust level and will be optimized to that end. In an effort to make Hall thrusters more robust, however, many thrusters can be operated at both their design, or rated, output capability or at a level less than the specified maximum. The input parameters described above can all be varied to achieve various levels of performance from a single Hall thruster.

The cathode used for a given Hall thruster need not be designed in concert with the thruster. It simply needs to provide the electrons for ionization of the propellant and neutralization of the exhaust plume. Cathode positioning with respect to the thruster has been examined in several studies. [40] [41] Low power Hall thrusters are generally designed to have the cathode or cathodes (if there is a redundant cathode as part of the design) mounted next to the thruster with the output of the cathode near the discharge channel of the Hall thruster. With increasing thruster size, the possibility exists for mounting the cathode internal to the thruster along its central axis. Whether mounted externally or internally, the cathode's position must remain fixed with respect to the thruster in order to make any determination of performance differences due to differing cathode inserts.

Just as geometry with respect to the cathode positioning is important for both performance and comparison, any effects resulting from the material property variations of the inserts needs to be captured as well. Since the work function of boride-based inserts varies from insert to insert due to the averaging of the work functions of the various crystal faces that make up each individual insert, knowledge of the density of the insert is critical. The physical dimensions also help determine comparative performance. The overall time an insert operates will also affect its performance. This is especially true for impregnated inserts where the impregnate is consumed, albeit extremely slowly, as the cathode is operated.

Performance Measurement and Plasma Diagnostics

Any time we wish to measure the efficiency, we must be able to measure the input and outputs and compare them. Quantifying the propellant used by the thruster and cathode, as well as the power being consumed by the anode, magnets, and keeper, is fairly straightforward. The above statement assumes the cathode heater is off during steady state thruster operation. Measuring the output of a Hall thruster can be done in a myriad of ways though. If thrust measurements are the goal, an inverted pendulum thrust stand can be used to directly measure the small thrust levels generated by Hall thrusters. By knowing the propellant flow rates and exhaust velocity, an I_{sp} value can be determined. Exhaust velocity can be obtained through laser velocimetry techniques such as absorption experiments or laser-induced fluorescence. Both of these techniques are quite useful, but neither gives much insight into the properties of the exhaust plume and plasma.

There are numerous ways to characterize the plasma forming the exhaust plume of a Hall thruster. The diagnostics used for this research include a Langmuir probe, a Faraday probe, and an ExB probe. Each of these instruments provides some of the information needed to determine overall thruster performance and efficiency.

One of the simplest instruments used for many years to study plasma is the Langmuir probe. Despite being an intrusive probe, whereby its presence in the plasma will impact the plasma properties, the Langmuir probe's ability to measure numerous plasma properties makes it an invaluable tool for plasma characterization (i.e. plasma potential, floating potential, and ion and electron density).

Other less intrusive probes enable us to measure parameters of specific interest in the study of EP as well. A Faraday probe measures current density, used to determine a number of parameters to describe the thruster exhaust plume.

An ExB probe, or Wein filter, can be used to separate ions based on their mass and charge state. Charge state determination allows us to determine how efficiently the propellant is being ionized. Any of the probes mentioned above can be positioned throughout the region of the thruster plume. By translating the probe through the thruster plume, spatial data can be obtained allowing for a more thorough understanding of the plume and the generation of accurate plume models.

Efficiency Determination

Numerous factors affect the efficiency of a Hall thruster. These efficiency factors can be looked at singly or as a whole, depending on the data available and the depth of analysis. Presented below is a brief overview of the various efficiency factors impacting

the overall performance of a Hall thruster. Kim provides the following equation to relate all of the various efficiencies into a single formula;

$$\eta_T = \frac{I_i}{I_d} \eta_i \eta_\beta \eta_v \eta_\epsilon \quad (6)$$

where all of the terms on the right-hand side of equation (6) are the various efficiencies of the thruster. [42] I_i and I_d are the ion current and discharge current, respectively. η_i is the propellant utilization efficiency, η_β is the focusing efficiency of the beam, which takes into account beam divergence, η_v is the loss caused by the distribution of ion velocities, and η_ϵ is the acceleration efficiency. Goebel and Katz, in their text, derive a similar expression that is more intuitive; [5]

$$\eta_T = \gamma^2 \eta_b \eta_v \eta_m \eta_o \quad (7)$$

η_b is the beam current efficiency which relates the fraction of the discharge current, I_d , that forms the beam current, I_b , as follows;

$$\eta_b = \frac{I_b}{I_d} \quad (8)$$

Similarly, η_v is the beam voltage efficiency term, relating the discharge potential, V_d , and the beam potential, V_b , as follows;

$$\eta_v = \frac{V_b}{V_d} \quad (9)$$

η_m is the mass utilization efficiency and relates the mass flow rates of propellant to the anode and cathode, \dot{m}_a and \dot{m}_c , respectively, to the mass flow rate of the ions leaving the thruster, \dot{m}_i ;

$$\eta_m = \frac{m_i}{m_a + m_c} \quad (10)$$

Finally, the electrical utilization efficiency, η_o , relates the discharge power of the thruster, P_d , to the input power, which includes the discharge power, the keeper power, P_k , and the magnet power, P_{mag} ;

$$\eta_o = \frac{P_d}{P_d + P_k + P_{mag}} \quad (11)$$

Equations (8) through (11) allow for the evaluation of the performance of a Hall thruster in a piece-wise fashion, providing the ability to look selectively at the various operating parameters of a Hall thruster and see what effect each has on the performance. The properties of the plume are captured in the γ^2 term. This term takes into account the effects of multiply-charged ions in the plume and the plume divergence and is given by;

$$\gamma = \alpha F_t \quad (12)$$

In this expression, $F_t = \cos \theta$, where θ is the average half-angle divergence of the beam. This assumes a uniform beam divergence “with a constant ion current density profile accelerated by a uniform electric field.” [5] For a cylindrical thruster the expression becomes;

$$F_t = \frac{\int_0^r 2\pi r J(r) \cos \theta(r) dr}{I_b} \quad (13)$$

$J(r)$ is the ion current density as a function of the radius, which can be determined experimentally using a Faraday probe. To relate the losses caused by doubly-charged ions, Goebel and Katz derive the following formula; [5]

$$\alpha = \frac{1 + 0.707 \frac{I^{++}}{I^+}}{1 + \frac{I^{++}}{I^+}} \quad (14)$$

Since equation (14) is a quotient of ratios, we do not need to know the specific beam current that is generated by the singly- and doubly-charged ions, only their ratio. This type of data is readily obtained experimentally through the use of an ExB probe. Additionally, this expression can be expanded to include the effects of more highly charged ions.

There are other ways to quantify Hall thruster efficiency beyond those presented here. Numerous studies focused on a single factor affecting the overall efficiency of a Hall thruster. [43] [44] There are many parameters, in design, construction, and operation of Hall thruster affecting the overall performance and efficiency of the thruster and their interrelatedness can make it challenging to draw conclusions as to the effects of adjusting a single parameter on the overall performance.

III. Methodology

Vacuum Facility

All of the experimental work described herein was conducted at the AFIT Space Propulsion Analysis and System Simulation (SPASS) laboratory. The centerpiece of the lab is the 2.5 meter long by 1.8 meter diameter vacuum chamber. The chamber has a volume of $\sim 6.5 \text{ m}^3$ and numerous feed-throughs with view ports for observing operations inside the chamber while pumped down. The chamber was built and installed by PHPK of Columbus, Ohio. The chamber utilizes a mechanical roughing pump to lower the pressure to approximately 100 millitorr. Once below its crossover pressure, four liquid-helium cooled cryogenic pumps are activated automatically to reduce the pressure further. When bringing the chamber up to atmospheric pressure between test runs, a low-flow nitrogen system was used to slowly back-fill the chamber with an inert gas to help mitigate any potential poisoning of cathode inserts and increase the life of the cryo-heads.

The cryogenic pumps are 0.5 meter diameter CVI Torrmaster TM500 cryopumps which can handle up to 4,000 l/s of xenon gas per unit. The pumps consist of an air-cooled compressor assembly that is connected to the cryo-head by means of flex lines. [45] [46] The cryo-head assembly reaches temperatures of 16-22 K and acts as a cold trap for gasses inside the chamber. The gases condense on the cold surfaces inside the cryopump and are trapped there maintaining the vacuum. The cryopumps are a closed system and do not vent or expel the trapped gasses to atmosphere and, as such, their capability to contain gases introduced into the vacuum chamber, namely the xenon propellant, degrades over time. This can be observed during chamber operation by noting a rise in the operating temperatures of the cryo-heads. The effects of this degradation can

be mitigated some by limiting the time a thruster is operated during a pump down cycle and cleaning of the cryo-heads' fins inside the chamber when the chamber is at atmospheric pressure to remove substances deposited there due to thruster operation. Figure 6 shows one end of the vacuum chamber along with a cryo-head and compressor, the roughing pump, and the cryo-head temperature indicators.

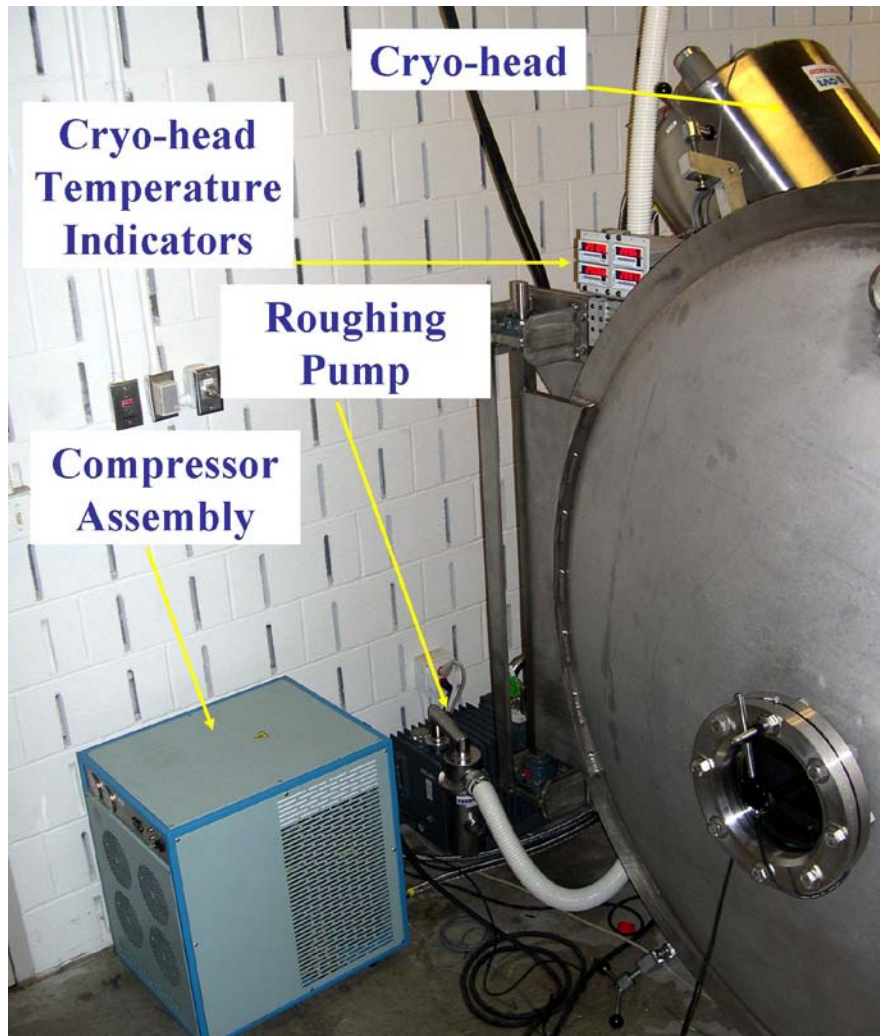


Figure 6. SPASS lab vacuum chamber and associated components.

To measure pressure and monitor the various gas species present in the chamber, a combination of devices were utilized. For pressures in excess of 0.1 millitorr, a Lesker

300 Series Convection vacuum gauge was utilized. This pressure sensor uses a convection-enhanced Pirani gauge to enable pressure measurements over a wide range. [47] It also contained the circuitry that activated the cryo-pumps and shut down the roughing pump once the crossover pressure was reached. It was primarily used to monitor the pressure during roughing pump operation.

The second device used to measure pressure was an Extorr XT Series Residual Gas Analyzer (RGA), model XT100. This device is a single integrated unit containing a Pirani gauge, a hot cathode ion gauge, and a quadrapole gauge and is capable of measuring pressures from atmospheric all the way down to 10^{-11} torr. [48] The RGA was controlled using Extorr's VacuumPlus software. The software provides a continuous pressure reading using either the Pirani gauge, if the pressure is above 0.1 millitorr, or the ion and quadrapole gauges for pressures below 10^{-2} and 10^{-3} torr, respectively. A plot of the partial pressures of gas species in the vacuum chamber is continuously updated as well, allowing the user to monitor for possible leaks or sources of poisoning. Figure 7 shows a screenshot of the VacuumPlus software and illustrates the partial pressures of the various species detected during a test run.

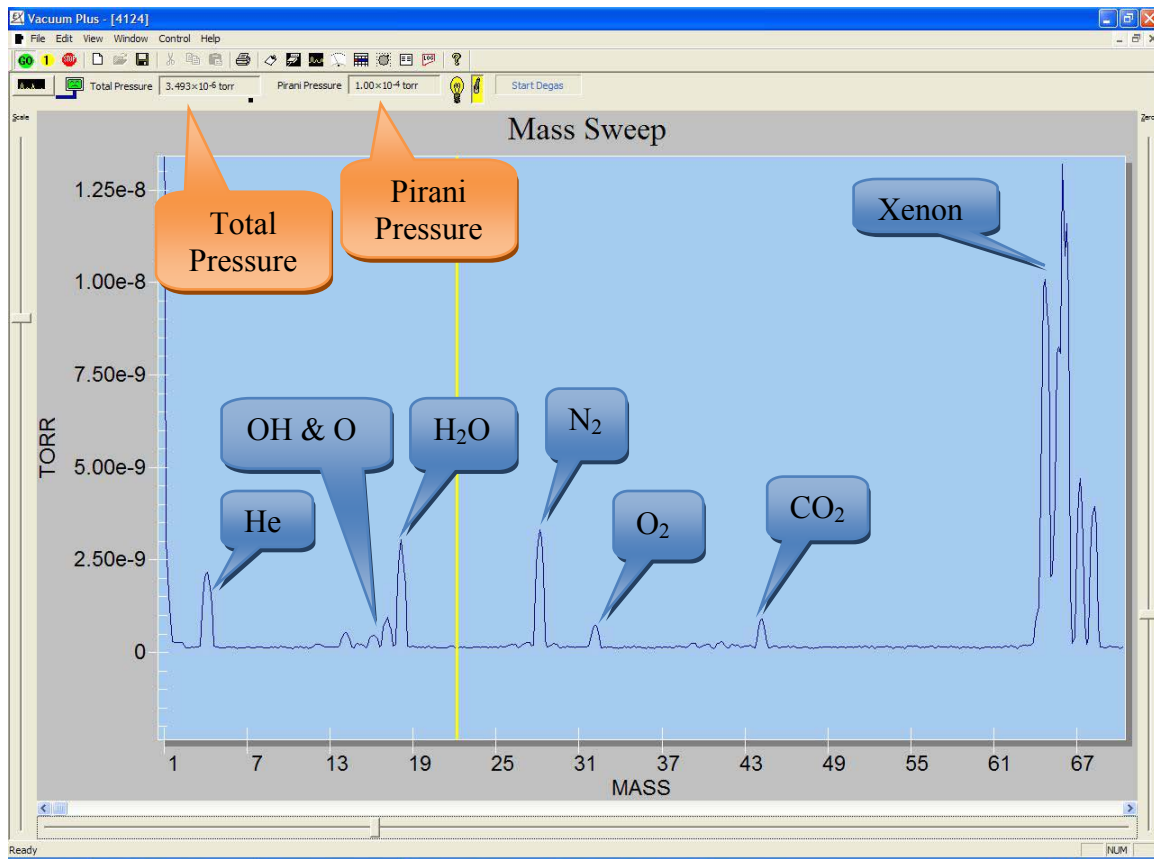


Figure 7. Screenshot of VacuumPlus software.

The final pressure gauge used is a combination of a Kurt J. Lesker KPDR900 vacuum controller and a calibrated Series 979ATV transducer. This device became available to the author after testing had begun and was used to cross check the operation of the Extorr RGA. The 979ATV uses a combination of a Pirani gauge with a hot cathode pressure sensor to enable measurement of pressures from 5×10^{-10} to 1000 torr. [49] With the propellant flow rates used for cathode and thruster operation, this gauge indicated that the total pressure inside the vacuum chamber did not exceed 1.3×10^{-5} torr during testing.

Test Assembly

To facilitate the use of multiple instruments to measure various properties of thruster operation, the thruster was mounted on an assembly constructed of 80/20® aluminum components bolted to the Z-axis of a three-axis Aerotech® translation stage system. The Aerotech® system allowed for thruster translation in all three axes over a 60 cm range. Each axis could be controlled independently to sub-millimeter accuracy. Additionally, scripts could be written to automate thruster movement. Depending on the instrument being used, the thruster was either pointed down the length of the vacuum chamber or at the ceiling of the chamber. Changing the orientation of the thruster had to be done manually as the Aerotech® system as installed has no rotational capability.

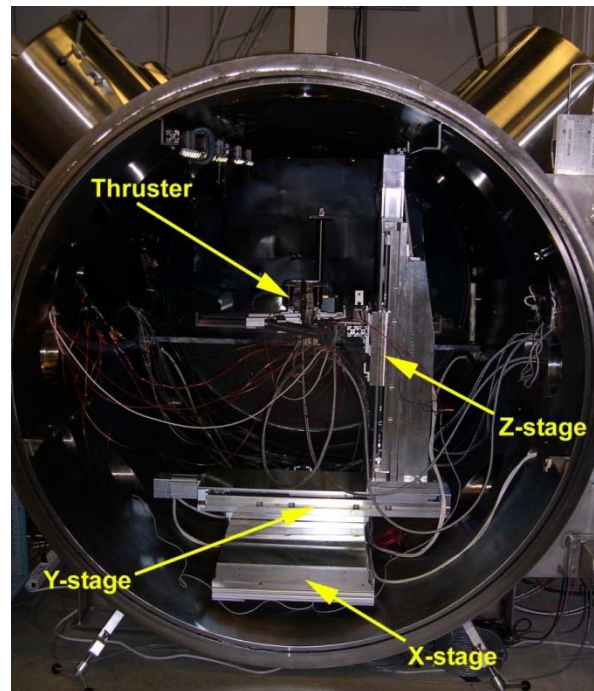


Figure 8. Photo showing thruster, pointing vertically, along with truss structure and Aerotech® translation stages.

The xenon propellant was stored in a gas bottle mounted on a wall external to the chamber. The pressure from within the bottle was initially reduced using a regulator/manifold assembly to pressures that the mass flow controllers could reasonably handle. Two MKS model 180A precision mass flow controllers, calibrated for xenon, were used to control the propellant flow rates. The flow controller for the cathode was calibrated from 0-10 sccm of xenon and the controller for the anode was calibrated from 0-50 sccm of xenon. Both controllers are accurate to $\leq 0.01\%$ of full scale. After passing through the mass flow controllers the xenon went through a gas feed-through into the chamber and through stainless steel flex lines to the cathode and thruster. The flow rates of the propellant were set and monitored by means of a MKS Type 247 four-channel readout.

Four DC power supplies were utilized to power the cathode and thruster during testing. For heater power a Hewlett-Packard 6033A power supply, rated at 250 W and capable of 0-20 V and 0-30 A, was utilized. Since a large potential at the cathode keeper aids in cathode ignition, a Matsusada REk650-2.5 power supply was used. This power supply is rated at 1625 W and capable of 0-650 V and 0-2.5 A with a current accuracy of 0.02%. Initially, both the magnet power and discharge, or anode power were controlled using a Busek BPU-600 Power Processing Unit (PPU). The discharge voltage accuracy was determined empirically to be 0.1%. The PPU received its power from a Sorensen DCS55-55 power supply rated at 3 kW and capable of 0-55 V and 0-55 A. The PPU card controlling power to the magnets failed part way through testing and so an Agilent 6038A power supply was substituted. This unit is rated at 250 W and capable of 0-60 V and 0-10

A with a current accuracy of 0.09%. The negative leads for the power supply going to each component were grounded either internal or external to the chamber.

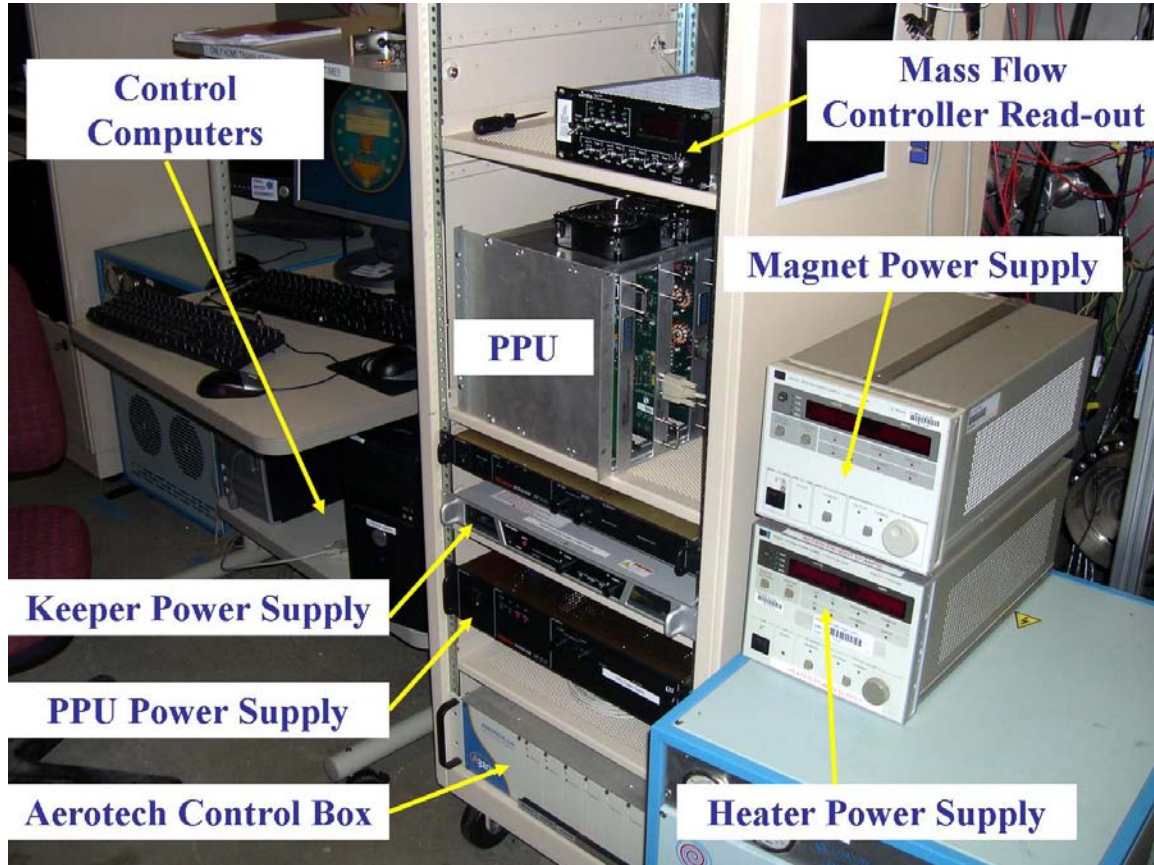


Figure 9. PPU and power supplies used to power thruster and cathode.

Hall Thruster

The key component in this work is a Busek model BHT-1500 Hall thruster. In the summer of 2007 Busek delivered a BHT-1500 Hall thruster modified to accept a center-mounted cathode to AFIT's SPASS lab. The designation for this modified thruster is BHT-1500-C. The detailed specification of the BHT-1500 are proprietary, so the data provided below is either publicly available from the manufacturer or was determined empirically by the author. Operating at a discharge power of 1.7 kW, with a discharge

voltage and current of 340 V and 5.0 A, respectively, the BHT-1500 delivers 102 mN of thrust at an I_{sp} of 1820 seconds. [12] The above performance was achieved using xenon as a propellant and equates to an overall efficiency of 54.6%. Depending on how it is operated, the BHT-1500 can be classified as either a low- or high-power Hall thruster. Much of the literature considers anything over 1 kW a high-power thruster. In this work, the BHT-1500-C was operated such that the total output was less than 1 kW putting it in the low-power category.

The frontal area of the thruster is square in shape, with each side being approximately 16 cm long. An electromagnet is positioned at each corner and together they make up the outer portion of the magnetic component of the thruster. The thruster's depth is approximately 9.5 cm. There is a single central electromagnet internal to the thruster and a removable metal center sleeve that forms the core of the inner electromagnet. Two center sleeves were utilized during testing. The original sleeve provided by Busek weighed 400 g and the second sleeve delivered weighed 365 g. The second sleeve was required to enable the integration of a center-mounted cathode of the design described below with the BHT-1500-C thruster. The diameter of the aft end of the original sleeve was not large enough to accept the cathode design to be tested. When operating with a center-mounted cathode a quartz sleeve supplied by Busek was used to electrically isolate the cathode keeper from the center sleeve.



Figure 10. The BHT-1500-C Hall thruster. [50]

As mentioned above, a Busek BPU-600 PPU was used to control the discharge power and, for a portion of the testing, the magnet power of the thruster. The PPU was controlled through a LabView® interface also supplied by Busek. The BPU-600 Host Simulator version 4 software enabled control and monitoring of the discharge and magnet power from a nearby computer. Figure 11 shows the controls available via the host simulator software. Both the software and the thruster itself are capable of independently controlling power to the inner and outer magnet coils separately, but the PPU did not have this capability. As such, the magnets, both inner and outer coils, were wired in series and powered as a single unit.

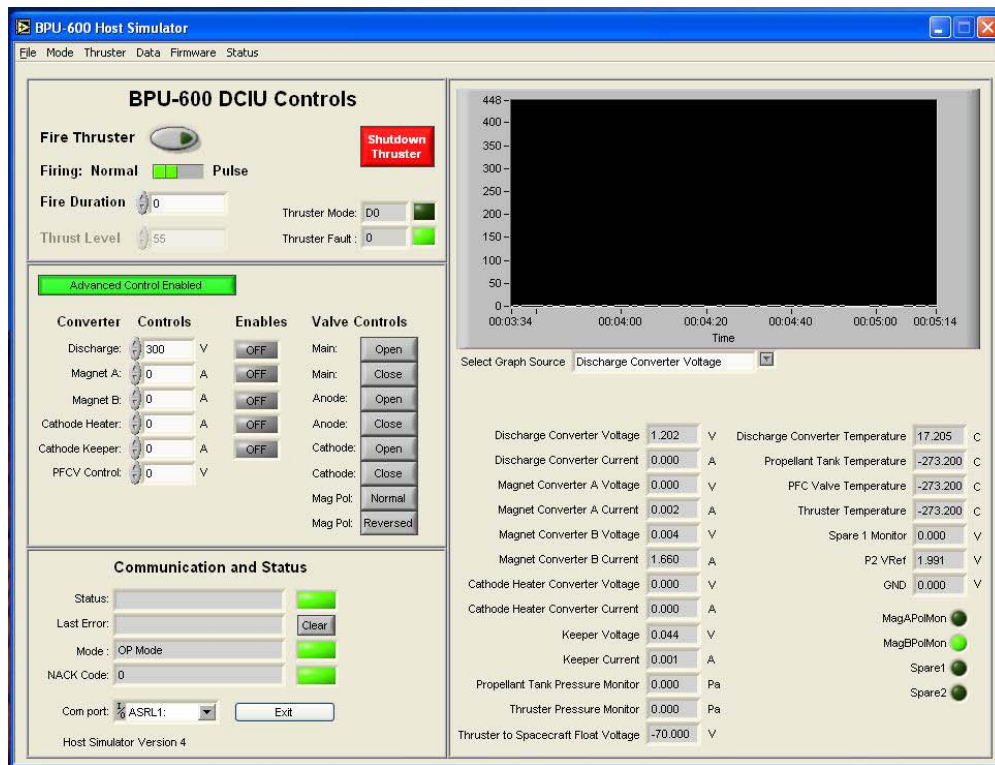


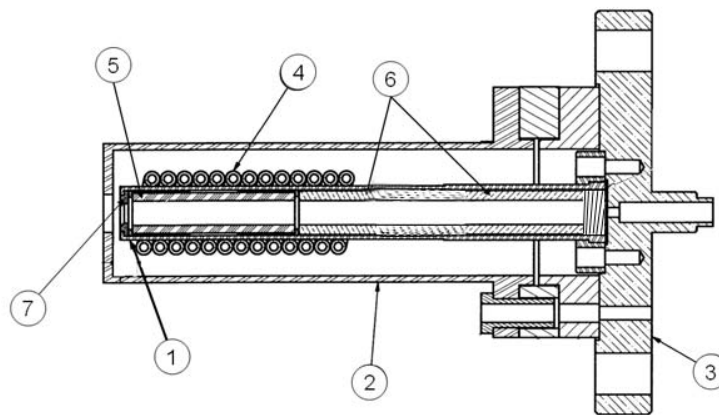
Figure 11. Screenshot of BPU-600 Host Simulator, version 4.

Like most Hall thrusters, the BHT-1500-C can be operated under conditions other than its rated values. In the case of this testing, the BHT-1500-C had to be operated at values less than the operating parameters mentioned above. This was due to two reasons. First, the cryo-pumps can only handle a certain amount of propellant flow before they are unable to maintain the chamber pressure at acceptable levels. Second, the BPU-600 PPU limits the available discharge voltage and current to 400 V and 3.2 A, respectively, giving a maximum discharge power of 1280 W.

Hollow Cathode Assembly

The hollow cathodes utilized in this research are based on Goebel's design from the work done at JPL. [30] Previous research done here at AFIT was the genesis for many

of the cathode design adjustments as well as cathode fabrication. [9] Enough components were on hand, fabricated, or obtained to enable the assembly of two cathodes at a time. To clarify the descriptions of the cathodes it must be noted that due to the geometry of the thruster and the cathode placement locations, two sizes of cathodes were fabricated. These will be referred to as the short and long cathodes. When conducting testing using an externally-mounted cathode, the short cathodes were used. When conducting testing using an internally-mounted cathode, the long cathodes were used. This was necessitated because the cathode's length needed to be longer than the depth of the thruster when mounted internally so the keeper orifice was flush with the thruster's face and the base of the cathode could be accessed from behind the thruster. Functionally the cathodes operated in identical fashion, as the inserts were the same size in each type of cathode. The only difference was the length. The figure below shows the individual components that make up the hollow cathode.



1. Cathode Tube
2. Graphite Keeper Electrode
3. Stainless Steel Base Plate
4. Tantalum Heater Wire
5. Insert (CeB₆/LaB₆/impregnated Tungsten inside protective carbon sleeve)
6. Carbon Support Tube
7. Tantalum Orifice Plate

Figure 12. Hollow Cathode Assembly

The most important component of the cathode is the insert. For this testing, three separate inserts were used, CeB_6 , LaB_6 , and one impregnated tungsten insert. The dimensions for each insert are identical and measure as follows; 6.4 mm outside diameter, 3.8 mm inside diameter, and 25.4 mm long. The figure below shows the three inserts that were used.

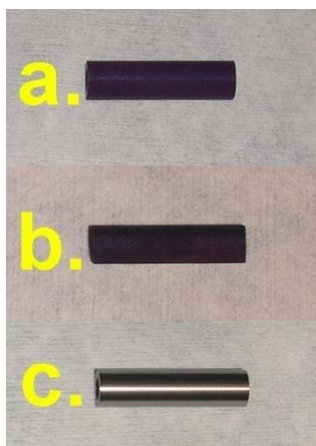


Figure 13. Cathode Inserts: a. LaB_6 , b. CeB_6 , c. impregnated Tungsten

Since the boride-based cathodes were manufactured as described above, their densities are of great importance. Vendor data specified the LaB_6 insert had a theoretical density of between 80-90% and the CeB_6 insert had a theoretical density of ~85%.

An important consideration in the design and construction for cathodes used in low-power applications is their thermal properties. In order to minimize the power consumed by the cathode, the goal is to insulate the insert to the maximum extent possible. The use of materials with high thermal conductivities, however, may be necessary for some components, such as the molybdenum cathode tube described below, to ensure structural integrity.

To insulate the insert from the cathode tube it was encased in a carbon sleeve made from DFP-1 graphite covering the entire length of the insert. A thin graphite washer, also made from DFP-1 graphite, was also placed at the forward end of the insert to separate it from the orifice plate. A support tube fabricated from Poco EDM-3 graphite was placed behind the insert to thermally insulate it. The rear-most component inside the cathode tube was a small spring made out of 0.254 mm diameter tungsten wire that kept all the components in the cathode tube snug against the orifice plate and allowed for thermal expansion of all the components during cathode operation. When a cathode had to be disassembled to switch out the insert, all of the components were cleaned and all the components within the cathode tube were kept with the insert that was tested or replaced as needed. This ensured there was no cross-contamination between the inserts.

The orifice plate was the forward-most component inside the cathode tube. It was fabricated from 0.25 mm tantalum sheet and had a 1.0 mm diameter orifice machined into it. All of the components described so far were contained in a molybdenum cathode tube. This tube provided the structural integrity for the cathode. The molybdenum cathode tube was bolted to a stainless steel base plate machined to accept the bolts for the cathode tube and keeper assembly and a fitting for the propellant.



Figure 14. Molybdenum cathode tube (long) and mounting flange.

To heat the insert to the levels where it would begin emitting electrons, a tantalum sheathed, alumina insulated heater wire was wrapped around the end cathode tube where the insert was located. The coils of wire around the cathode tube ensured an even distribution of heat to the insert region. The upstream end of the wire ran down the length of the cathode tube and through the flange that formed the base of the cathode tube. It then ran through the base plate to a location where a lead from the heater power supply could be attached. To further insulate the inserts, 0.127 mm thick tantalum foil was wrapped around the heater element twelve times. This foil was then held in place by wrapping it with a single layer of 0.254 mm thick tantalum sheet.



Figure 15. Assembled (long) cathode tube with heater wire installed.

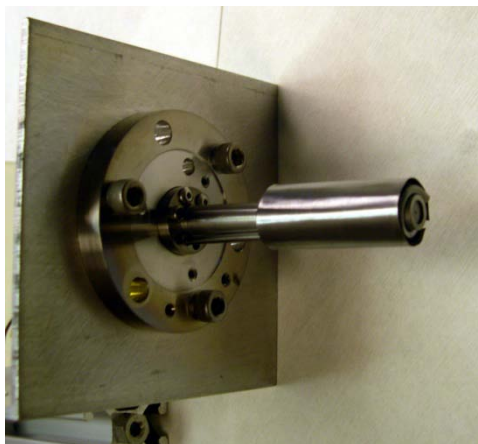


Figure 16. Cathode tube (short) with heater wire and tantalum foil, mounted to base plate

The keeper electrode was fabricated from Poco EDM-3 graphite and completely enclosed the tantalum-wrapped heater and cathode tube assembly. It was electrically isolated from the rest of the cathode by means of ceramic insulators and alumina hat washers. Graphite was chosen for several reasons. It can easily be machined into various shapes and it provided a degree of insulation from radiation losses. Additionally, graphite has a low sputter yield allowing it to last much longer than other materials used to fabricate keeper electrodes. The orifice on the keeper electrode was 6 mm in diameter.

Figure 17 shows both cathode keeper electrodes.



Figure 17. Cathode keepers; short and long.

As mentioned, the cathode tube and keeper sub-assembly were bolted to a base plate. This plate was threaded on one side to accept a gas feed line for the xenon propellant. The base plate was then mounted to a flange that allowed the cathode to be mounted in the vacuum chamber using the 80/20® components already in place. Figure 18 below shows the part used for building both the long and short cathodes and Figure 19 shows a fully assembled cathode.



Figure 18. Parts breakdown for cathodes—keeper and cathode tubes for both long and short cathodes shown. (Short cathode tube shown with heater wire and tantalum foil.)

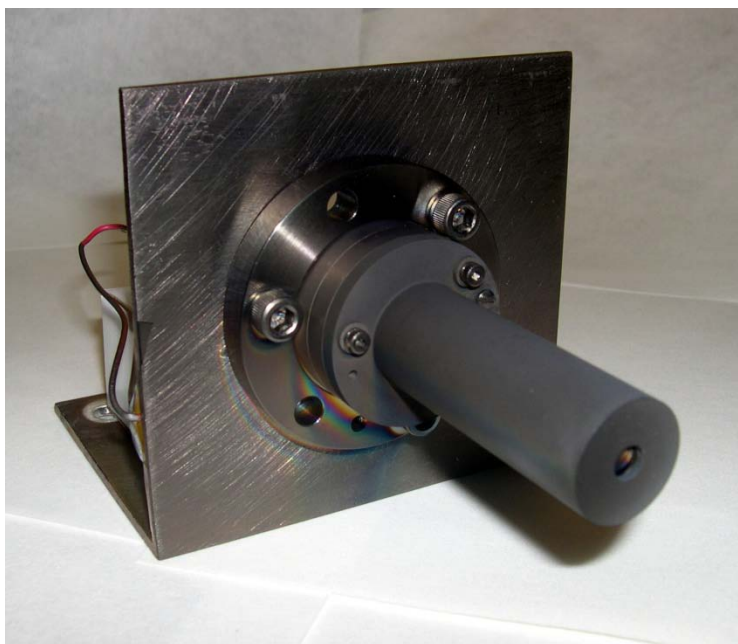


Figure 19. Assembled Cathode (short)

Data Acquisition and Measurement Equipment

In order to measure the efficiency, the power being input into the thruster and cathode must be observed and recorded. Current and voltage allow us to monitor the overall power used by the thruster and cathode. For each of the anode, magnets, and keeper, shunt resistors, connected in series, were used to measure the current. A Labview® program converted the voltage across the shunt resistor read by a National Instruments® SCXI-1321 4-channel readout to current by means of Ohm's Law. The voltage was sampled at a fairly low rate over a long time period to attenuate out any high frequency oscillations and minimize the effect of transients. The heater current was not tracked because once the thruster was operating steady-state, the power to the heater was turned off.

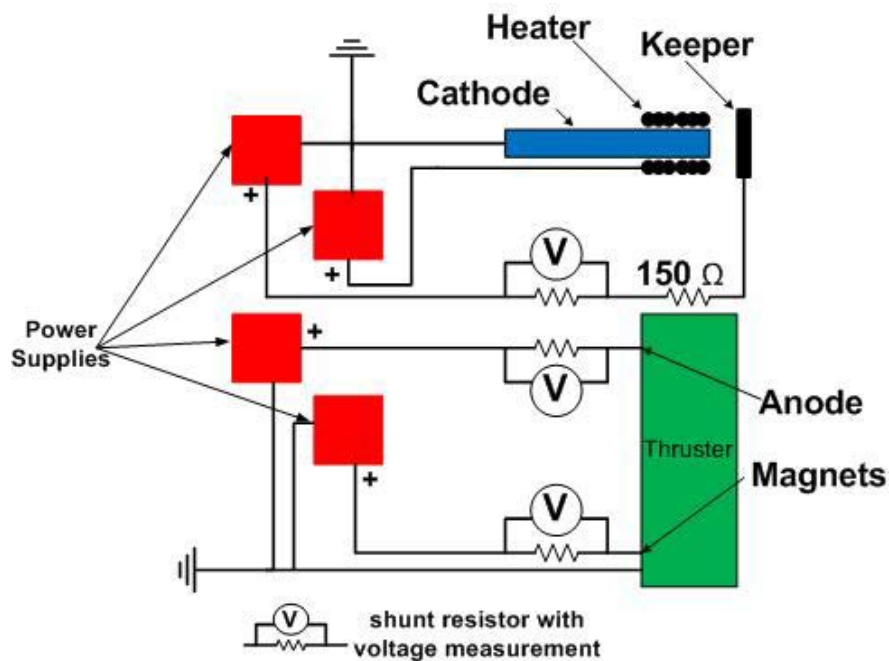


Figure 20. Electrical schematic of thruster and cathode.

Langmuir Probe

One of the oldest and most widely used tools for studying plasma properties is the Langmuir probe. Langmuir probes have been widely utilized for the study of Hall thruster plume properties. [40] [44] [51] [52] [53] [54] [55] In this work, a single Langmuir probe was utilized in concert with the Aerotech® translation stages described earlier to obtain spatial data for the BHT-1500-C Hall thruster. The probe used is a SmartProbe™ built by Scientific Systems. The system consisted of the probe itself, which was mounted to the vacuum chamber using appropriate hardware, the control electronics, which were housed in a single box, and the SmartSoft software, which ran on a nearby computer. Figure 21 shows the Langmuir probe installed through the ceiling of the vacuum chamber and the BHT-1500-C Hall thruster in relation to it. Additionally, low pressure compressed nitrogen was flowed through the probe shaft to keep it cool during thruster operation.

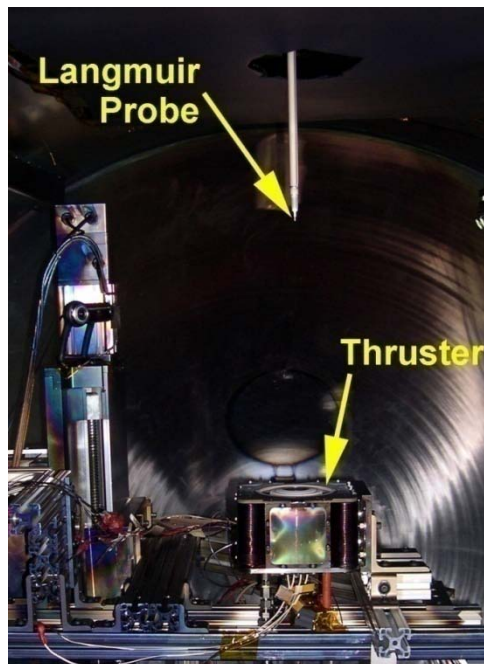


Figure 21. Installed Langmuir probe and Busek BHT-1500-C Hall thruster.

A Langmuir probe works by measuring the current flowing through its probe tip as the voltage applied is swept through a range of values. The probe resolution is 25 mV and 0.1 μ A for voltage and current, respectively. The probe tip used was a tungsten wire, 0.19 mm in diameter and 4.3 mm in length. The plasma created by the thruster is not isotropic, but the plasma exposed to the probe itself is assumed to be isotropic. The density gradients not accounted for by this approximation will induce a degree of uncertainty not quantified in the data presented here. [9] The voltage is swept from negative to positive to generate the corresponding current values. A number of sweeps are generally averaged together to generate a scan for a single location. The SmartSoft program was allowed to choose the lower and upper limits for the voltage sweep as a way to more efficiently collect the data and to prevent the probe from being damaged due to electron saturation at large positive potentials.

The I-V characteristic curve seen in Figure 22 is an output of the raw data generated by the Langmuir probe. There are three distinct regions within the curve from which numerous plasma properties can be extrapolated. The first region of the curve is called the ion saturation region. In this region, the probe is at a large negative potential relative to the plasma and subsequently saturates itself with ions while simultaneously repelling electrons. In this region ion current, ion number density, and ion flux can be calculated. At the end of this region, the plasma floating potential can be determined when the probe current equals zero.

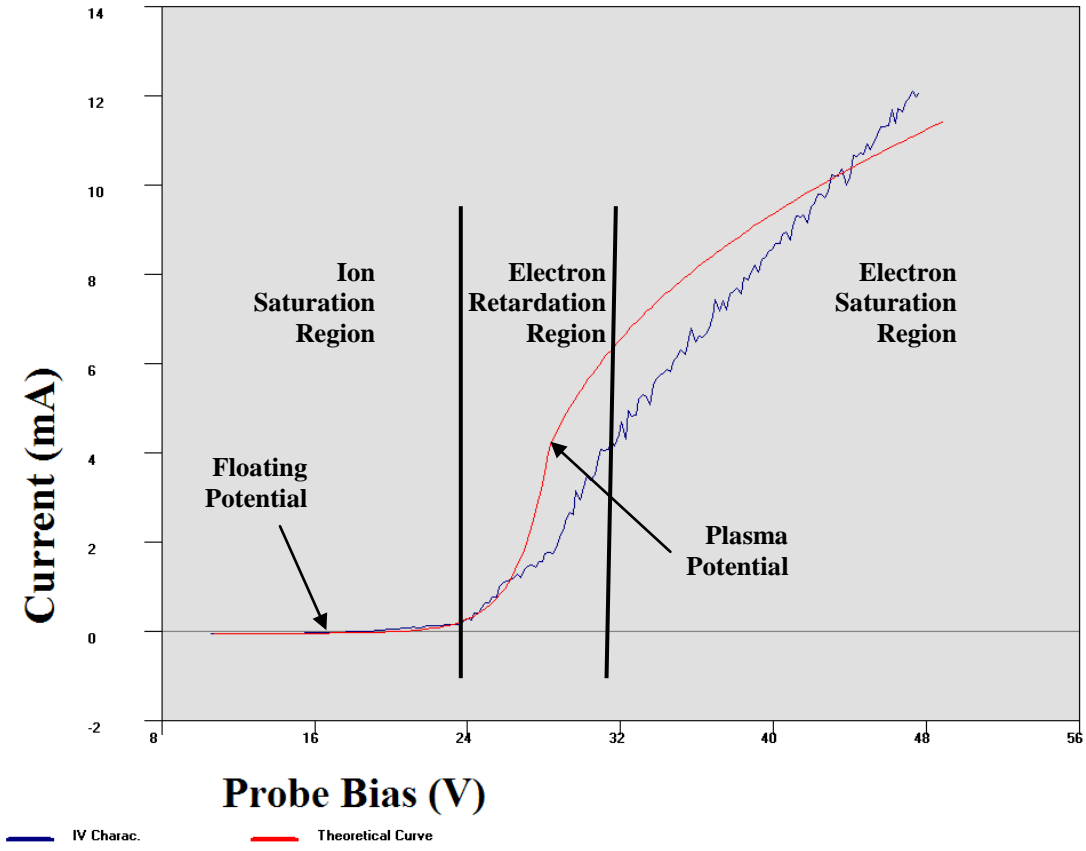


Figure 22. I-V Characteristic Curve

The second region of the curve is the electron retardation region. In this region, electrons with enough energy to overcome the probe's potential are collected. By assuming the electron distribution is in thermal equilibrium, the electron current is exponential with respect to the applied potential. In this region, the electron temperature can be determined as follows; [56]

$$\frac{I(V_p)}{\int_{V_f}^{V_p} I(V) dv} = \frac{1}{kT_e} \quad (15)$$

Where $I(V_p)$ is the measured current and the denominator is the integrated current from the floating potential to the plasma potential. The plasma potential is the location where

the second derivative of the I-V curve is zero. This corresponds to the voltage where there is no potential difference between the plasma and the probe.

The final region of the curve is the electron saturation region. Once the probe's potential exceeds that of the plasma, it quickly becomes saturated with electrons. Here a more accurate plasma potential is calculated by using the method of intersecting slopes, which incorporates the Laframboise theory. This theory takes into account the expansion of the probe sheath as a function of the applied voltage. The exponential curve for the electron retardation region and a line from the electron saturation region are extended to determine their intersection, which corresponds to the plasma potential. Using this more accurate plasma potential, electron temperature can again be calculated using equation (15) above, as well as electron number density as follows; [56]

$$n_e = \frac{I(V_p)}{A_p} \left(\frac{2\pi m_e}{e^2 k T_e} \right)^{1/2} \quad (16)$$

Where A_p is the probe area.

As mentioned above, the Laframboise theory takes into account the expansion of the sheath around the probe tip inserted into the plasma as the voltage is applied. The sheath width can be approximated by the following equation; [56]

$$d_s = \lambda_d \sqrt{\left| \frac{V - V_p}{k T_e} \right|} \quad (17)$$

In this equation, d_s is the sheath width, λ_d is the Debye length, V is the applied voltage, V_p is the plasma potential, and kT_e is the electron temperature. “Laframboise developed a theory which calculates the ion and electron current to the probe as a function of applied voltage for a range of different Debye lengths and probe radii.” [56] The SmartSoft

program uses the Laframboise theory in the form of several equations not presented here allowing for more accurate calculation of the plasma parameters, including ion number density. The number density is calculated as follows; [56]

$$n_+ = \frac{I_{0+}}{A_p} \left(\frac{2\pi m_+}{e^2 k T_e} \right)^{1/2} \quad (18)$$

The value for I_{0+} is determined using the parameters of the Laframboise theory derived equations that are integral the SmartSoft analysis algorithm.

For the research presented here, a matrix of spatial data was taken for each test case. The spatial data includes both axial and radial dimensions in a single plane. Scans were taken at axial distances from 50 cm to 15 cm from the face of the thruster in 5 cm intervals. 15 cm was the closest the thruster could be positioned to the Langmuir probe based on the installation of the probe and the thruster. For radial distances, the scans were taken at ± 20 cm from thruster centerline in 2 cm increments from 50 cm to 30 cm axial distance and at ± 16 cm from thruster centerline in 1 cm increments from 25-15 cm axial distance. Figure 23 shows the overall geometry of the data collection. For all the scans, the cathode was in the plane of the scan in order to see how the cathode affected the plume. For the center-mounted cathodes the radial data was only taken from the outermost point, 20 or 16 cm respectively, to the centerline of the thruster as the plume was assumed to be axis-symmetric when operating with a center-mounted cathode.

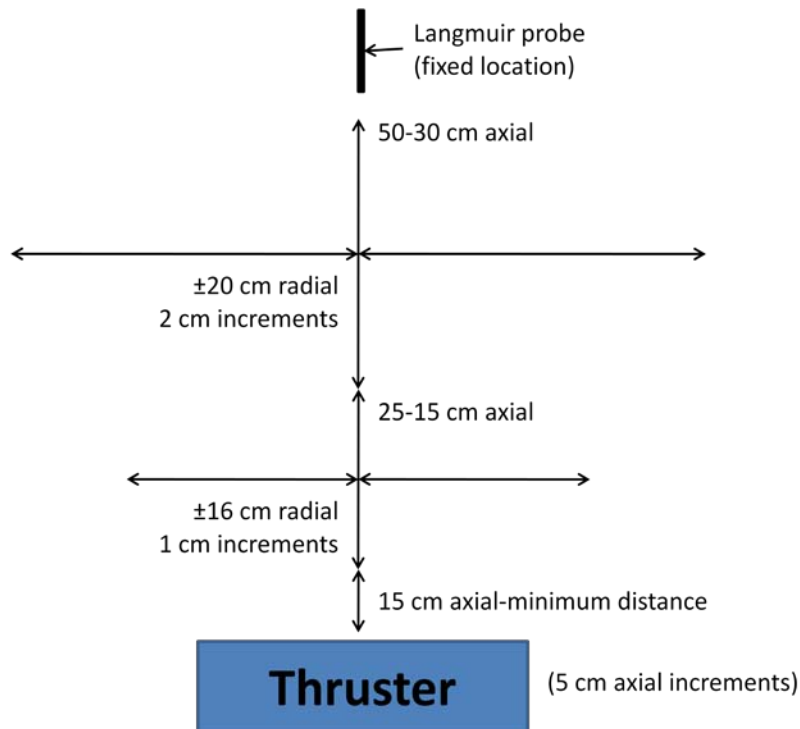


Figure 23. Spatial data collection points (edge-mounted cathode)

During a data collection at a given point, the SmartSoft program determined the minimum and maximum voltages and the voltage interval for each sweep. At each voltage, 10 samples were read and 50 sweeps were averaged to provide the values for a single location or scan. Once a scan was completed at a given location, the thruster was translated to the next location for the next scan.

Beam Profiler

In the summer of 2008, the author assisted in the installation of a beam profiling system designed and built by Colorado State University. The system consists of a three-axis translation and rotation system to which can be mounted a number of instruments. The translation stages consist of an axial or Z stage with 1.0 meter of travel and a radial or R stage also with 1.0 meter of travel normal to the Z stage. Due to installation

limitations, the entire travel of the radial stage, ± 50 cm ideally, could not be utilized. The rotational, or θ , stage was mounted on top of the translation stages and has a range of motion of ± 90 degrees. The motors for all the stages are water cooled and utilize a water cooler that is external to the vacuum chamber. The stages and instruments mounted to them are controlled via a LabView® program also developed at CSU. [57] The three instruments provided with the beam profiler include a Faraday probe, and ExB probe, and a Electrostatic Analyzer (ESA). For this research, the Faraday probe and ExB probe were utilized.

Faraday Probe

A Faraday probe is designed to measure current density in a plasma. The Faraday probe itself is a fairly simple device and it has been widely used to study Hall thruster plume properties. [10] [43] [58] It consists of a collector disk that has a potential applied to it and a device capable of reading the voltage across a resistor. The collector disk is mounted inside an enclosure generally biased negative to repel electrons, with an aperture to allow ions to enter and strike the collector disk. To determine the current density, j_B , the following formula is used; [59]

$$j_B = \frac{V \cdot 1000}{R \cdot A_{aperture}} \quad (\text{mA/cm}^2) \quad (19)$$

R is the value of the resistor in the circuit and $A_{aperture}$ is the area of the aperture in the probe body in cm^2 . Both of these values are fixed. V is the measured voltage across the resistor. The collector plate itself is usually biased positive to repel any low energy charge-exchange ions existing in the plume. Below are a photo and schematic of the Faraday probe used for this research.

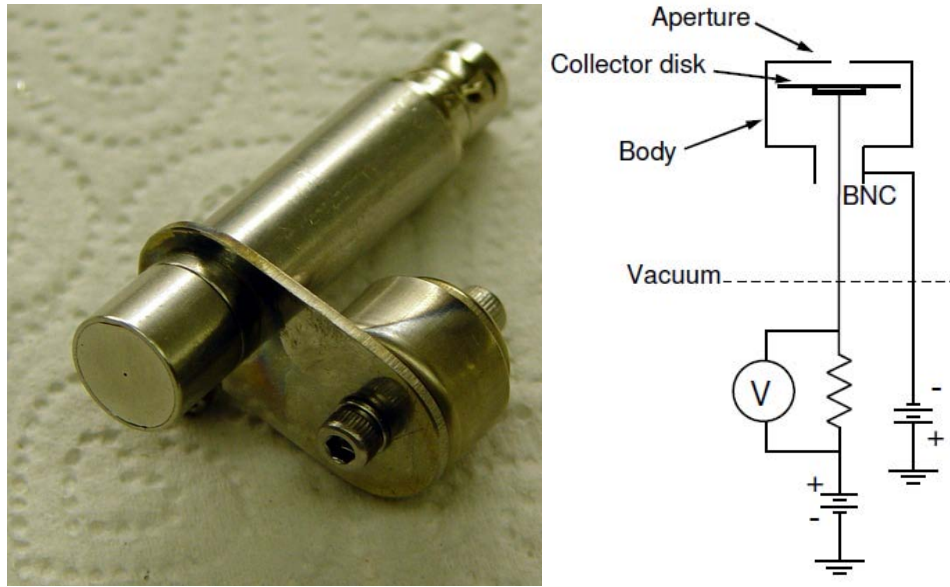


Figure 24. Faraday probe and schematic. [59]

For the testing conducted in this work, the following parameters were used. The aperture diameter is 0.381 mm. The collector plate was biased to +20 V using a Keithley 6517A electrometer/high-resistance meter. The probe body was biased to -40 V using an Agilent 6018A power supply. Voltage was read by an Agilent 34970A data acquisition switch unit accurate to $\pm 0.02\%$ and transmitted to the LabView® software recording the data to a file. Limitations on the data collection included the geometry of the beam profiler and the thruster as their minimum separation was 20 cm as well as the Agilent power supply, which would eventually overload once the probe was within a certain distance of the thruster.

Including the 20 cm axial offset, the probe began scanning at 70 cm axial distance from the thruster. It traversed radially from -40 to +40 cm (or vice-versa) from thruster centerline in 1.0 cm increments. The center of the thruster was specified as the center of rotation. The software and the theta stage kept the Faraday probe pointed at this point.

Once the data collect at a given axial distance was completed, the probe was moved 2.0 cm closer to the thruster and began traversing radially again. This continued until the Agilent power supply overloaded and data could no longer be collected. At each data point, the Agilent data acquisition equipment took 10 samples that were averaged to provide the single value for that point. The scans were completed the same way regardless of the cathode geometry being used.

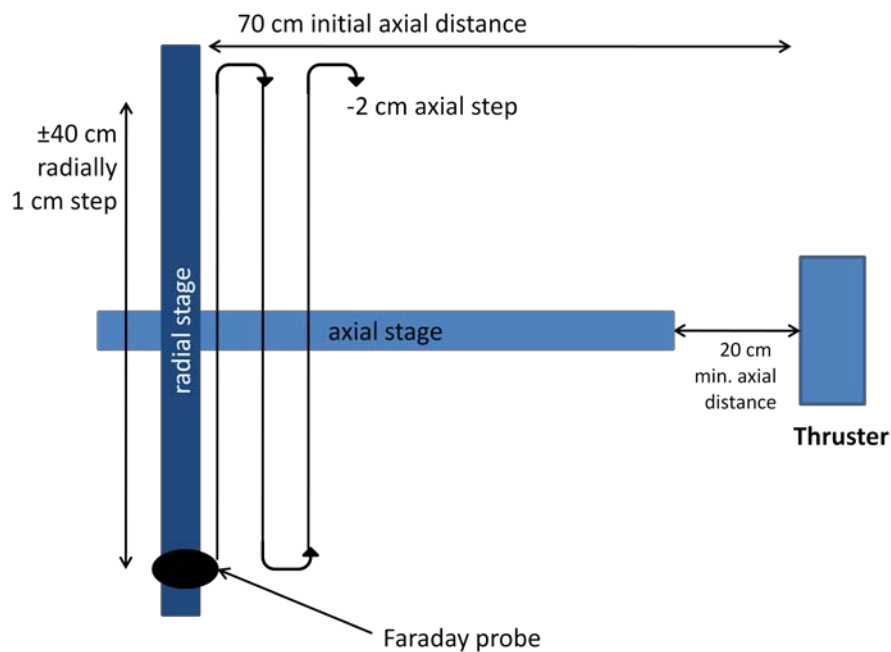


Figure 25. Faraday probe data acquisition setup.

ExB Probe

The ExB probe uses electric and magnetic fields placed normal to each other to enable the separation of ions based on their energy, mass, and charge state. ExB probes are commonly used in Hall thruster research due to their diagnostic usefulness. [10] [43] [58] Figure 26 shows the main component of the ExB probe. The entrance or collimator section has a 0.381 mm aperture, which yields acceptance angles for ions of ± 0.30

degrees. [60] This makes angular alignment of the ExB probe critical to successful data collection. After passing through the collimator, the ions pass through the normal magnetic and electric fields. They will only be able to pass through if the net force on the ion due to the magnetic and electric fields is near zero. The magnetic field is generated by permanent magnets and the electric field provided by an external source and swept through a range of voltages.

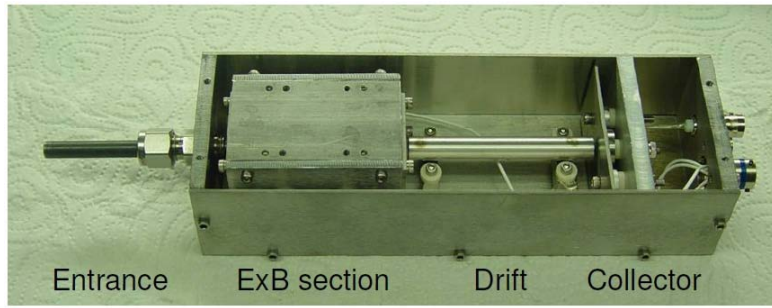


Figure 26. ExB probe with cover removed. [60]

After passing through the drift tube, the ions strike the collector where the current measured is a function of plate bias voltages. Just before the collector is a negatively biased suppressor which serves to repel electrons.

The equation derived from the Lorentz Force equation allowing us to determine the ion energy, mass, and charge state is; [60]

$$\Delta\phi = B \cdot d \cdot \sqrt{\frac{2 \cdot z \cdot q \cdot \Delta V_p}{m}} \quad (20)$$

where the $\Delta\phi$ term is the voltage difference between the plates. The following are constants on the right-hand side; B is the magnetic field strength, d is the distance between the plates, and q is the electronic charge. The z term is the integer value for the charge state of the ion and ΔV_p is the potential difference between the ion creation point

in the plasma and the collimator of the probe. By knowing the ion species of interest and the discharge voltage of the thruster, we can estimate the $\Delta\phi$ values where we should expect to see peaks in the current detected by the probe.

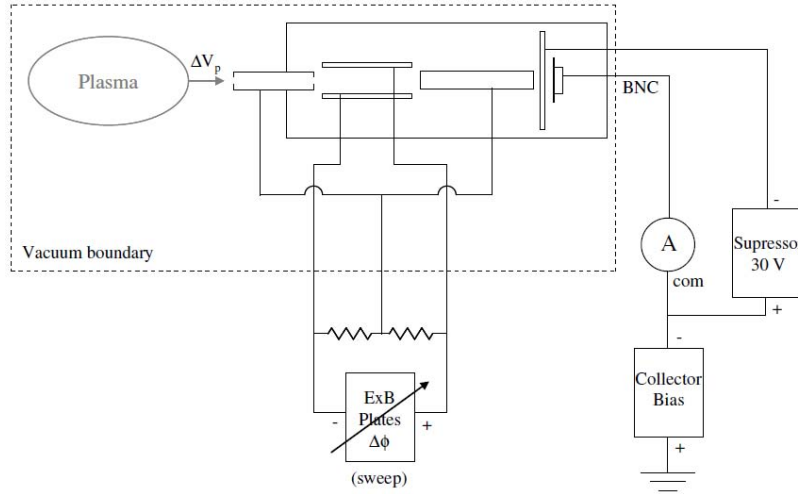


Figure 27. Schematic of ExB probe. [60]

Figure 27 shows the electrical layout of the ExB probe. For this work, the sweep voltage was applied by the Keithley 6517A electrometer/high-resistance meter. It then also measured the current at the detector. This meter was operated in the 200 pA range and is accurate to $\pm 1\%$ of the measured current for this range. A Keithley 6487 picoammeter/voltage source supplied the -30 V to the suppressor. The voltage across the plates was swept from +5 to +40 V in 0.1 V increments. At each voltage increment, 10 samples were taken and averaged to generate the data point.

For each test case ExB data was taken at a number of locations within the thruster plume. For the edge-mounted cathodes, at an axial distance of 50 cm, scans were conducted with the probe pointed down the centerline of the thruster and pointed directly at the channel on either side of the thruster. This was to see if any differences could be

noted due to the cathode's influence. Scans were also taken at 15 and 30 degrees either side of center line with the probe pointed at the near channel of the thruster. Further scans were taken at 60 and 70 cm axial distance that included all of the above except the off-centerline scans. For the center-mounted cathodes, the above scheme was used except with the assumption of an axis-symmetric plume, scans were only done on one side of centerline. Figure 28 illustrates the locations where ExB data were taken.

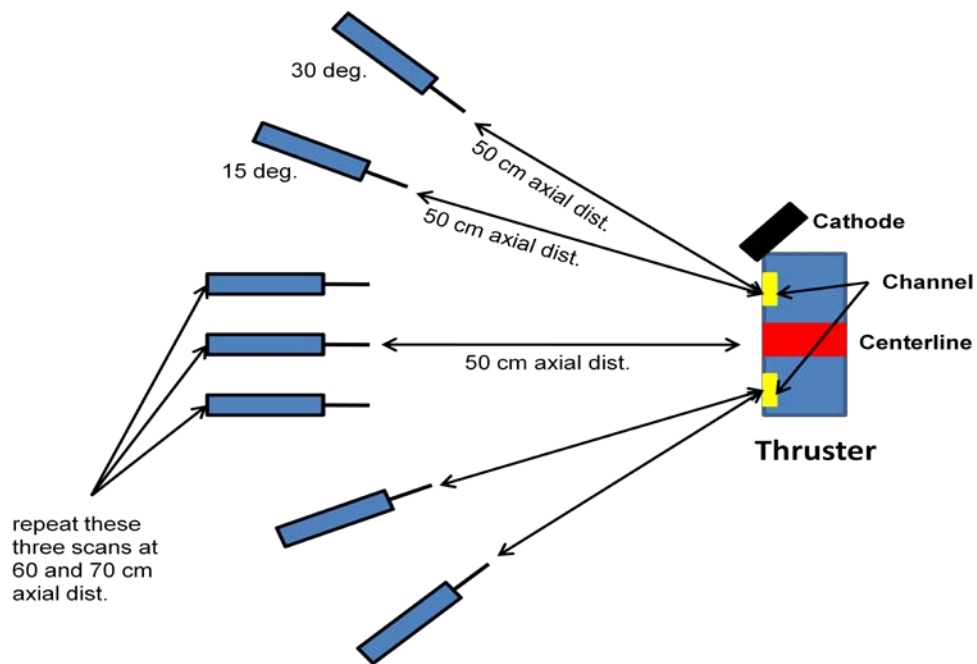


Figure 28. ExB data collection scheme.

Hall Thruster and Cathode Operation Test Points

Overall, three hollow cathode insert materials were tested in cathodes mounted in two different geometries. A CeB_6 , LaB_6 , and impregnated tungsten insert were each tested in an externally-mounted cathode. For the center-mounted cathodes only the CeB_6 and LaB_6 inserts were tested. The edge-mounted cathodes were angled 45 degrees towards the centerline of the thruster. They were mounted such that the radial distance

from the center of the cathode orifice plate to the center of the discharge channel of the thruster was the same as the distance from the centerline of the thruster to the center of the discharge channel. The center-mounted cathodes were inserted from behind the thruster such that the orifice face of the keeper electrode was flush with the face of the thruster. Due to the geometric constraints, the edge-mount cathodes' keeper protruded approximately 1.5 cm past the face of the thruster.

Two of the edge-mounted cathodes could be installed at the same time to enable testing of more than one cathode insert material during a single pump down cycle. Figure 29 shows the face of the BHT-1500-C Hall thruster with cathodes installed on either side. Figure 30 shows a side-view of the BHT-1500-C thruster and a single edge-mounted cathode installed. In this figure, both the cathode and anode propellant fittings can be seen as well as all the electrical connections for the cathode.

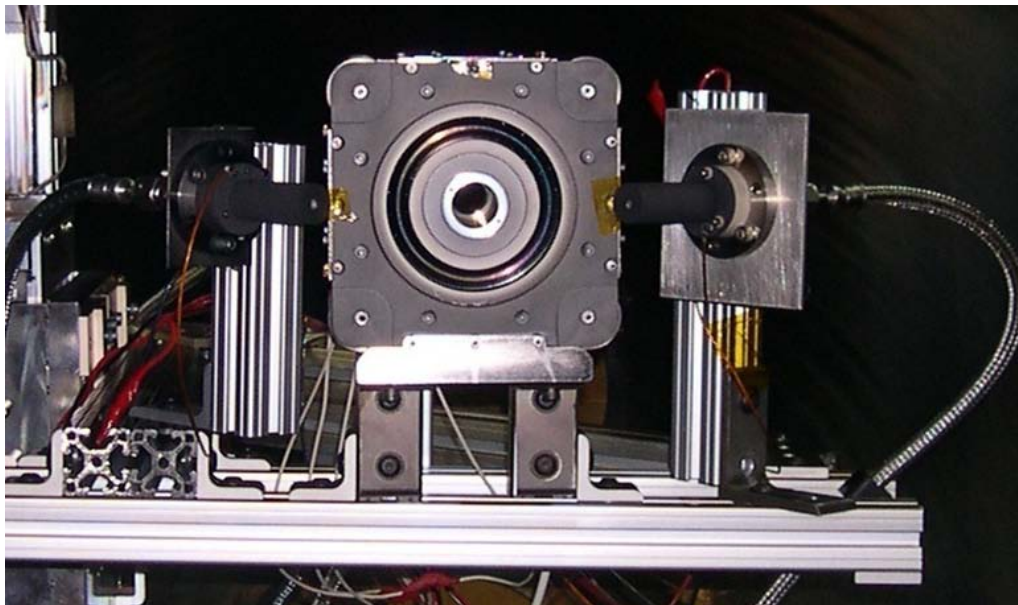


Figure 29. BHT-1500-C thruster with two edge-mounted cathodes installed.

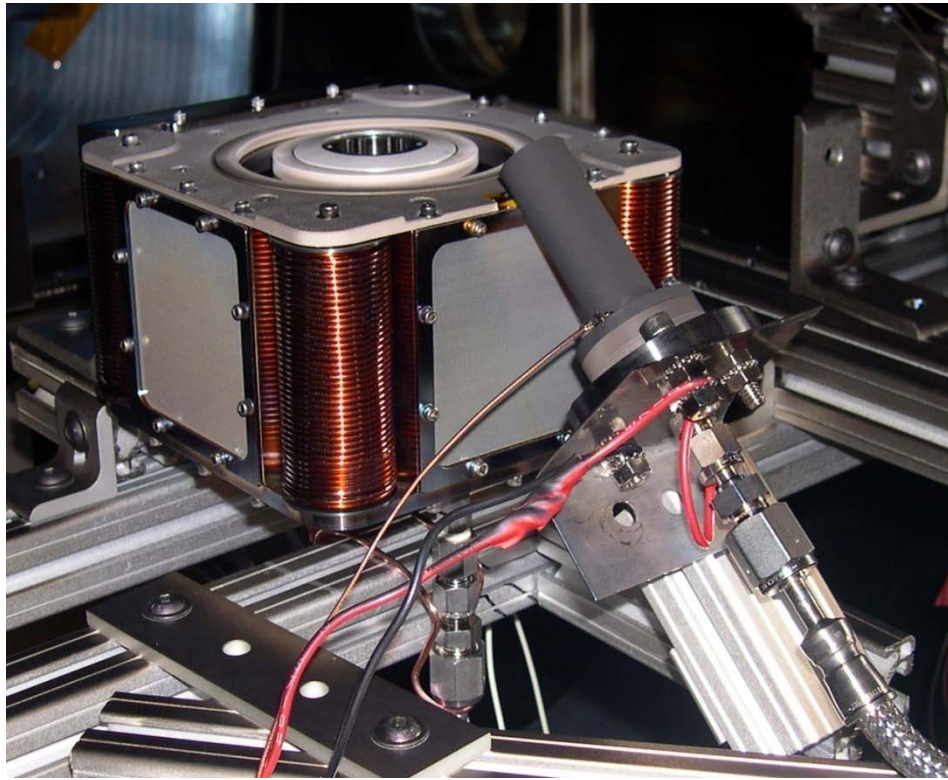


Figure 30. BHT-1500-C thruster with single edge-mounted cathode installed.

The center-mounted cathodes could only be installed one at a time for obvious reasons. The fragile nature of the graphite keepers and the tight space at the back of the thruster made the installation of the center-mounted cathodes challenging at times. Figure 31 shows a front and rear perspective of the BHT-1500-C thruster with a center-mounted cathode installed.

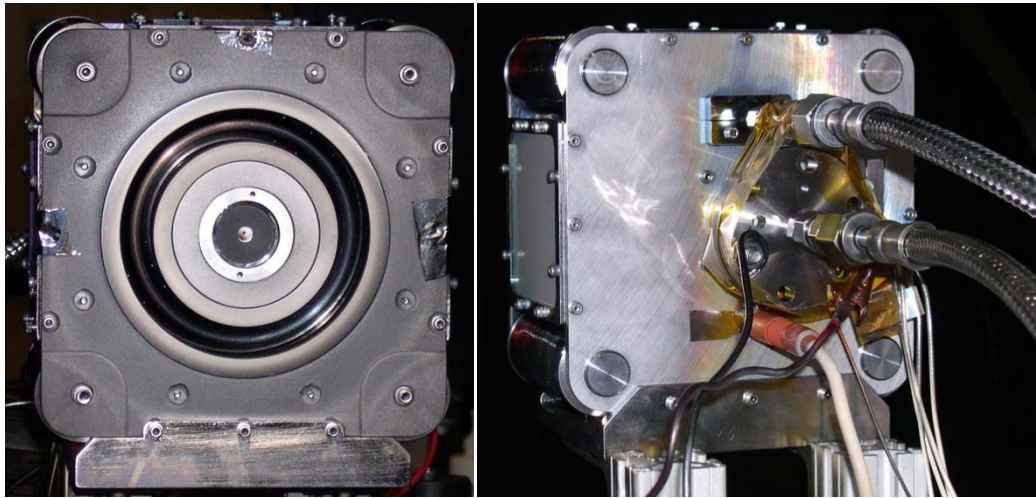


Figure 31. BHT-1500-C thruster with center-mounted cathode installed.

The thruster and cathodes were operated using values derived from the manufacturer and Warner's previous work with hollow cathodes. [9] [50] Since the thruster could not be operated at its rated value due to the limitations of the PPU and cryo-pumps mentioned earlier, a lower operating condition was used. Using Busek test data, a discharge voltage of 300 V was used along with a magnet current of 2.07 A and the propellant flow rate for the thruster was 25 sccm. [50] For the cathodes, the keeper current was set to 1 A and the propellant flow rate for the cathode was 3 sccm. Per Warner's previous research, this ensured the cathodes would remain in a focused, or spot mode during thruster operation. [9] The aforementioned spot mode is a stable operating condition where the cathode experiences smaller voltage fluctuations and operates at a lower discharge voltage. The discharge voltage for the cathode refers to the voltage from the insert plasma to the keeper. The counterpart to spot mode is plume mode, characterized by a diffuse plume from the cathode that exhibits larger voltage fluctuations while operating at higher discharge voltages. For most of the testing, the BHT-1500-C

thruster's discharge current was ~ 2.25 A. Along with the discharge voltage of 300 V, this equates to a thruster output of 675 W.

IV. Analysis and Results

Thruster-Cathode Integration

The actual assembly of the cathodes was fairly straightforward. The overall design is quite simple and the incorporation of the tungsten spring to allow for thermal expansion makes the cathode design more robust. The graphite pieces contained within the cathode tube would occasionally need to be replaced upon removal, but served well to insulate the inserts. Disassembling and cleaning the cathodes was a simple process as well.

Mounting the cathodes to the thruster posed a few challenges. Ensuring the edge-mounted cathodes were mounted in the same geometry for each test run took some care. The use of 80/20® allowed for relatively easy adjustment and a small jig was used to ensure the alignment was consistent for each test run. Integrating the center-mounted cathodes posed somewhat greater challenges. The brittle nature of the keeper material and the very tight tolerances between the center stem of the thruster, the quartz sleeve, and the keeper electrode, made installing the long cathodes a very delicate operation. Initial attempts were made to mount the center-mounted cathodes to the existing 80/20® components in the vacuum chamber. Two long keepers were broken in this process. The heavy stainless steel base plate for the cathode created a bending moment felt by the keeper itself at the rear face of the thruster with the thruster mounted to fire in a horizontal orientation.

The solution involved removing the mounting flange attached to the base plate of the cathode to reduce weight and the use of Kapton® tape to support the aft end of the cathode. The Kapton® tape can be readily seen in right-hand photo of Figure 31. The

tape also served to hold the cathode in a fixed axial position with the orifice face of the keeper flush with the face of the thruster. Additionally, an alligator clip was used to connect the positive lead for the heater power supply to the heater wire lead on the cathode. These measures resulted in the successful mounting of a center-mounted cathode in a low power thruster.

Thruster Operation

The BHT-1500-C fired successfully at the specified operating condition during all five test cases presented in this work. The successful integration and test of a center-mounted hollow cathode with a low-power Hall thruster achieves one of the primary goals set forth in this research, namely, to demonstrate the feasibility of such a design. The use of multiple cathode insert materials demonstrates the flexibility of the design as well.

The thruster and cathodes were started and operated with a very high degree of reliability. Initial operations with the cathode inserts at times required increasing the propellant flow to the cathode or power to the heater wire in order for the cathode to ignite. All of the cathodes had zero hours of use on them at the beginning of testing, so a bit of a “breaking-in” period was to be expected. The need for increased propellant flow or heater power when starting was prevalent primarily with the boride-based cathodes. The impregnated tungsten insert would ignite quite easily from the very beginning. Once operating, the cathodes were, overall, very stable, as was the thruster. The only exception being the LaB₆ cathodes. In both geometries these cathodes exhibited a degree of oscillation in the keeper voltage. The LaB₆ cathodes never ceased emitting, but the keeper voltage would, at times, fluctuate ± 10 -15 V. In one test run, the thruster, using an

edge-mounted cathode with CeB_6 as the insert material, ran for over 19 hours straight with no observed stoppages or fluctuations.



Figure 32. BHT-1500-C operating with externally-mounted cathode.

What follows are general startup procedures for the hollow cathodes and thruster. Appendix A contains detailed, step-by-step procedures for cathode conditioning, thruster startup, and system shutdown. Once the vacuum chamber pressure had stabilized, all valves in the propellant lines back to but not including the xenon gas bottle valve were opened to purge the propellant lines of any contaminants. Once this was completed heater power was applied using a constant current setting on the power supply. The current was increased over time until the power going into the heater was sufficient to allow for electron emission. This process of incrementally increasing the power to the heater is the

conditioning process and is critical to the mitigation of any poisoning effects due to contamination from exposure to atmosphere. Conditioning takes approximately one hour for the boride-based inserts and several hours for the impregnated tungsten inserts after the insert has been exposed to the atmosphere. If the insert had been previously conditioned and had remained under vacuum, the conditioning process could be significantly abbreviated. Once the conditioning process was complete, xenon was allowed to flow through the cathode. To ignite the cathode a large potential was applied to the keeper. Ignition was noted when the keeper power supply voltage dropped and current flow was observed.

Once the cathode was lit, xenon was allowed to flow to the thruster. Using the PPU host simulator software, a discharge voltage was then set on the anode. With no power to the magnets, a neutral ball of xenon plasma would then form at the face of the thruster. The power to the magnets was then applied via the host simulator or the external power supply. The magnets focused the plume into the collimated stream of xenon ions as seen in Figure 32. With the thruster operating, the heater power supply was secured and the cathode continued to operate in self-heating mode. Time was then allowed for thruster operation to stabilize before taking any data. To secure the thruster, all power and propellant to the thruster and cathode was secured.

Steady-State Power Consumption

Key to determining the performance or efficiency of a thruster is the knowledge of the power input into the device. The National Instruments® instrumentation and LabView® software gathered the data to determine the input current to the anode, magnets, and keeper. For each test case, the thruster and cathode were allowed to

stabilize before data collection began. Then approximately twenty minutes of data were taken to determine the input current and, while this was being done, no other testing was conducted.

Table 1. Component and total power consumption for each test case.

Component Power	Cathode Insert Material and Geometry				
	CeB ₆ (edge-mount)	LaB ₆ (edge-mount)	Impregnated W (edge-mount)	CeB ₆ (center-mount)	LaB ₆ (center-mount)
Keeper Power (W)	29.78	38.21	12.62	16.77	28.44
standard dev.	0.11	0.13	0.03	0.04	0.04
Magnet Power (W)	6.22	6.21	6.32	6.16	6.26
standard dev.	0.11	0.05	0.12	0.08	0.04
Discharge Power (W)	682.60	677.21	682.96	682.44	676.08
standard dev.	3.65	2.48	3.44	4.67	2.94
Total Power (W)	718.60	721.63	701.90	705.37	710.78
Electrical Eff. (η_o)	0.950	0.938	0.973	0.967	0.951

To calculate the power consumption values in Table 1, the following constants were used. For discharge power, the voltage was assumed to be constant at 300 V. For the magnet power, the resistance in the magnet circuit was assumed to be constant at 1.4 Ω . This neglects the change in the resistance of the magnets that occurs while the thruster is operating, but for the analysis here provides a basis for comparison. A steady-state keeper voltage value was recorded each time the thruster was run. The voltage values for each run corresponding to a particular test case were averaged to determine the keeper voltage for that test case. The keeper voltage values are the largest source of error in the power consumption calculations. The electrical efficiency was calculated using equation (11).

From Table 1, the impregnated tungsten-based edge-mounted cathode has the highest electrical efficiency. This is most likely due to its lower power consumption for the keeper, which is a result of the lower work function of the impregnated tungsten insert. The efficiency of the CeB₆-based cathode was slightly higher than for the LaB₆-

based cathode in both configurations. This can be attributed to the slightly lower work function of CeB₆. More interesting is that the electrical efficiency of both CeB₆ and LaB₆ increased when going from an edge-mounted configuration to a center-mounted configuration. Had an impregnated tungsten insert-based cathode been tested in the center-mounted configuration, it likely would have exceeded the electrical efficiency of all the test cases presented here.

Faraday Probe Analysis

Plasma current density was directly measured with the Faraday probe and a number of additional parameters were derived from this data. Looking at the current density distribution we can get an overall idea of the symmetry of the plume at the various axial distances data was taken. By integrating the current density, the overall beam current can be determined to allow calculation of the beam current efficiency, η_b , and other performance parameters. In order to fully map the current density in the plume, a Faraday probe is swept in a 180-degree arc at a constant radius in front of the Hall thruster. [61] [62] Due to the geometric constraints of the SPASS lab, this was not possible and the method of scanning in planes at various axial distances from the thruster described in Chapter 3 was used. As such, the maximum angle from the thruster centerline where data could be taken was ~38 degrees and decreased with increasing axial distances. Using this method, the author was unable to measure all of the current in the plume, however, valid comparisons between the test cases can be made. Figure 33 through Figure 35 below indicate the current densities observed at three axial locations, 50/60/70 cm, for each of the five test cases. (Note: the smallest axial distance for which data is available for the internally-mounted CeB₆ case is 52 cm.)

All of the figures representing current density are plotted as a continuous line to improve clarity since there are 81 data points for each axial scan. Additionally, the standard error of the current density was calculated and combined with the measurement accuracy of the equipment used to measure the voltage at the Faraday probe. The accuracy for all of the current density profiles is $\pm 0.049 \text{ mA/cm}^2$ which was the calculated standard error.

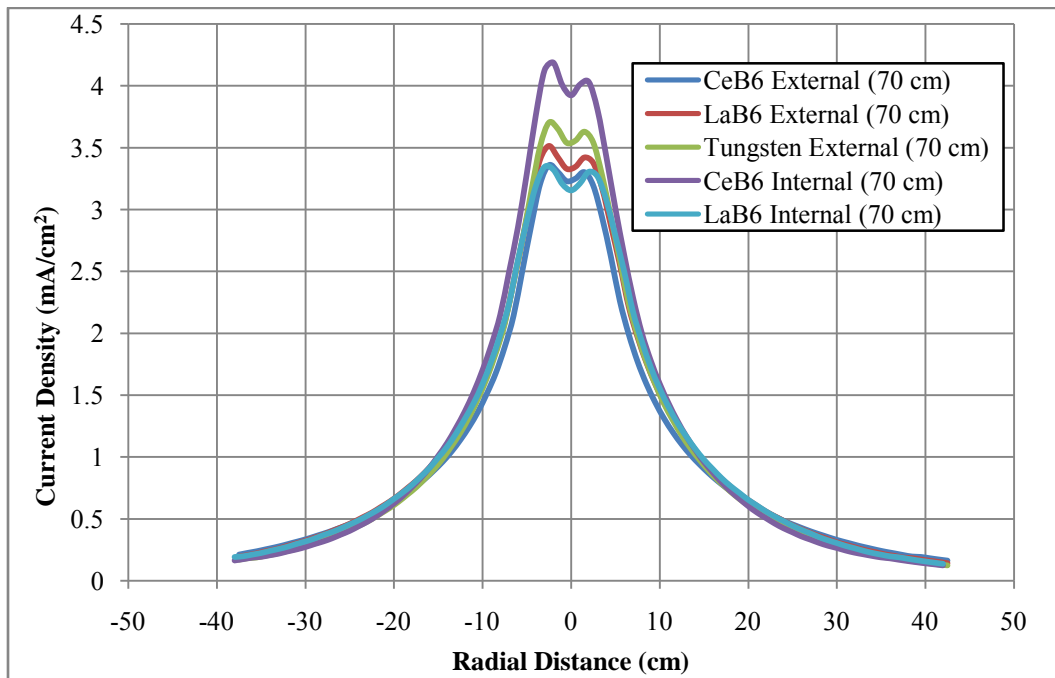


Figure 33. Current Density at 70 cm Axial Distance

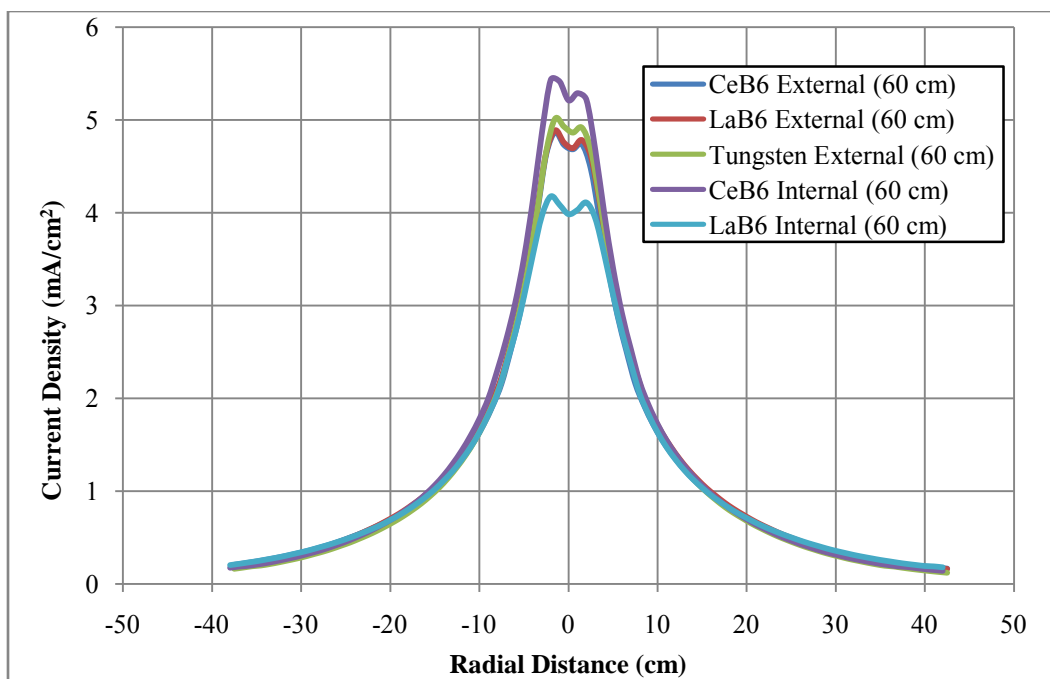


Figure 34. Current Density at 60 cm Axial Distance

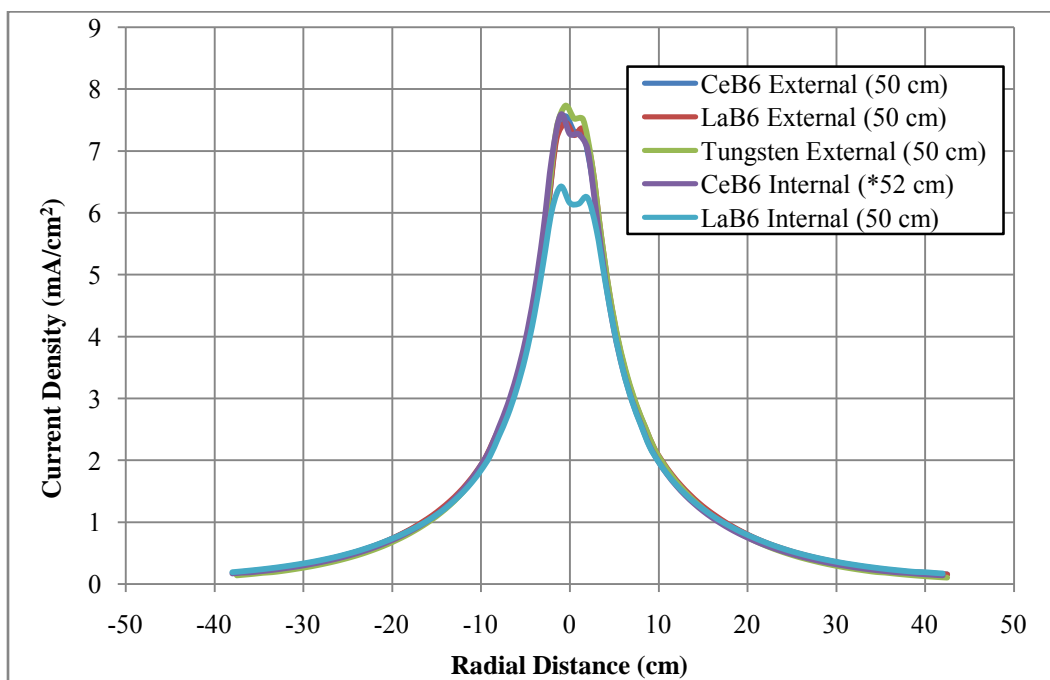


Figure 35. Current Density at 50 cm Axial Distance

Figure 33 through Figure 35 indicate increasing peak current density at smaller axial distances from the thruster, as would be expected. The thruster with the internally-mounted CeB_6 cathode demonstrates a higher peak current density than all the other cases as axial distance increases. The performance for all five cases, save for the internal LaB_6 cathode case, is very similar at 50 cm. The internally-mounted LaB_6 cathode demonstrated the lowest peak current densities at each axial distance. This is an interesting result that the author cannot attribute to any one particular phenomenon. The oscillation observed in the keeper voltage when operating with the LaB_6 inserts may be one source of performance loss. Despite its lower peak current density, the LaB_6 cathode shows the highest degree of symmetry in its current density distribution. Of note in the figures above, and those that follow, the centerline of the plume does not necessarily lie at exactly 0 cm radial distance. This offset is due to the combined slight alignment errors in the thruster, the beam profiler, and the probe itself. The asymmetry seen in the internally-mounted cathodes is likely due to slight misalignment of the theta stage on the beam profiling system.

Looking specifically at the externally-mounted cathodes, the LaB_6 cathode demonstrated a higher peak current density than the CeB_6 cathode at the furthest axial distance as evidenced by Figure 36. This is somewhat surprising given CeB_6 's lower work function. At all distances, the impregnated tungsten cathode out-performed the boride-based cathodes, which is to be expected based on the tungsten insert's work function. As the axial distance decreased the performance of the boride-based cathodes became nearly identical, which can be seen in Figure 37 and Figure 38.

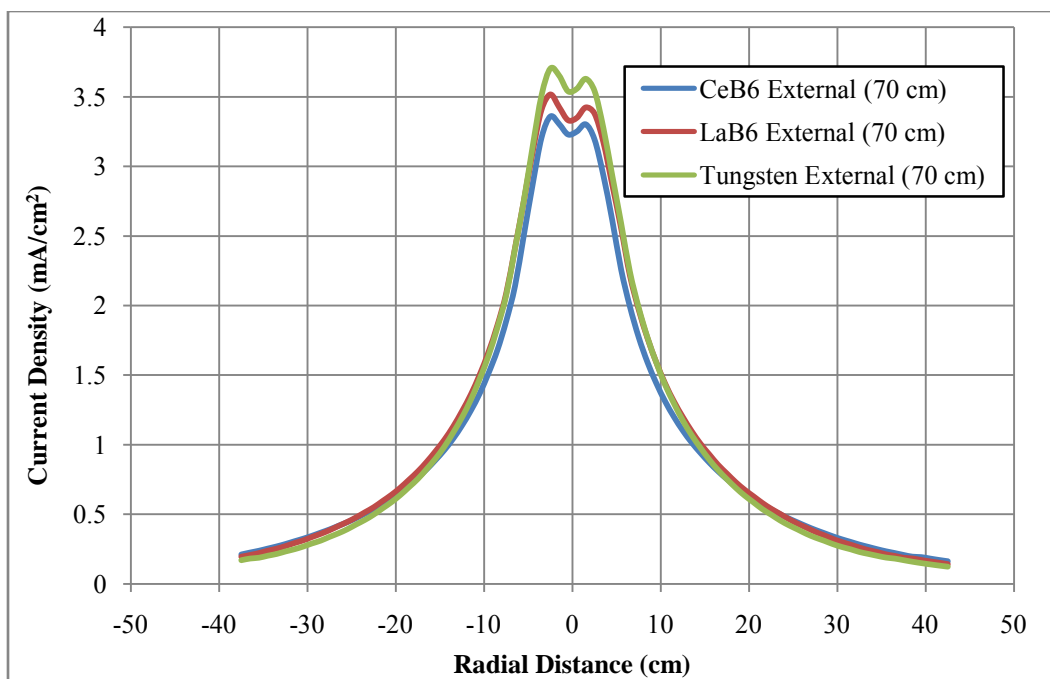


Figure 36. Current Density with Externally-Mounted Cathodes at 70 cm Axial Distance

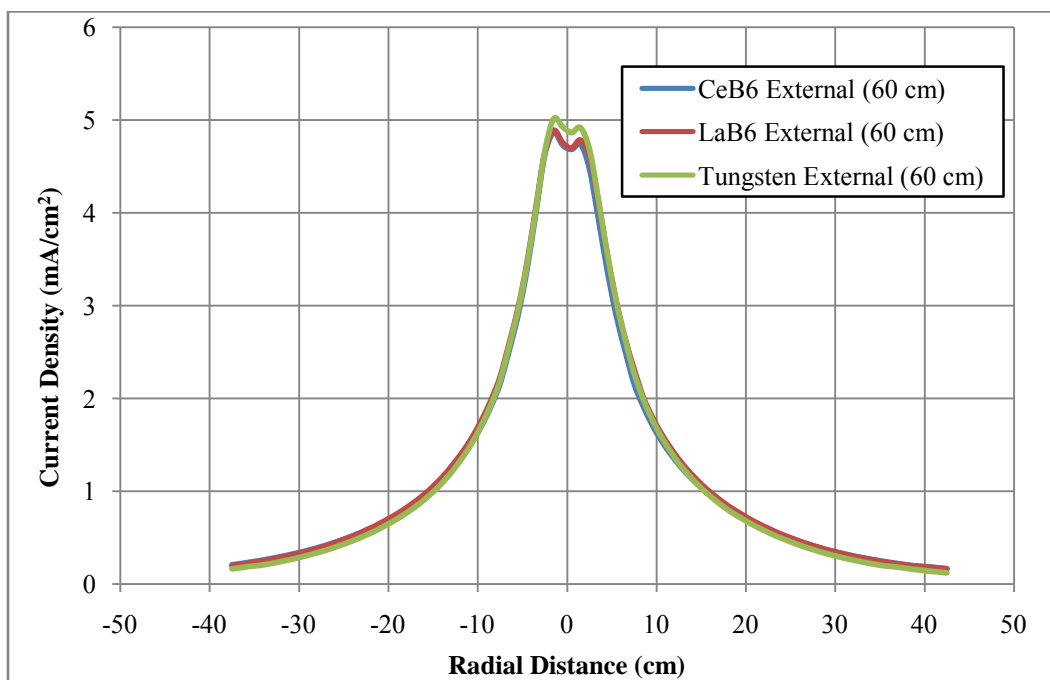


Figure 37. Current Density with Externally-Mounted Cathodes at 60 cm Axial Distance

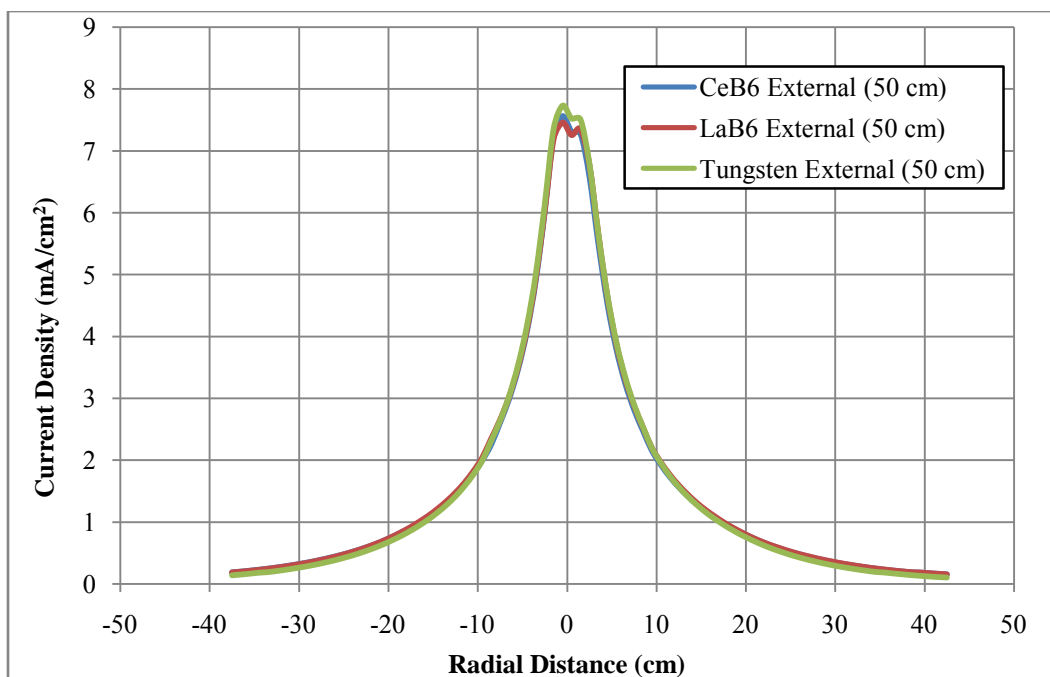


Figure 38. Current Density with Externally-Mounted Cathodes at 50 cm Axial Distance

Looking just at the two internally-mounted cathodes, the results are as expected. CeB₆ has a higher peak current density than LaB₆ at all axial distances. This cannot be solely attributed to the lower work function of CeB₆, however, as there were unexplained oscillations when operating with the LaB₆ cathodes. Figure 39 shows the current density profiles for both internally-mounted cathodes at a single axial distance.

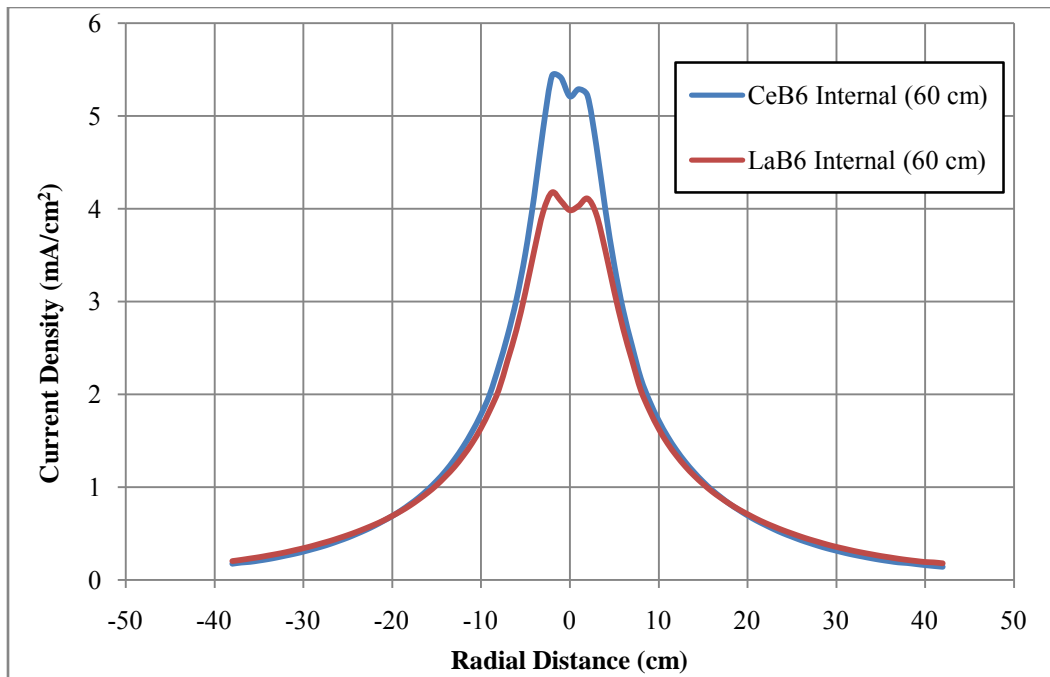


Figure 39. Current Density with Internally-Mounted Cathodes at 60 cm Axial Distance

Comparing the two geometries for cathode installation against one another for a given cathode insert material allows us to examine the effects on the plume based on the cathode geometry. With an internally-mounted cathode we would expect to see a more symmetric current density profile. For all of the Faraday data corresponding to the externally-mounted cathodes, the cathode was installed on the $-r$ side of the thruster centerline.

For the CeB_6 cathodes, the internally-mounted case gives us a higher peak current density relative to the externally-mounted cathode as axial distance is increased, although at 50 cm (52 cm for the internally-mounted cathode) the current density distributions were nearly identical. Interestingly, the current density distribution for the internally-mounted cathode did not appear to be any more symmetric than the external case as illustrated by Figure 40 through Figure 42. The current distribution for the externally-

mounted cathode actually appears quite symmetric as the axial distance is increased, as evidenced by Figure 40.

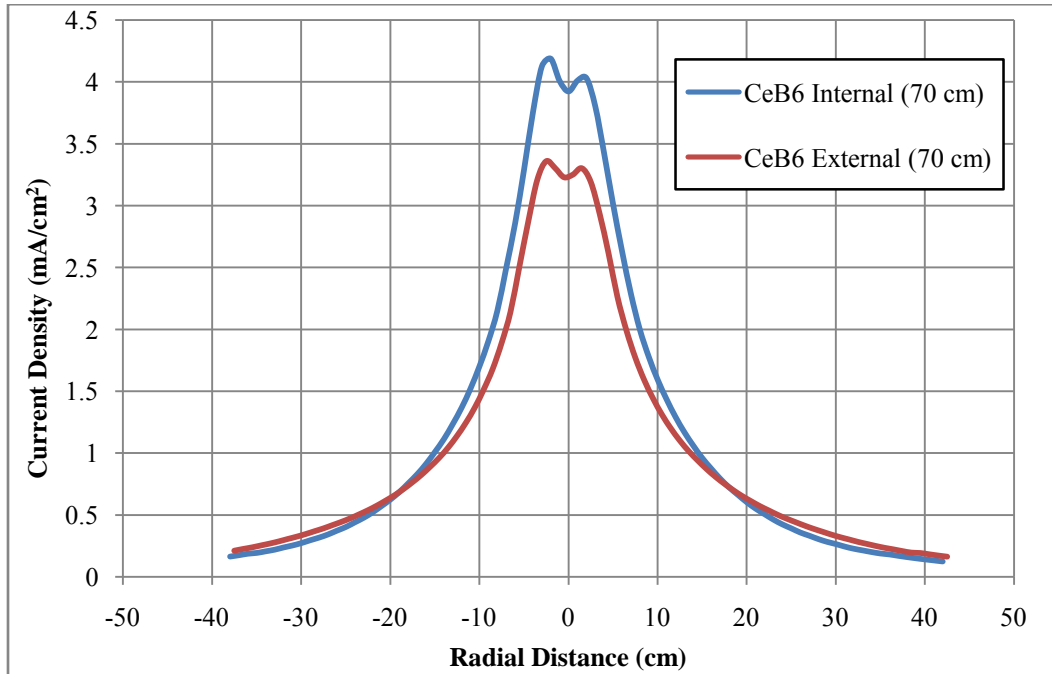


Figure 40. Current Density with CeB₆ cathode at 70 cm Axial Distance

This absence of symmetric current density distribution for the internally-mounted cathode has several possible explanations. It is possible that the orifice plate had been sputter eroded such that the opening was no longer symmetric. Uneven heating of the insert or slight misalignment of the cathode tube when mounting it to the base plate could also induce asymmetries in the plume.

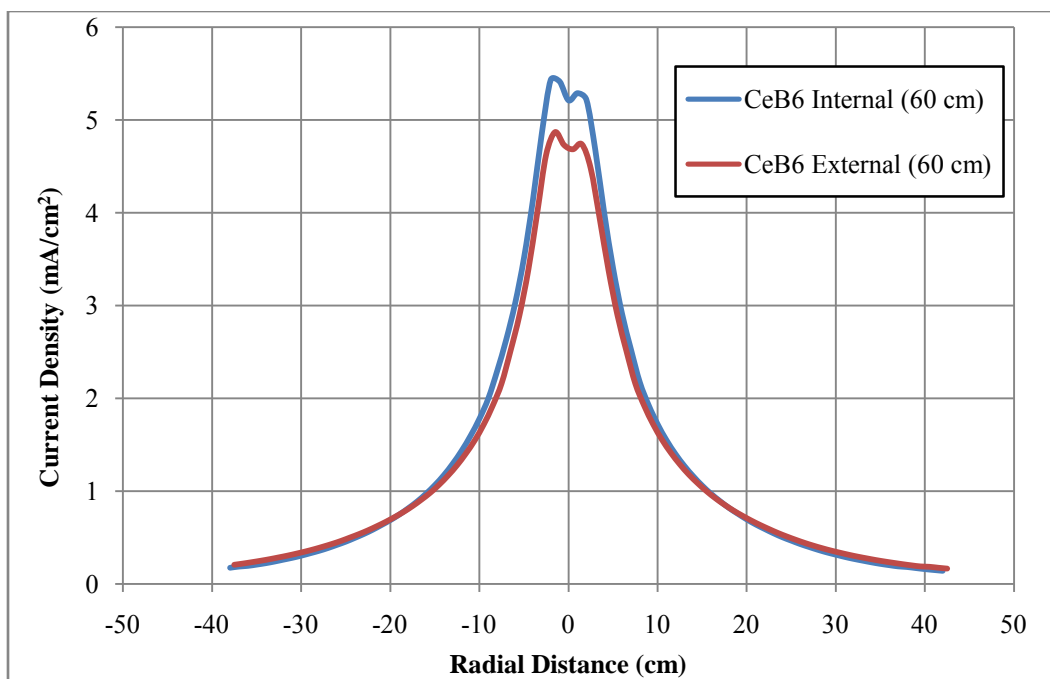


Figure 41. Current Density with CeB₆ cathode at 60 cm Axial Distance

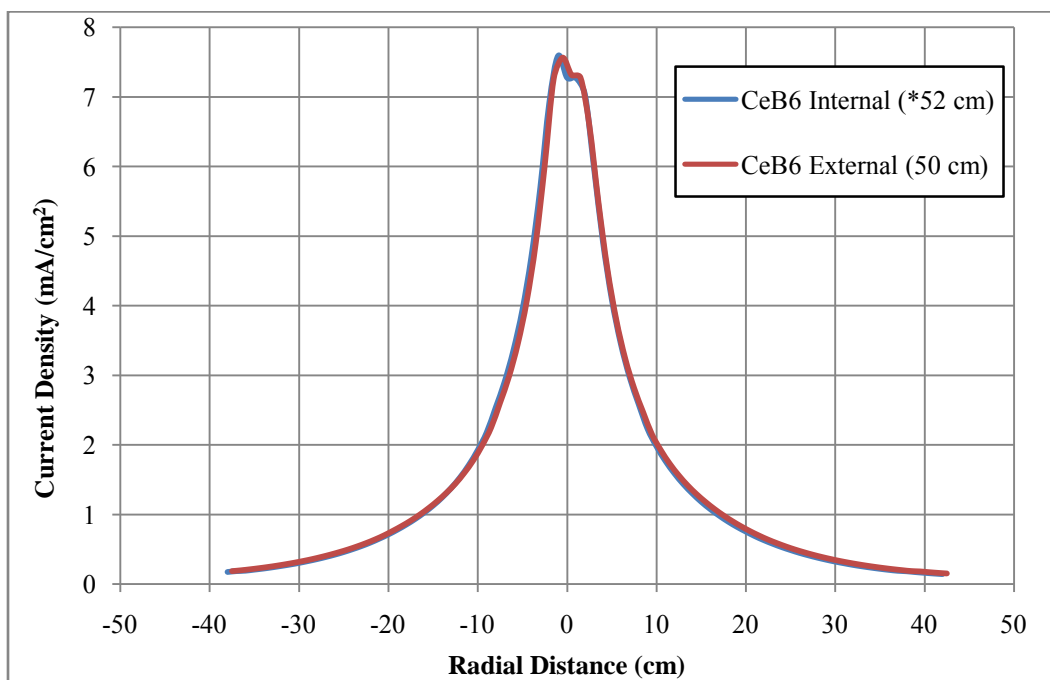


Figure 42. Current Density with CeB₆ cathode at 50 cm Axial Distance

The LaB₆ cathodes showed some peculiarities in both geometries. At all axial distances, the externally-mounted cathode developed a higher peak current density than the internally-mounted cathode. The internally-mounted LaB₆ cathode, again, showed the most symmetry of all the test cases. This symmetry, however, was diminished as the axial distance decreased.

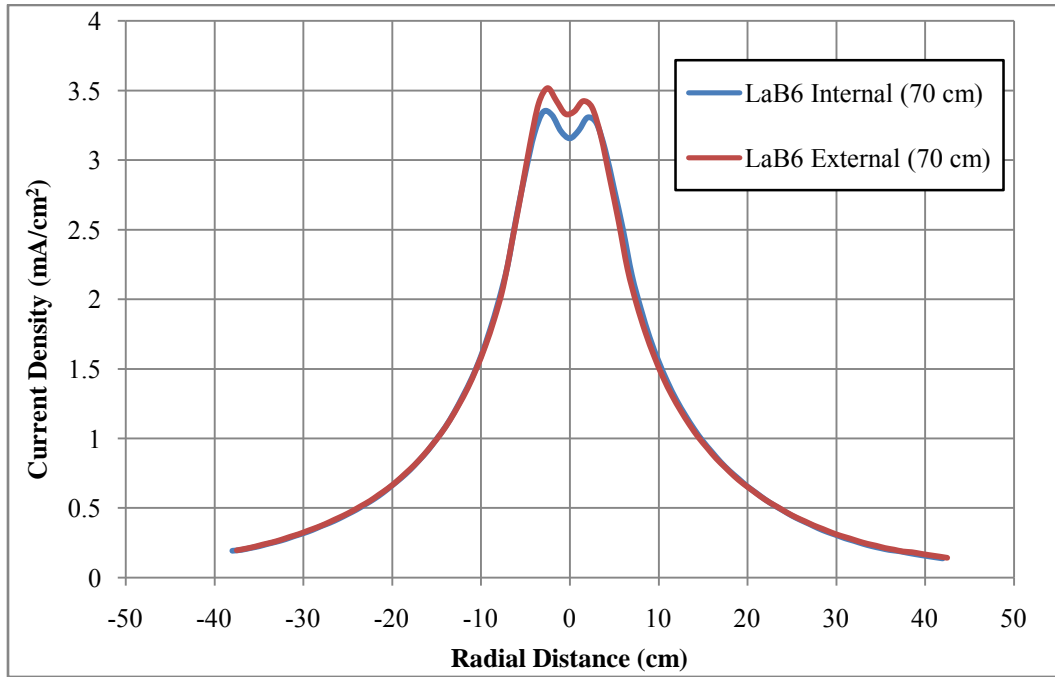


Figure 43. Current Density with LaB₆ cathode at 70 cm Axial Distance

Figure 43 through Figure 45 indicate the higher peak current density of the thruster when configured with the externally-mounted LaB₆ cathode.

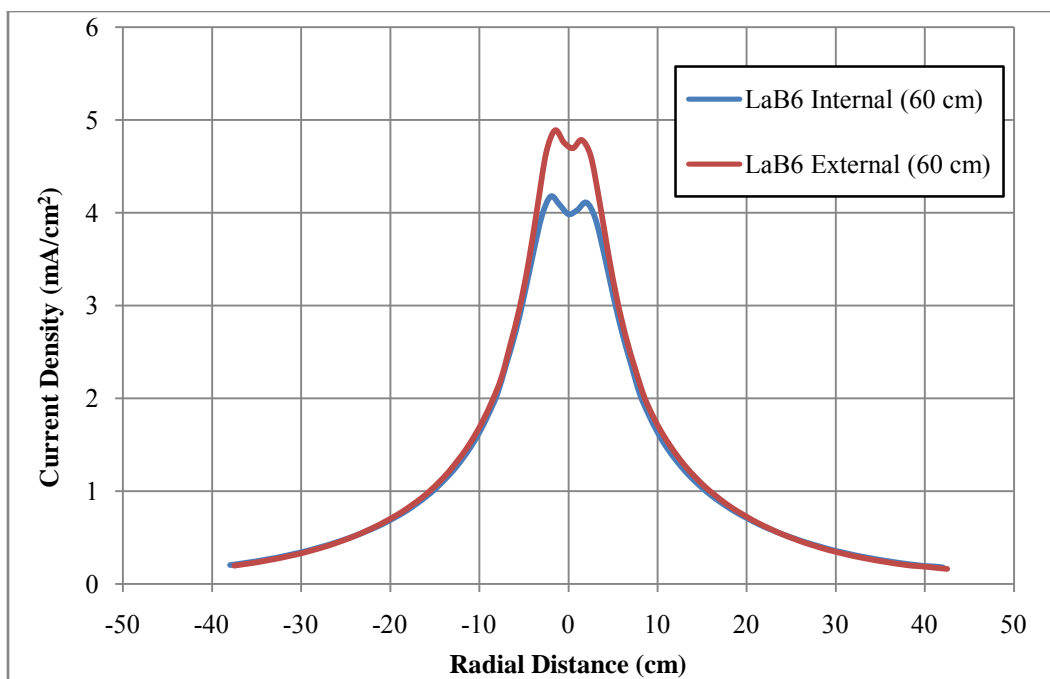


Figure 44. Current Density with LaB₆ cathode at 60 cm Axial Distance

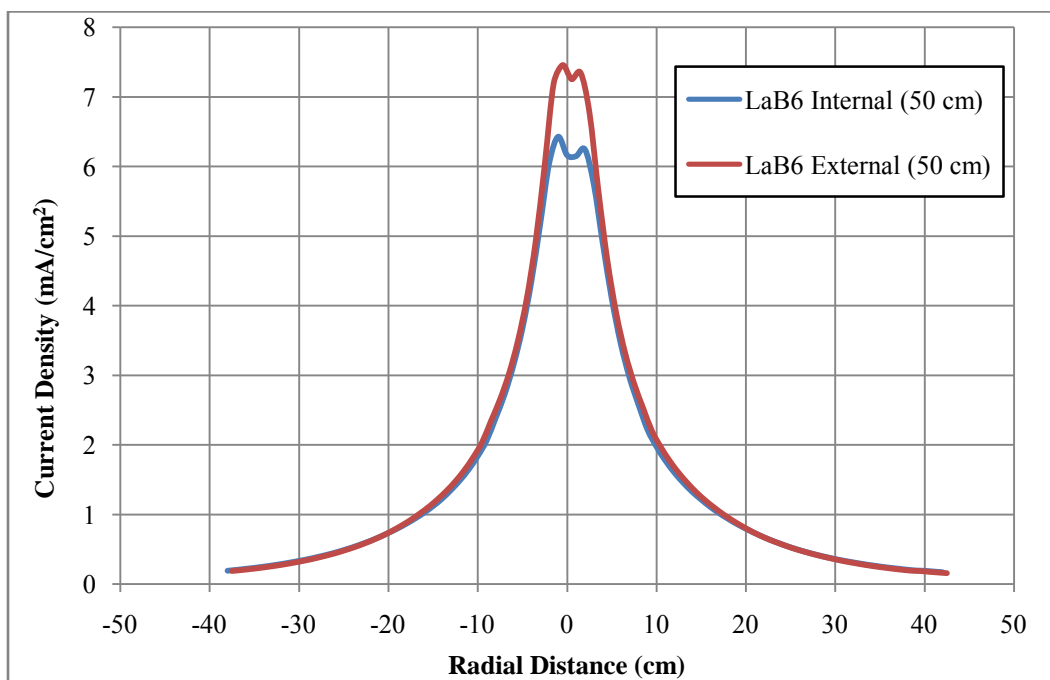


Figure 45. Current Density with LaB₆ cathode at 50 cm Axial Distance

In order to calculate a total beam current, the measured current density distributions were integrated for each test case at each axial distance. In order to capture the full beam current passing through a plane normal to the centerline of the thruster, we would need to integrate an infinite distance in all directions. As this is not possible with empirical data, the computed values are somewhat less than the actual beam current. Using the work of Azziz, the author was able to see approximately how much current was unable to be measured. Azziz conducted research using a BHT-1500 hall thruster and operated at nearly identical conditions to those in this work. [61] In his work, a Faraday probe was used to measure the current density of the plume for a full 180 degree arc at 1 m. The total beam current he calculated was 1.64 A. [61]

Since the data taken in this research was limited to axial distances from 50 to 70 cm, an exponential curve fit was used to extrapolate the data out to 1 m. The curve fit is only valid for a range of axial distances and will break down as the axial distance to the thruster is decreased. This is due to the near field effects of charge-exchange collisions and magnetic influences. For each geometry of CeB_6 , Figure 46 and Figure 47 show the integrated beam current calculated from the Faraday data along with a curve fit for that data and a corresponding curve based on the Azziz measured beam current using the exponential coefficient derived from this research.

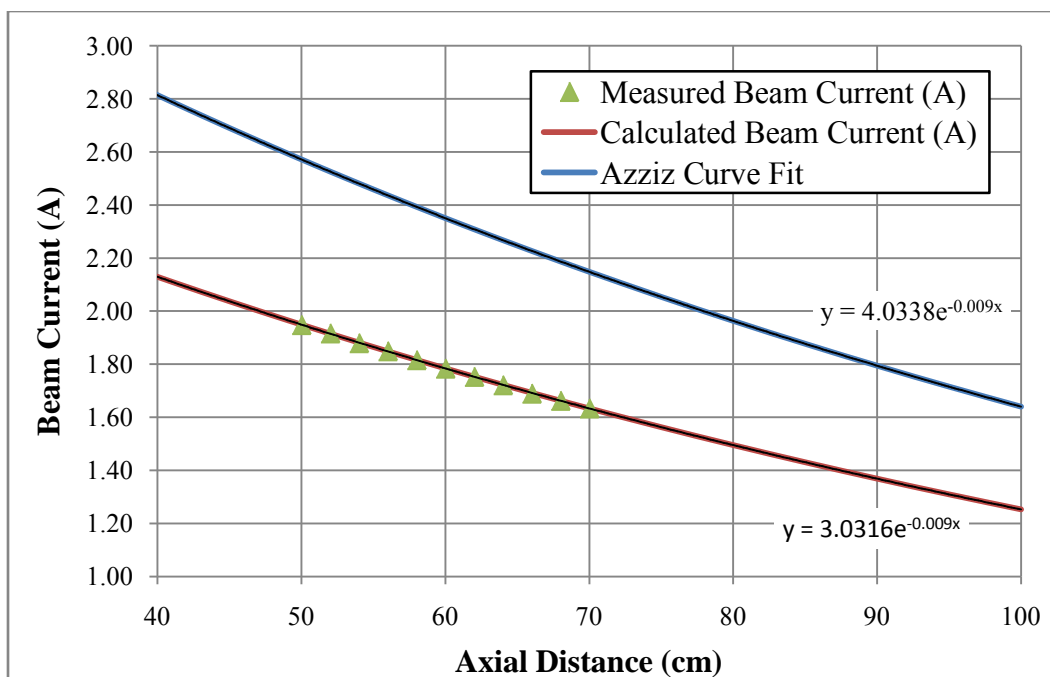


Figure 46. Total Beam Current vs. Axial Distance for Externally-Mounted CeB₆

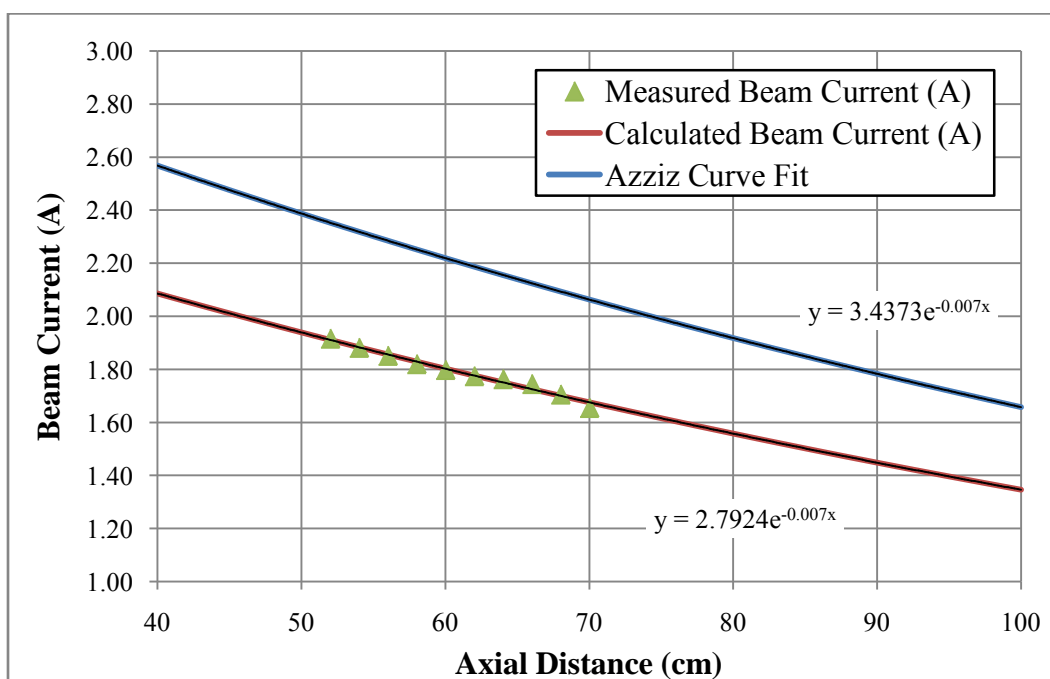


Figure 47. Total Beam Current vs. Axial Distance for Internally-Mounted CeB₆

Table 2 lists the integrated beam current for each test case at the three axial distances used for the figures above. All the values are reasonably close together and the difference between the extrapolated value at 100 cm that is based on the data collected and the Azziz data is fairly consistent. Since the entire beam current could not be calculated from empirical data, a true value for the beam current efficiency cannot be determined, but comparisons can be made between the various test cases.

Table 2. Integrated Beam Current (Amps)

Axial Distance	Cathode Insert Material and Geometry				
	CeB ₆ (edge-mount)	LaB ₆ (edge-mount)	Impregnated W (edge-mount)	CeB ₆ (center-mount)	LaB ₆ (center-mount)
50 cm	1.948	1.979	1.861	1.916	1.933
60 cm	1.784	1.821	1.700	1.799	1.779
70 cm	1.634	1.689	1.595	1.656	1.680
100 cm (extrapolated)	1.253	1.354	1.271	1.347	1.374
ΔJ from Azziz Work	0.387	0.286	0.391	0.311	0.266

One of the goals of using an internally-mounted cathode is to improve efficiency by decreasing losses due to plume divergence. We should expect to see a more highly collimated beam with an internally-mounted cathode. The Full-Width, Half-Max (FWHM) of the current density distribution for each test case at each axial distance was determined and plotted. To better model the asymmetries of the plume the half-max value of the current density for each side of the thruster was calculated independently. The radial distance corresponding to the half-max value was then determined and plotted. A linear curve fit was done for each side of the plume and the half-angle was determined. By comparing the half angles from either side of the thruster plume the degree of symmetry can be evaluated.

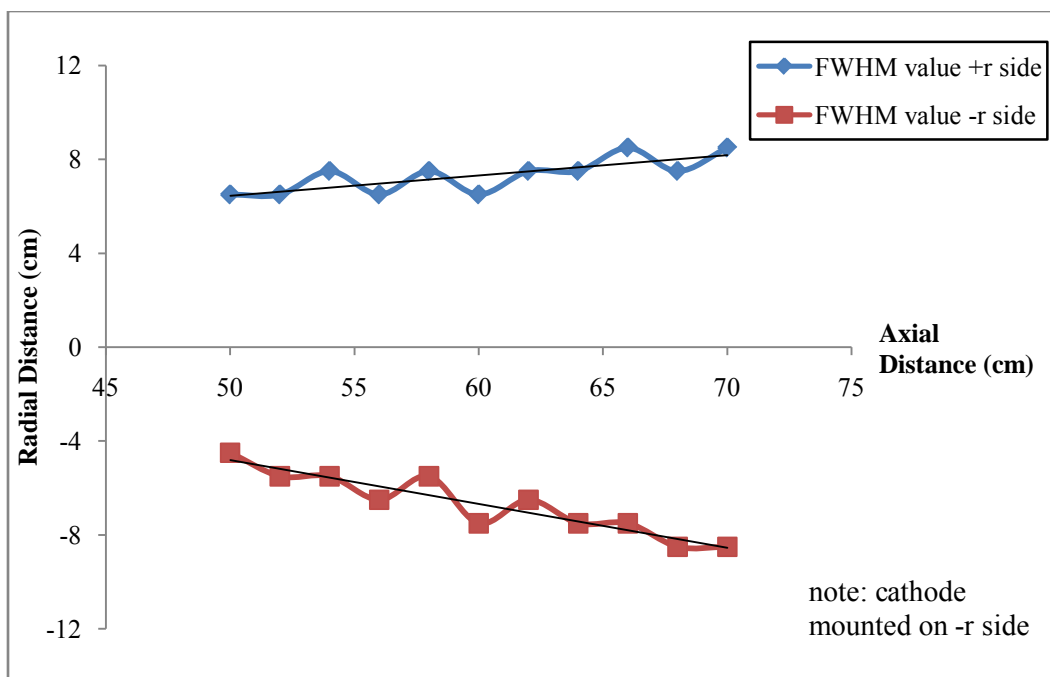


Figure 48. FWHM Plume Angle for Externally-Mounted CeB_6

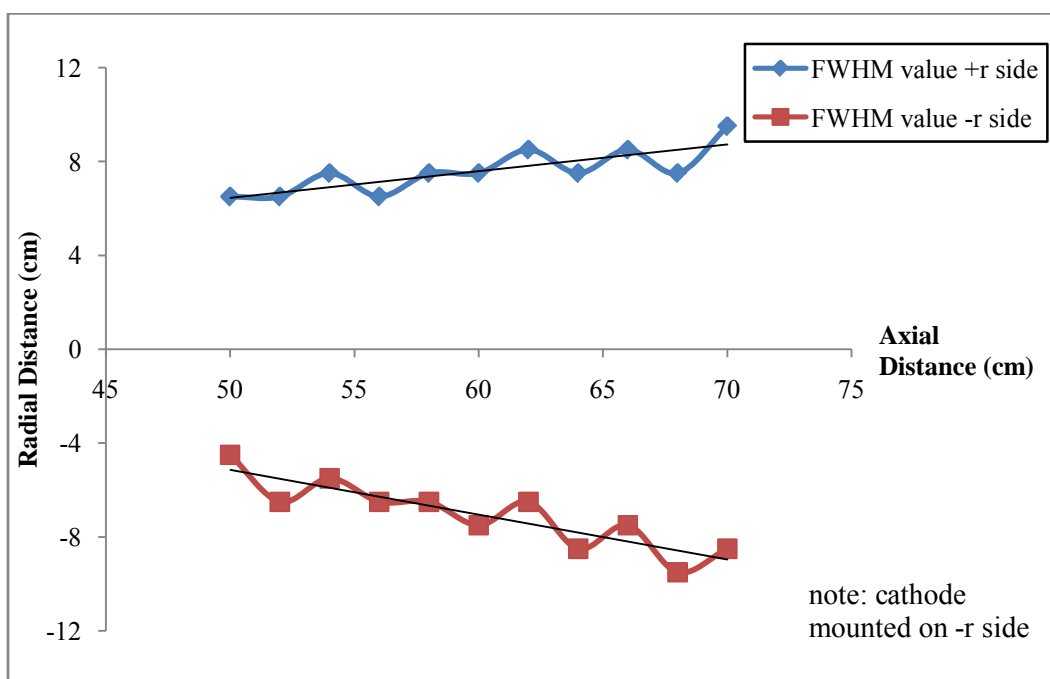


Figure 49. FWHM Plume Angle for Externally-Mounted LaB_6

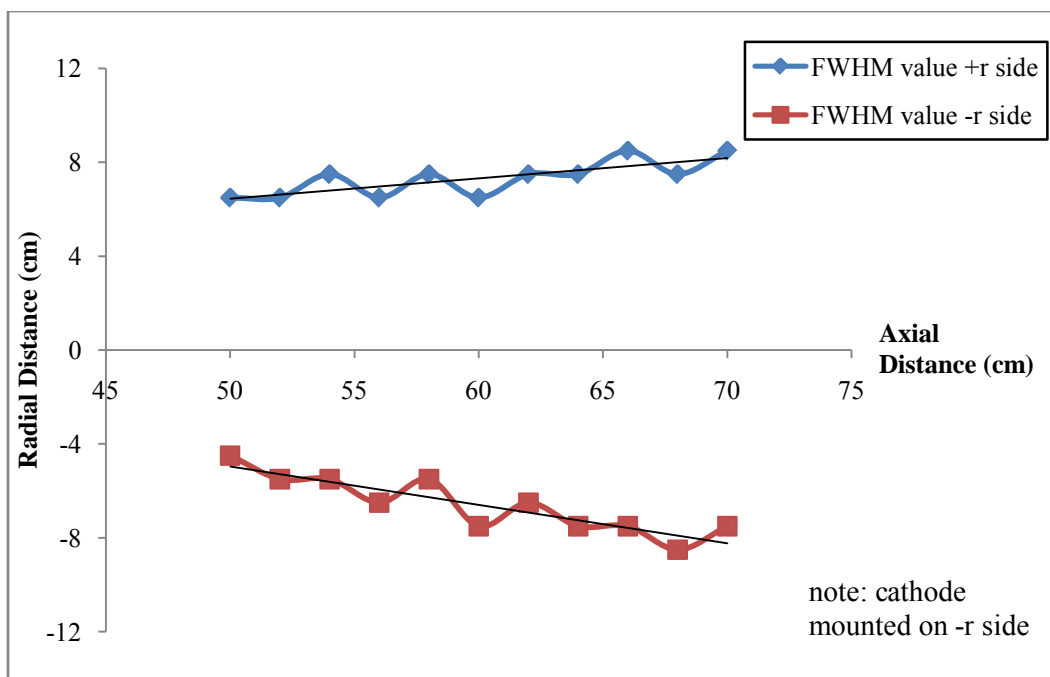


Figure 50. FWHM Plume Angle for Externally-Mounted Tungsten

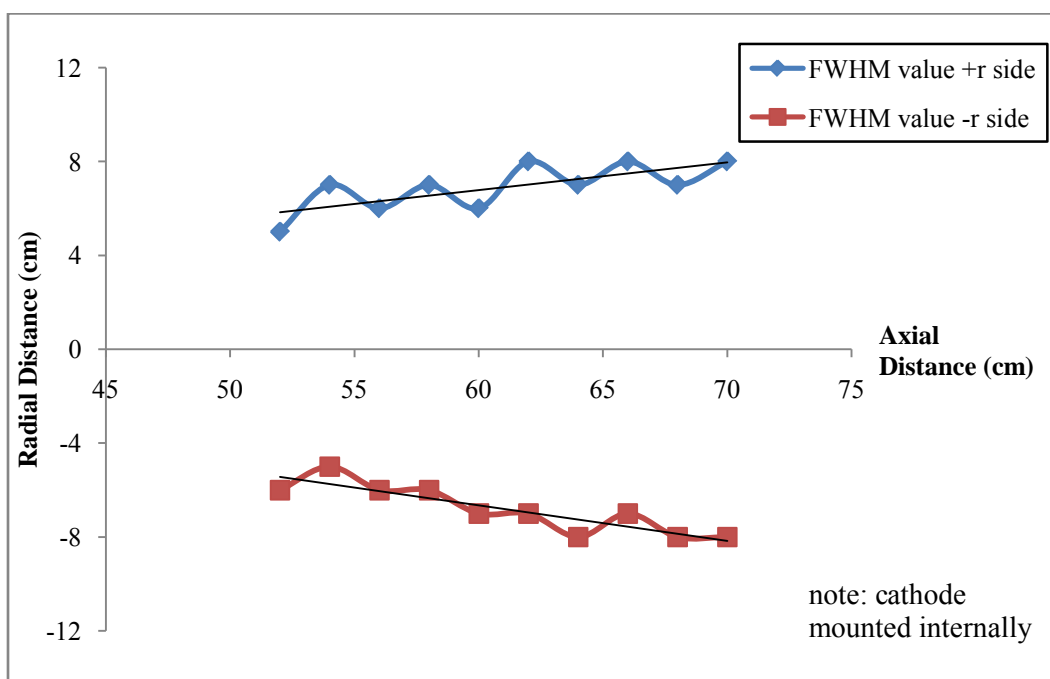


Figure 51. FWHM Plume Angle for Internally-Mounted CeB₆

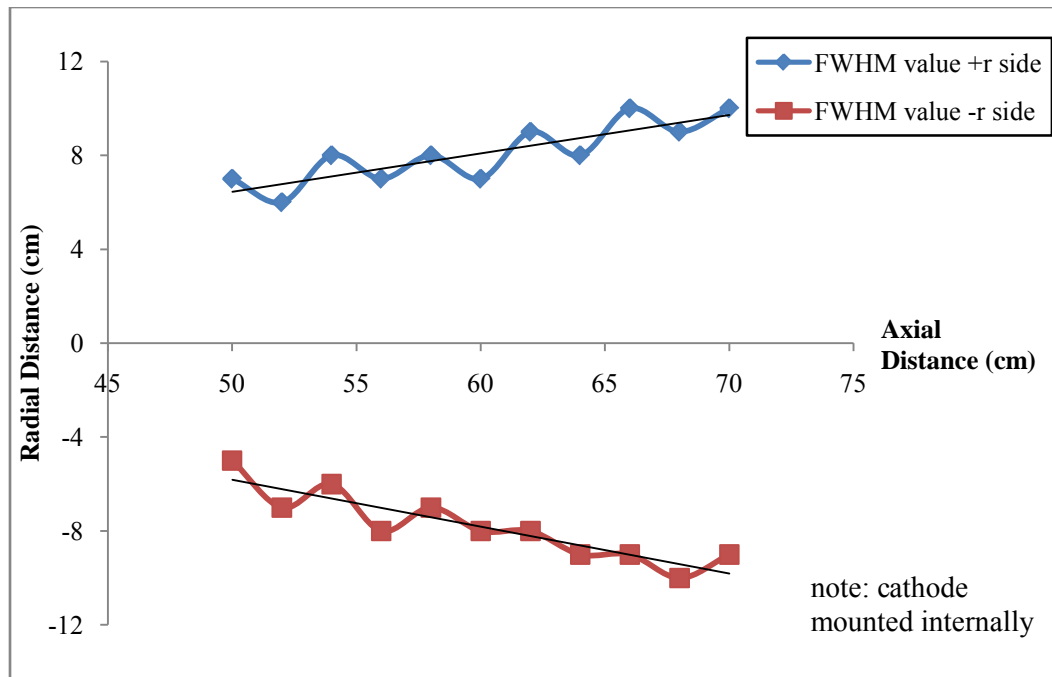


Figure 52. FWHM Plume Angle for Internally-Mounted LaB₆

For the externally-mounted cathodes in Figure 48 through Figure 50 the increased plume divergence on the cathode side is readily apparent. There still appears to be some asymmetry with the internally-mounted cathodes as evidenced by Figure 51 and Figure 52, but it is less pronounced.

Table 3. FWHM Plume Angles (degrees)

	Cathode Insert Material and Geometry				
	CeB ₆ (edge-mount)	LaB ₆ (edge-mount)	Impregnated W (edge-mount)	CeB ₆ (center-mount)	LaB ₆ (center-mount)
1/2 angle +r side	4.9	6.5	4.9	6.7	9.3
1/2 angle -r side	10.6	10.8	9.3	8.6	11.3
Total Angle	15.5	17.3	14.2	15.4	20.6
Δ angle from CL	5.6	4.3	4.4	1.9	2.0

Table 3 lists the both the positive and negative half-angles for each test case. For each test case the total angles are consistent except for the internally-mounted LaB₆ cathode. When looking at the difference between the positive and negative angles,

however, a trend emerges. The difference between the positive and negative half-angles for the internally-mounted cathodes are both less than half the difference of the half-angles for their respective externally-mounted cases. This would indicate a more highly collimated plume for the internally-mounted cases. This is further evidenced in that despite having the largest total FWHM angle, the internally-mounted LaB₆ cathode still had a difference between the positive and negative half-angles of just over 2.0 degrees. In the case of the internally-mounted CeB₆, the more highly collimated plume would account for the higher peak current densities seen further downstream in the plume even though the total beam current for all five cases was nearly identical. Likewise, the wider beam for the internally-mounted LaB₆ cathode would account for the lower current densities seen downstream.

Langmuir Probe Analysis

The single Langmuir probe provided data on the plasma that makes up the plume of the thruster. From this data, additional information was derived to determine performance characteristics of the thruster given the various cathode insert materials and cathode geometries. The plasma potential was measured and is used to determine the beam voltage, allowing the beam voltage efficiency to be calculated. This also allows for an exhaust velocity to be calculated allowing for certain assumptions. Ion number density was examined as well. It is key to determining the propellant utilization, as the more propellant delivered to the anode is ionized, the more efficient the thruster will be.

By subtracting the plasma potential from the discharge potential, we can calculate the beam voltage and subsequently calculate a beam voltage efficiency. This is given by;

$$V_d - V_p = V_b \quad (21)$$

where V_p is the plasma potential and V_d is the discharge potential, which for all test cases was 300 V. Knowing V_d and V_b the beam voltage efficiency, η_v , can be calculated using equation (9).

Figure 53 through Figure 55 show the plasma potential at increasing axial distance for all five test cases. A lower plasma potential is better allowing more beam potential to accelerate the ions. The 15 cm axial plot shows a spike along thruster centerline due to the coupling of the cathode to the discharge plasma. As axial distance increases this spike diminishes and a nearly constant plasma potential is seen.

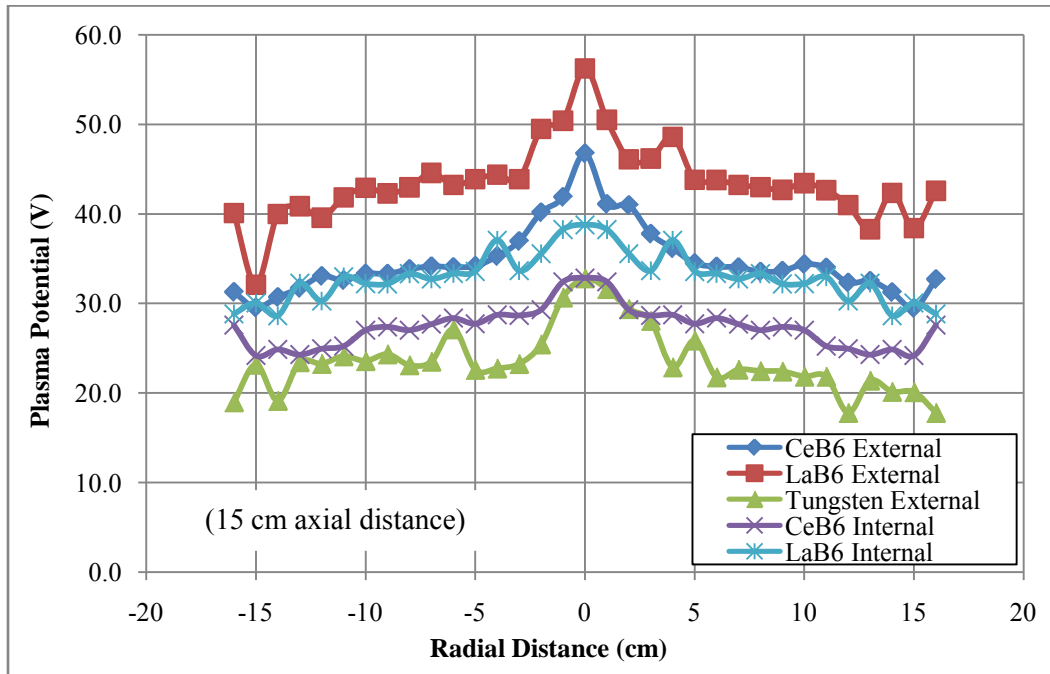


Figure 53. Plasma Potential at 15 cm Axial Distance

At 15 and 50 cm axial distance, the tungsten cathode gives the lowest plasma potential. Even through the other cases show a relatively constant plasma potential at 50 cm axial distance, the internally-mounted CeB₆ case shows a small spike in plasma

potential on centerline. Other than this small spike, the internally-mounted CeB₆ has the most stable plasma potential across the plume. The average standard error for the plasma potential measurements is 0.20 V.

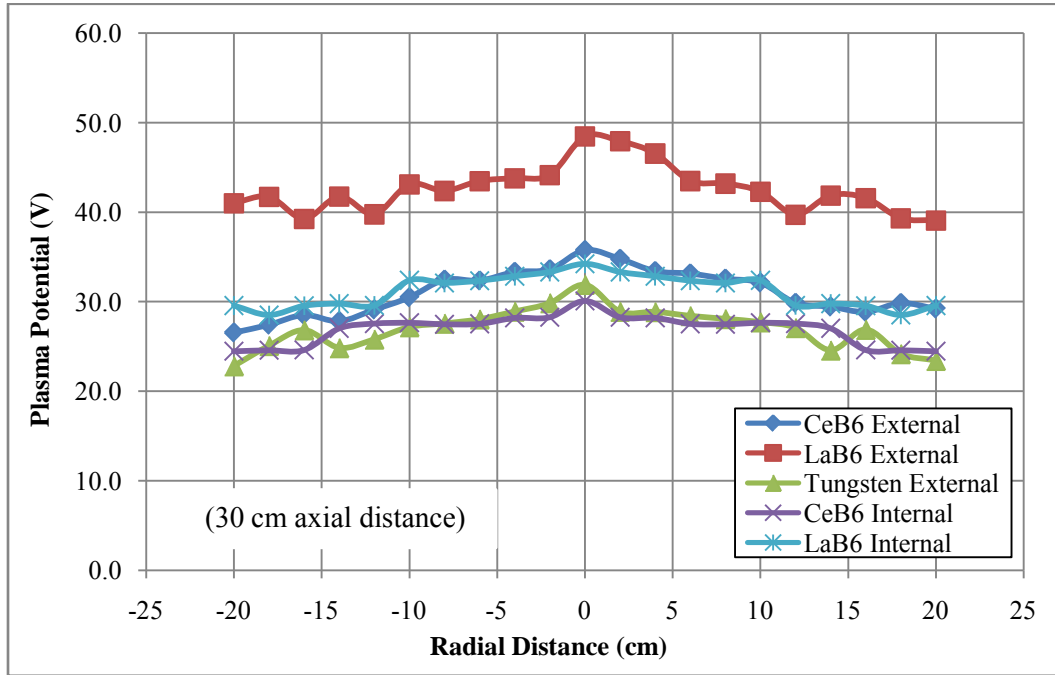


Figure 54. Plasma Potential at 30 cm Axial Distance

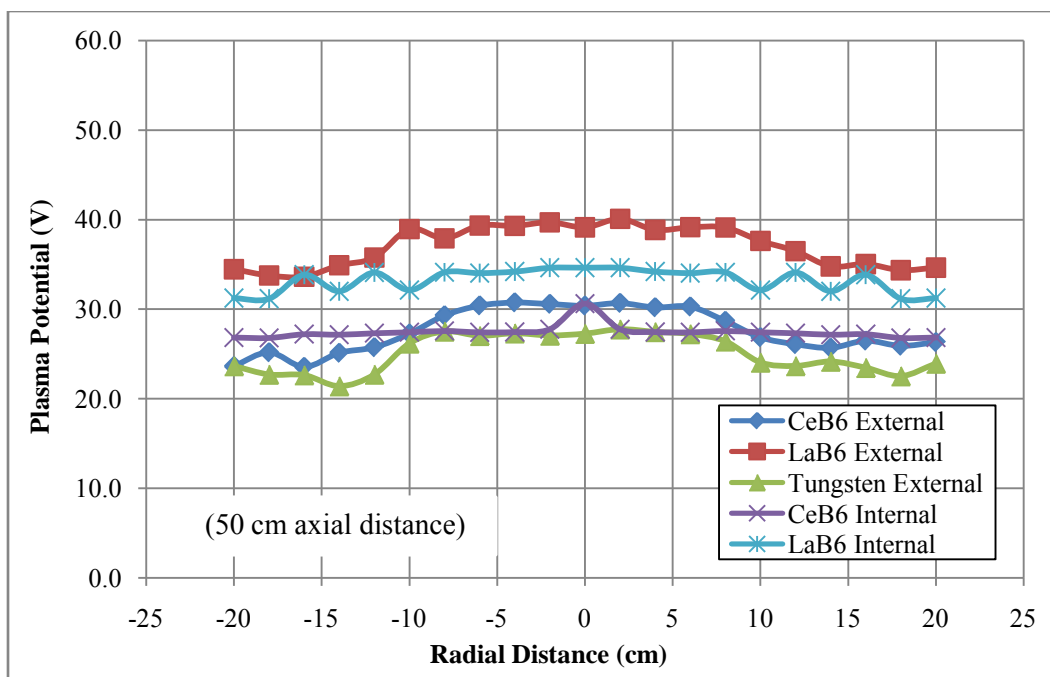


Figure 55. Plasma Potential at 50 cm Axial Distance

Looking at the average beam voltage versus axial distance, we see no clear trends. Figure 56 does show the internally-mounted CeB₆ case to, again, be the most stable, this time with respect to axial distance. Additionally, save for the 25 cm data, the tungsten case shows the highest beam voltage. The average standard error for the averaged beam voltages is 0.54 V.

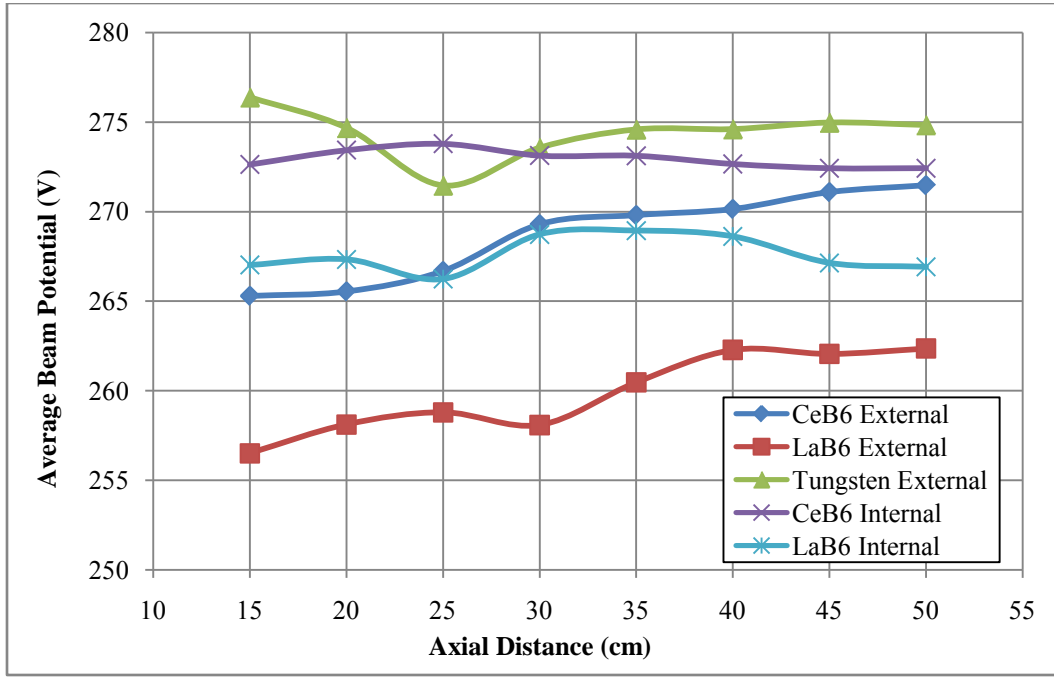


Figure 56. Average Beam Potential

Knowing the average beam voltage and mass of the xenon propellant, a velocity can be calculated using the following;

$$v_b = \sqrt{\frac{2e\bar{V}_b}{M}} \quad (22)$$

This assumes all of the xenon is singly-ionized and that it is all created at the average beam voltage. Neither of these assumptions is completely valid, but this gives a good first estimate of the velocity of the ions in the beam.

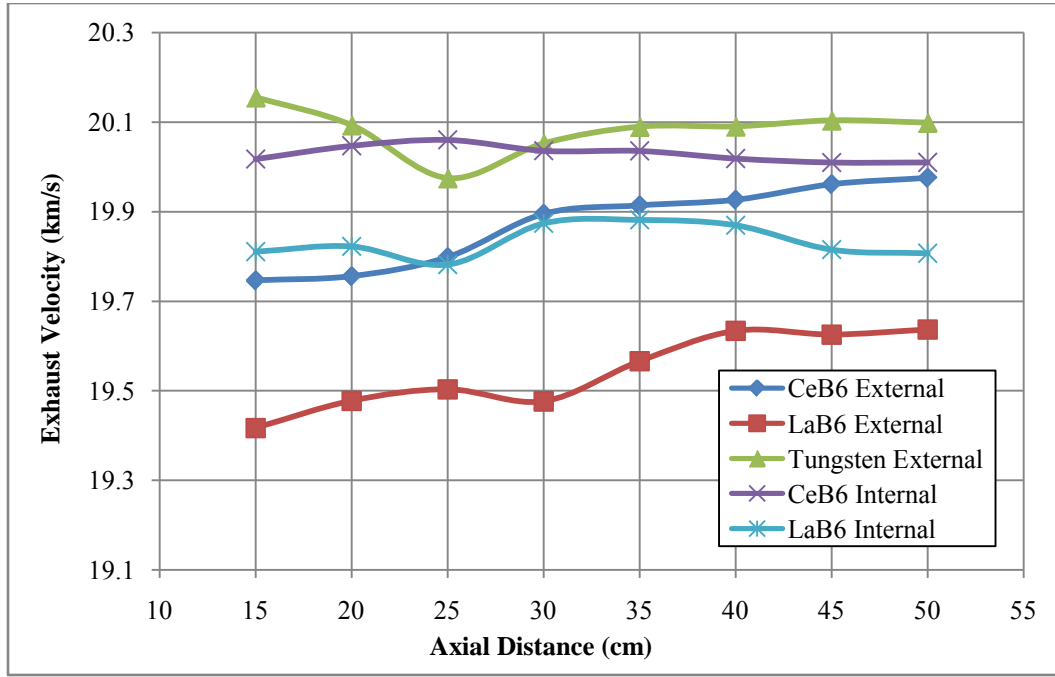


Figure 57. Average Beam Velocity versus Axial Distance

Figure 57 shows that the tungsten and internally-mounted CeB₆ cases yield the highest exhaust velocities. Interestingly, the externally-mounted LaB₆ had the lowest velocity. The ExB probe also allows us to calculate ion velocities. It can also determine the charge-state of the ions, therefore taking into account multiply-charged xenon ions. This will be examined in the next section.

Table 4. Beam Voltage (V), Efficiency, and Velocity

	Cathode Insert Material and Geometry				
	CeB ₆ (edge-mount)	LaB ₆ (edge-mount)	Impregnated W (edge-mount)	CeB ₆ (center-mount)	LaB ₆ (center-mount)
Average Beam Voltage	268.7	259.8	274.4	272.9	267.6
Discharge Voltage	300	300	300	300	300
Beam Voltage Eff. (η_v)	0.896	0.866	0.915	0.910	0.892
Average Velocity (km/s)	19.9	19.5	20.1	20.0	19.8

Table 4 summarizes the calculated and derived values from the plasma potential for each test case. The tungsten provides the highest efficiency and velocity, but the

internally-mounted CeB_6 is only slightly below these maximum values. Despite the results from the Faraday probe analysis, in the case of the Langmuir probe, it appears though the externally-mounted LaB_6 gives the lowest performance of the five cases, as we should expect.

Similar to the Faraday data, the ion number density data obtained via the Langmuir probe was integrated to get a total ion count at the specified axial distances. This integration is subject to the same limitations as the Faraday data, namely that we have planar data out to a limited radial distance. The Langmuir data was taken at closer axial distances, 15-50 cm, as opposed to 50-70 cm for the Faraday data, but the radial limits on the data collection were smaller. Still, comparisons can be made between the various test cases.

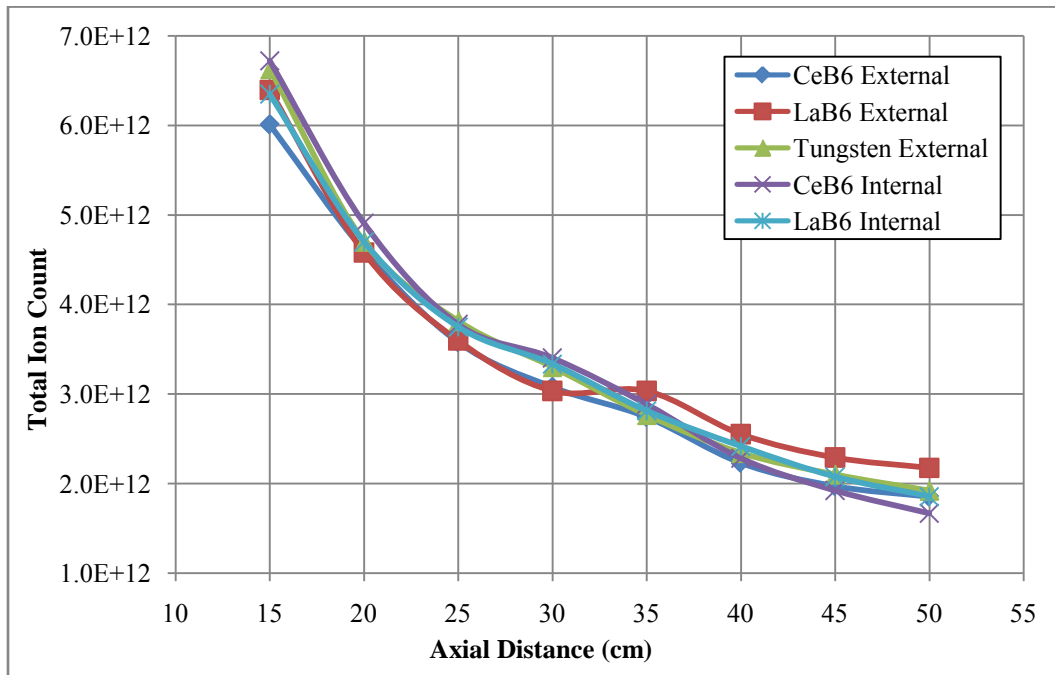


Figure 58. Total Ion Count versus Axial Distance

Figure 58 shows the total ion count obtained by integrating a circular area centered on the thrust axis based on the maximum radial distance examined at the specified axial distance. The trend of decreasing ion count as axial distance increases is to be expected. The standard error for this data set is $\pm 15.9\%$. To see how the ion count along the plume changed with axial distance the total ion count above was divided by the solid angle subtended by the circular area through which data was taken. This gives dimensions of ions per steradian.

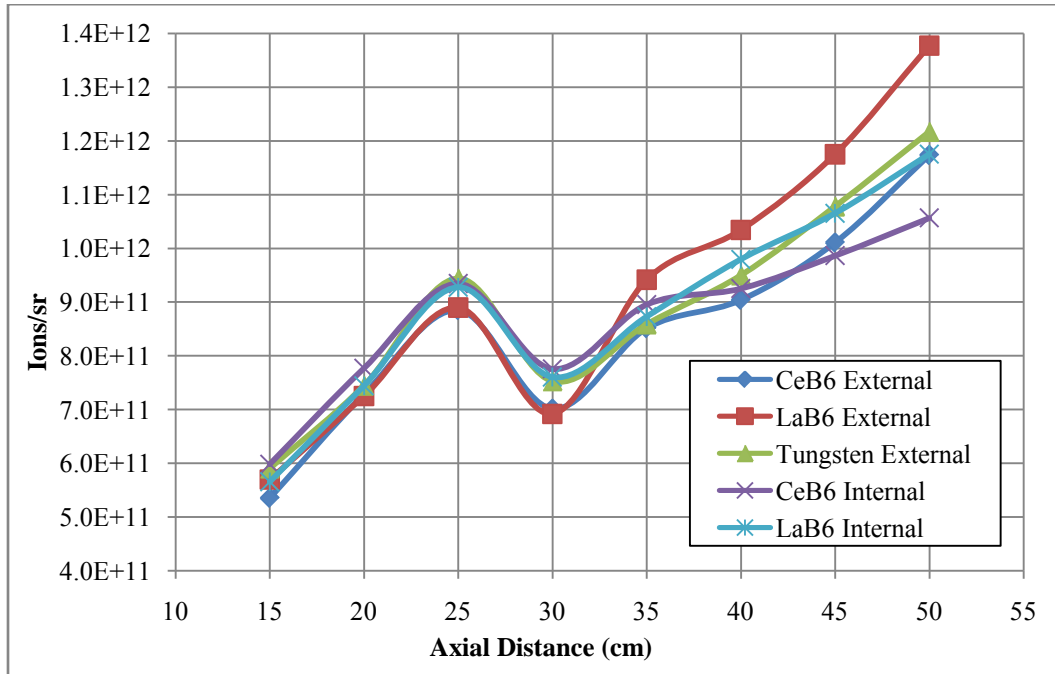


Figure 59. Ions/sr versus Axial Distance

Figure 59 shows the ions per steradian values for each of the five cases at each axial distance. The trend is expected since we are measuring along the thrust axis where the ion concentrations are the greatest in the plume and the solid angle is decreasing as the axial distance is increased. The negative slope from 25 to 30 cm axial distance is an artifact of the change in data collection from ± 16 cm to ± 20 cm radially. The standard

error for this data is $\pm 7.1 \times 10^{10}$ ions/sr. While all the test cases seem to be similar at smaller axial distances, the externally-mounted LaB₆ case shows a higher concentration of ions along the thrust axis at larger axial distances. This is an interesting result since the externally-mounted LaB₆ case had the largest beam angle, based on the Faraday data, of any of the externally-mounted cases. It does agree with the Faraday data as the externally-mounted LaB₆ case had the highest integrated beam current.

Various comparisons of the ion number density are presented below. The trends are generally what is expected except for the higher values for the externally-mounted LaB₆ case at the largest axial distances. In all of the externally-mounted cases, the cathode was mounted on the $-r$ side of the thruster. Figure 60 through Figure 62 show all five cases plotted at three axial distances.

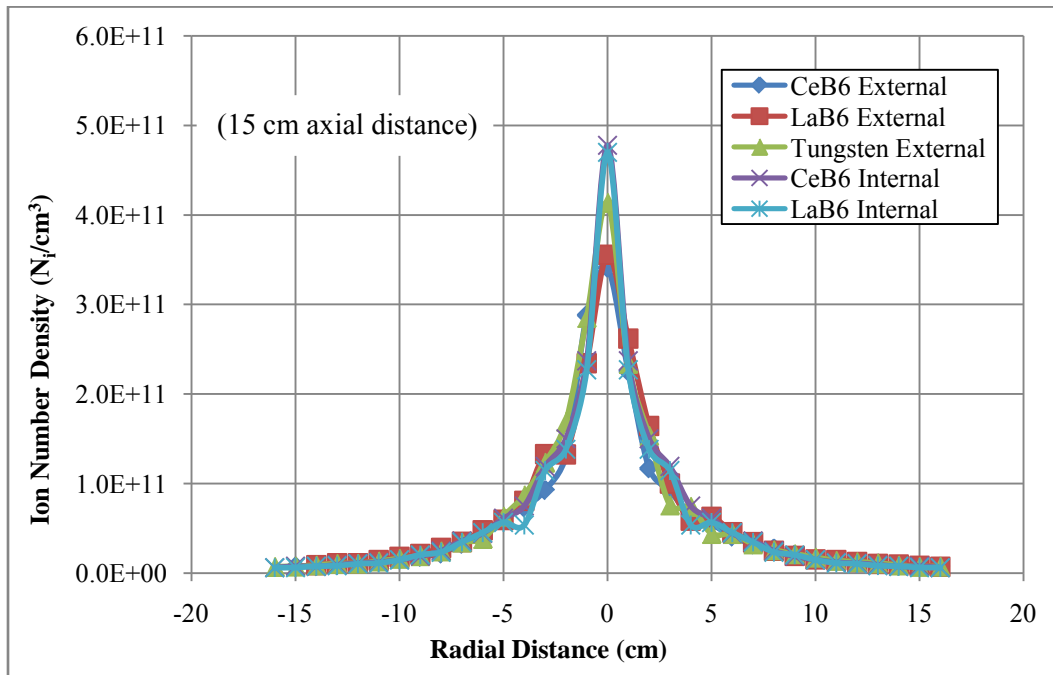


Figure 60. Ion Number Density at 15 cm Axial Distance

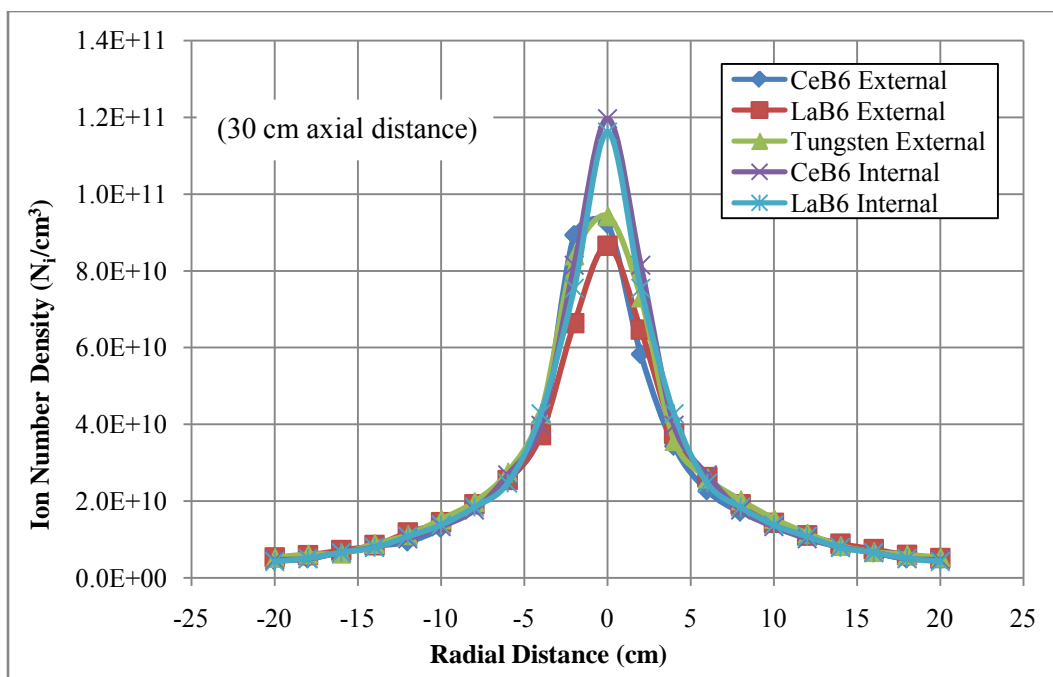


Figure 61. Ion Number Density at 30 cm Axial Distance

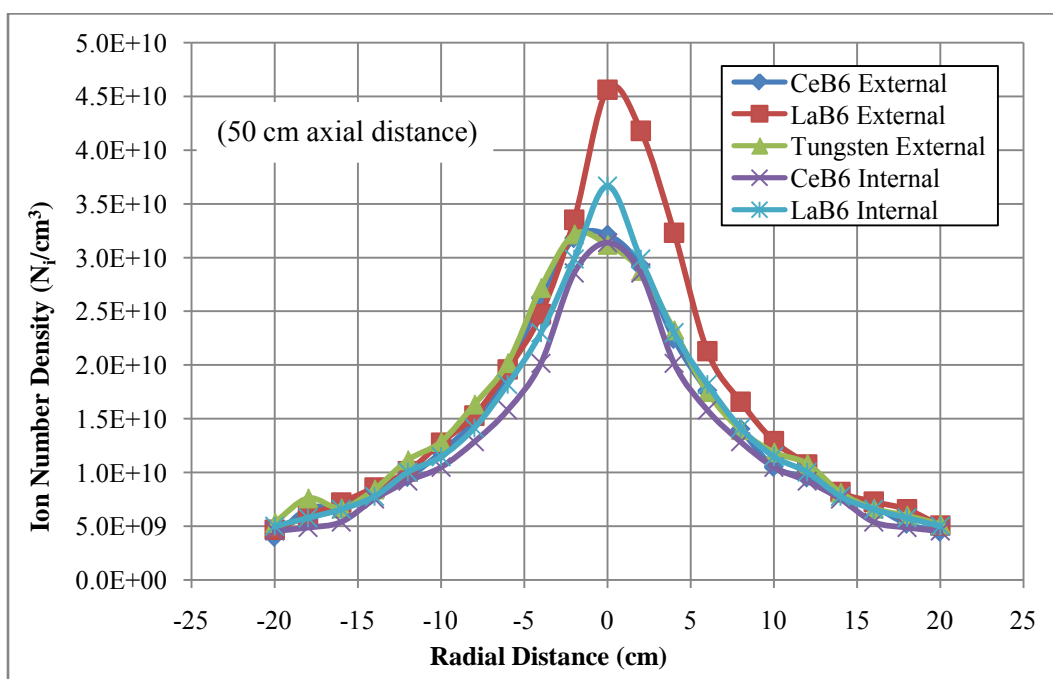


Figure 62. Ion Number Density at 50 cm Axial Distance

The standard error for the ion number density was calculated at each of the three axial locations illustrated in the figures presented here. At 15 cm, the standard error is $\pm 1.58 \times 10^{10} \text{ cm}^{-3}$, at 30 cm it is $\pm 6.19 \times 10^9 \text{ cm}^{-3}$, and at 50 cm it is $\pm 2.15 \times 10^9 \text{ cm}^{-3}$.

Looking at the externally-mounted cases, the tungsten has the highest number density in close, but the LaB₆ is significantly higher at 50 cm axial distance. The performance of the CeB₆ case is nearly identical to the tungsten except near the very center of the plume at the smaller axial distances. Figure 63 and Figure 64 both show the central peak for ion number density and, at the 15 cm axial distance, the distribution is quite symmetric. At 50 cm, however, the distribution is less symmetric, especially in the LaB₆ case.

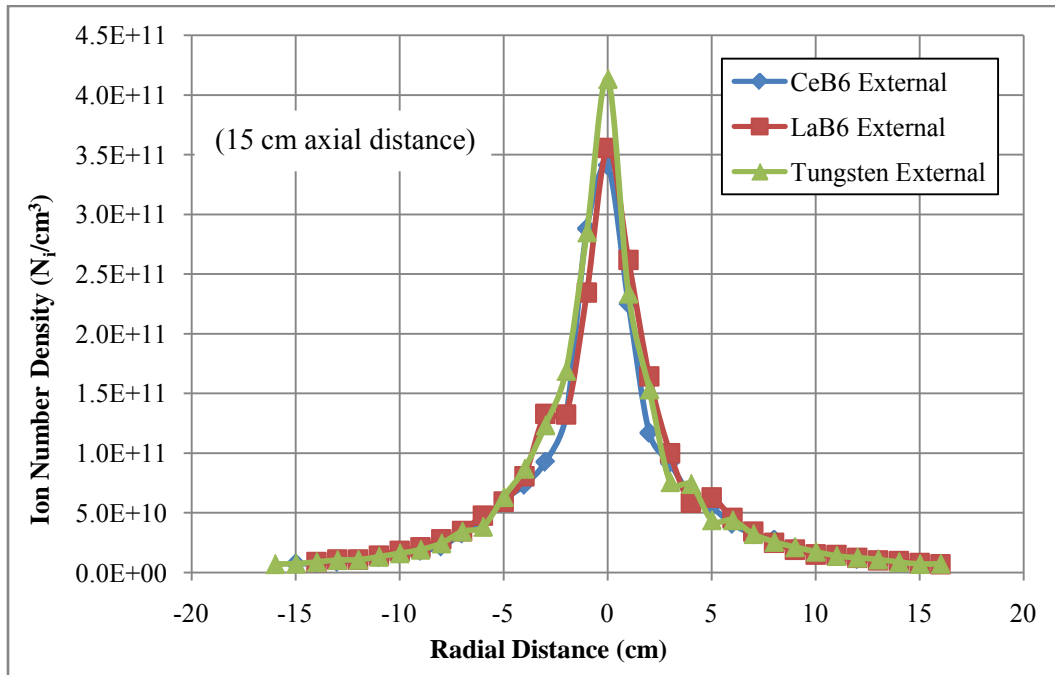


Figure 63. Ion Number Density with Externally-Mounted Cathodes at 15 cm Axial Distance

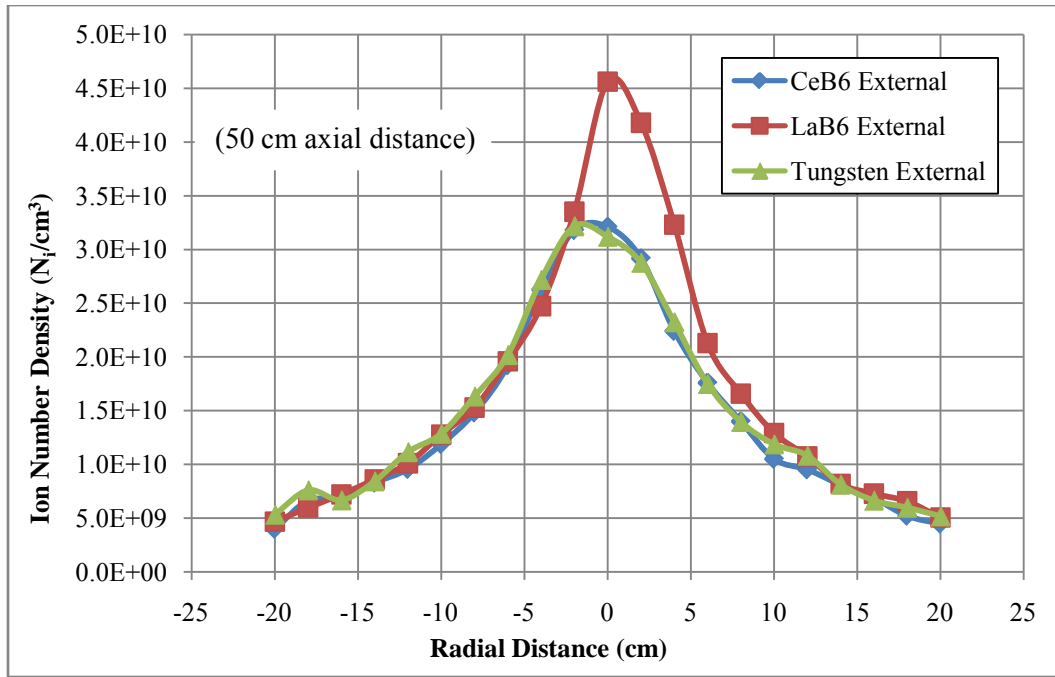


Figure 64. Ion Number Density with Externally-Mounted Cathodes at 50 cm Axial Distance

The distributions for the internally-mounted cases were virtually identical as axial distance decreased. As axial distance increased, however, the LaB₆ case showed higher peak ion number densities. Figure 65 shows the ion number density of the LaB₆ at all points to be higher than that of the CeB₆. The slightly higher beam current for the internally-mounted LaB₆ at the larger axial distances seen in the Faraday data, coupled with the increased divergence of the plume, may contribute to the higher ion number densities seen with the LaB₆ at larger axial distances.

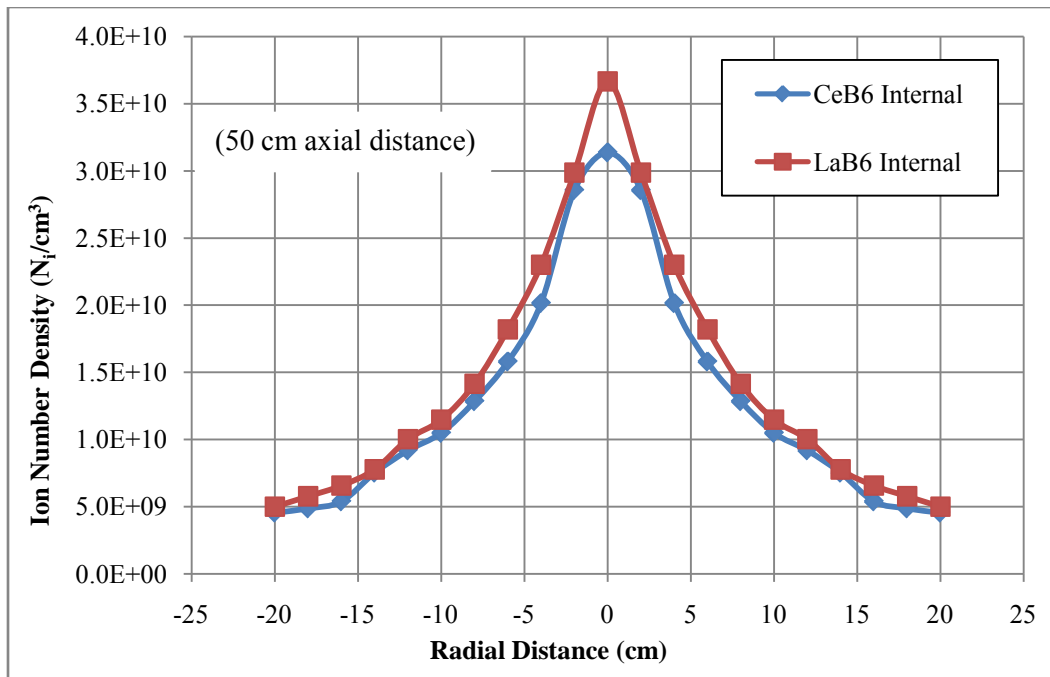


Figure 65. Ion Number Density with Internally-Mounted Cathodes at 50 cm Axial Distance

Examining the internal versus external case for the CeB_6 and LaB_6 respectively, we can see an additional trend. Both internal cases show a higher peak ion number density close to the thruster as seen in Figure 66 and Figure 67 as should be expected. Looking at the ion number density at 50 cm axial distance in Figure 68 and Figure 69, however, both the externally-mounted CeB_6 and LaB_6 cases show a higher ion number density at all points in the plume.

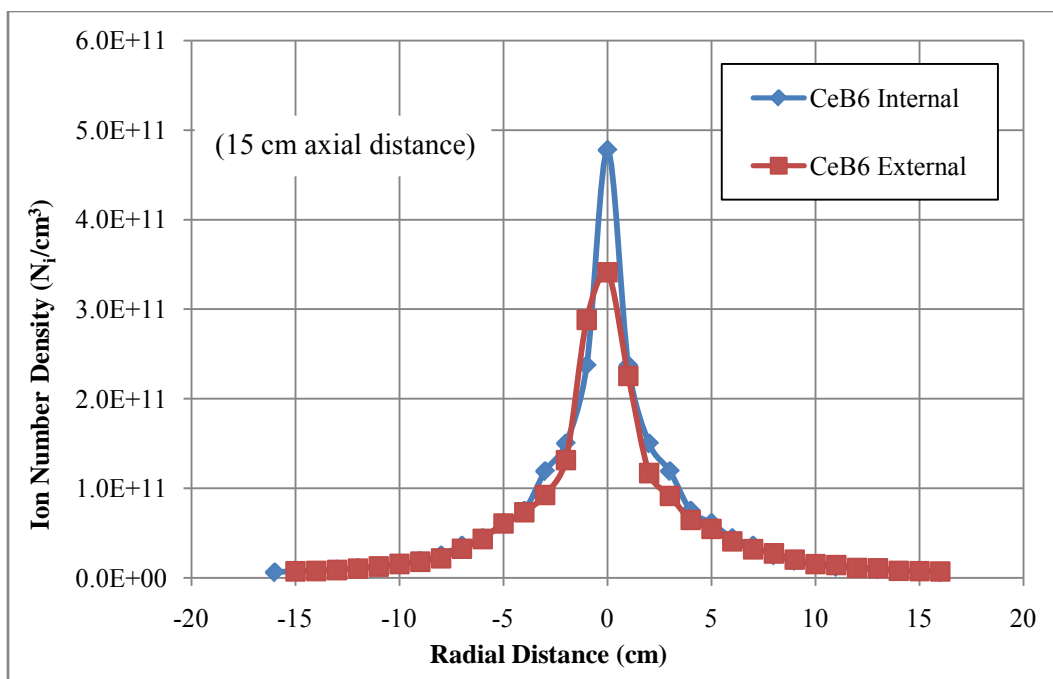


Figure 66. Ion Number Density with CeB₆ cathode at 15 cm Axial Distance

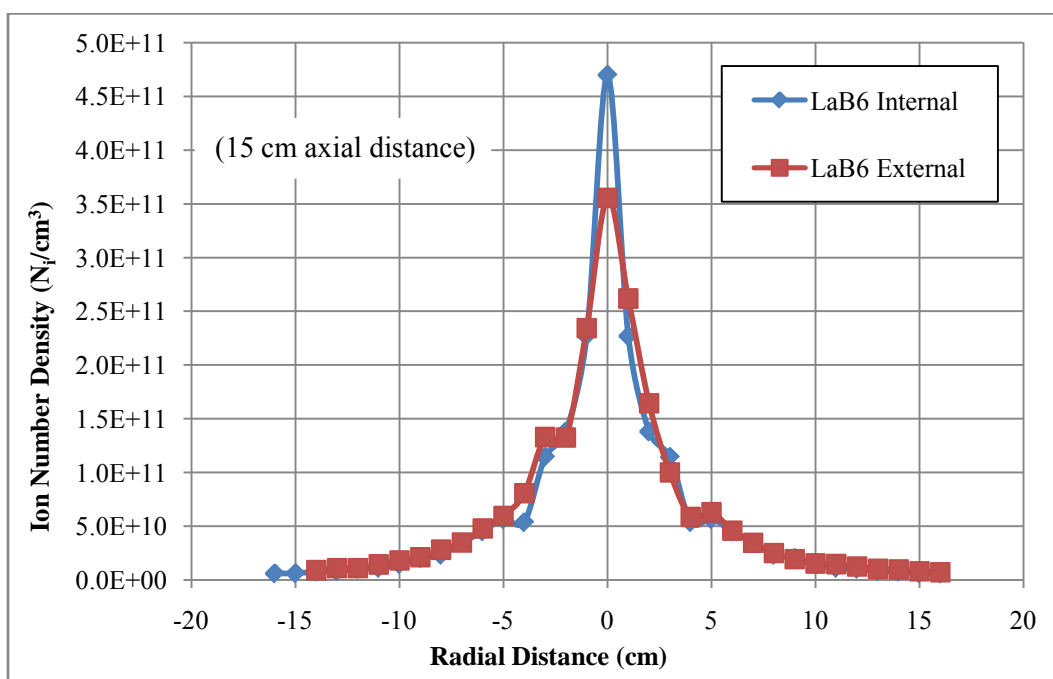


Figure 67. Ion Number Density with LaB₆ cathode at 15 cm Axial Distance

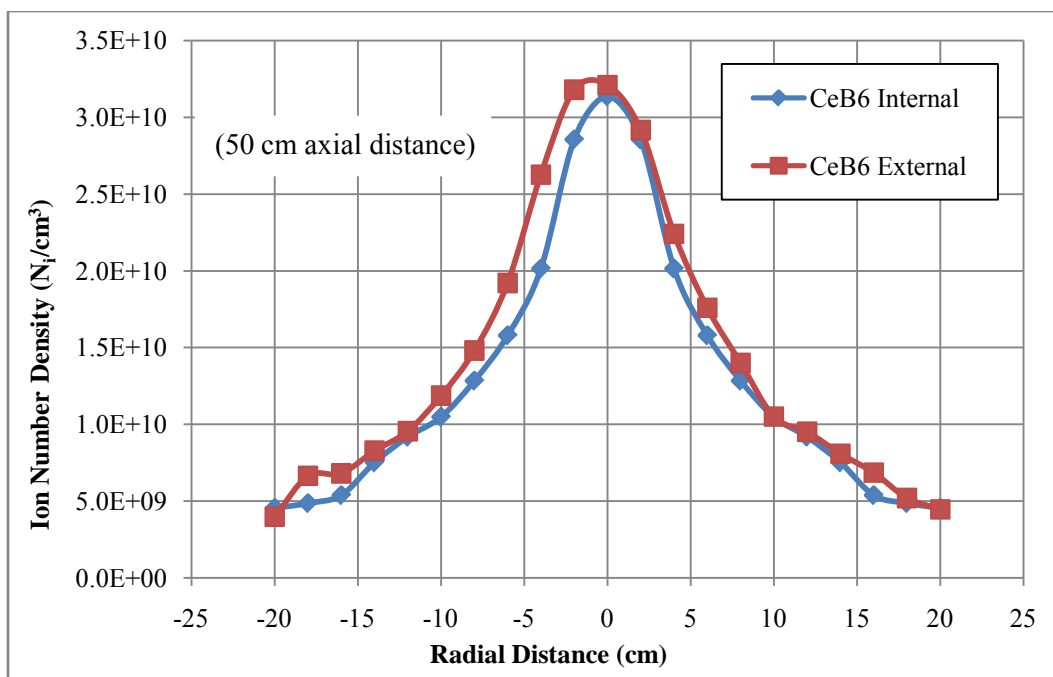


Figure 68. Ion Number Density with CeB₆ cathode at 50 cm Axial Distance

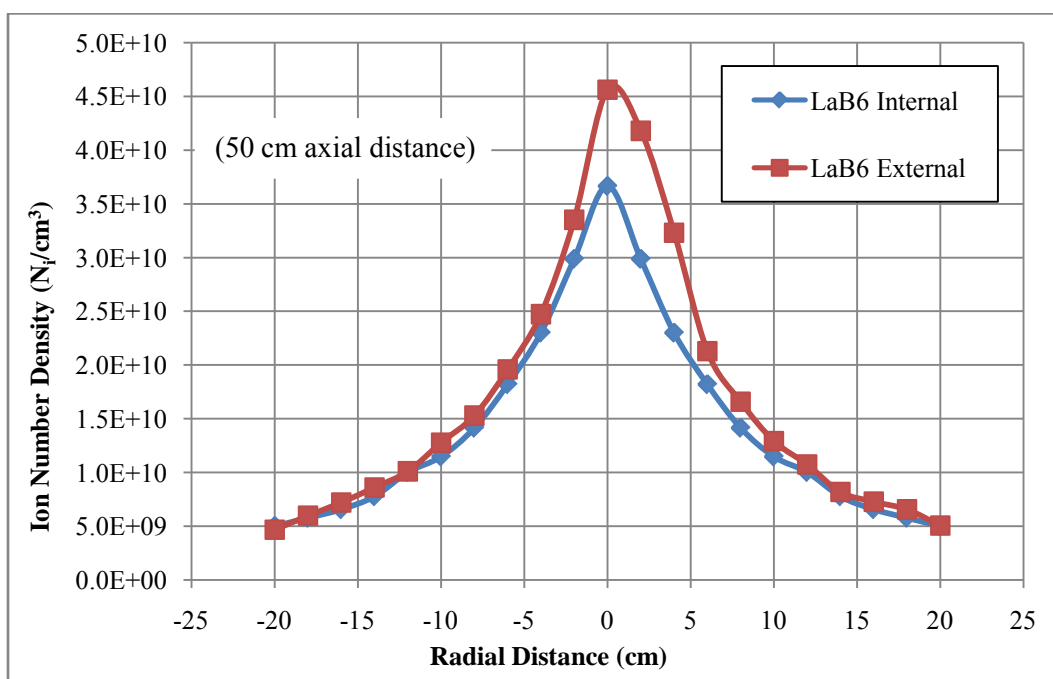


Figure 69. Ion Number Density with LaB₆ cathode at 50 cm Axial Distance

To better compare an internal versus an external cathode configuration with respect to the ion number density, a three-dimensional plot was generated for both CeB_6 test cases. Figure 70 and Figure 71 represent the ion number density profile for the externally-mounted CeB_6 and internally-mounted CeB_6 , respectively. Visual analysis of these plots shows that the peak ion number density is higher and the beam more focused for the internally-mounted case.

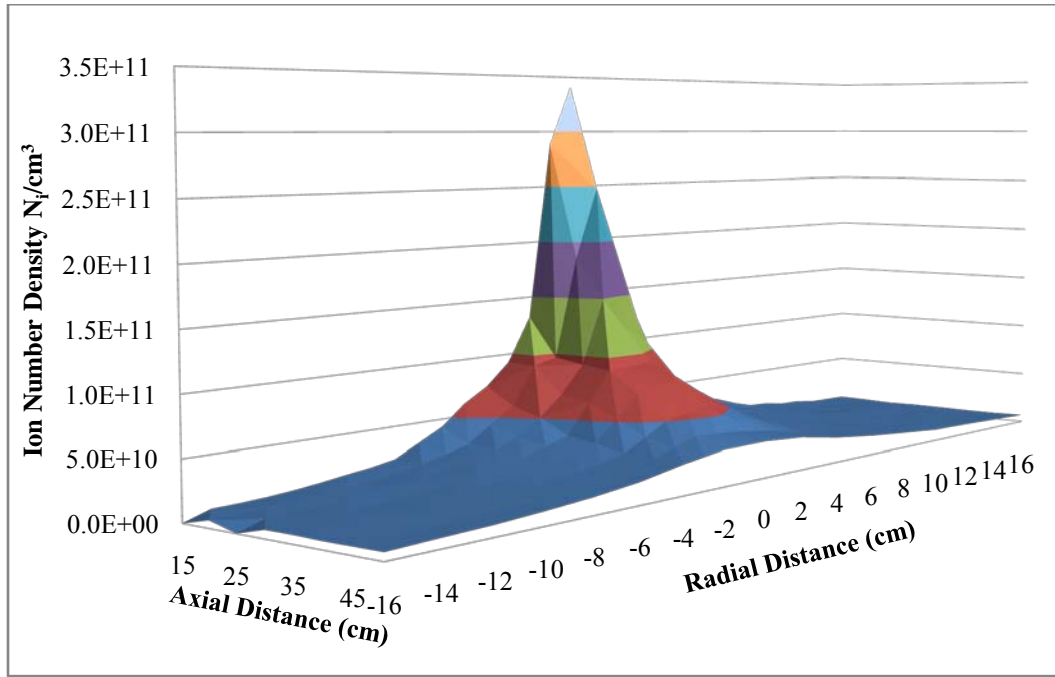


Figure 70. Ion Number Density Profile with Externally-Mounted CeB_6 cathode

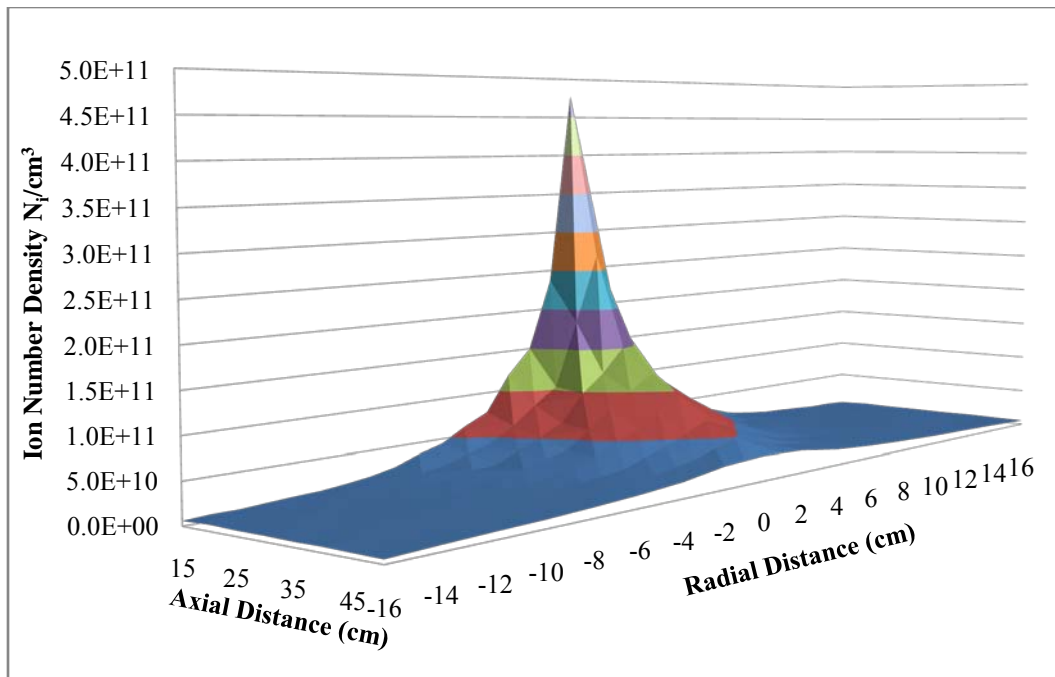


Figure 71. Ion Number Density Profile with Internally-Mounted CeB_6 cathode

ExB Probe Analysis

Data from the ExB probe was analyzed to determine the ionization species fractions and a velocity for each. Additionally, the potential difference between the ion creation point in the plasma and the collimator of the ExB probe was calculated. While data was taken at multiple locations within the plume for each test case, a comparison between the five test cases for only one location is presented. Much of the data taken for the internally-mounted cases was extremely noisy to the point of being unusable. Some of the data for the internally-mounted cases also exhibits an increasing or decreasing current bias over time that skewed the data. The likely cause of this is alignment errors with respect to the probe itself.

The data taken at 15 degrees off thruster centerline for the internally-mounted cathodes was resolved enough to be used for analysis. As such, the 15 degree off-axis

case was examined for all five test cases. For the externally-mounted cathodes, the data from both sides of the thruster, the cathode side and the opposite side, is evaluated. This gives a total of eight cases for the ExB probe data. In all cases the probe itself was pointed at the discharge channel, not the center of the thruster, and the distance to the thruster was 50 cm. Due to the small magnitude of the currents measured for the ExB data, the uncertainty for this data is ± 2.56 pA.

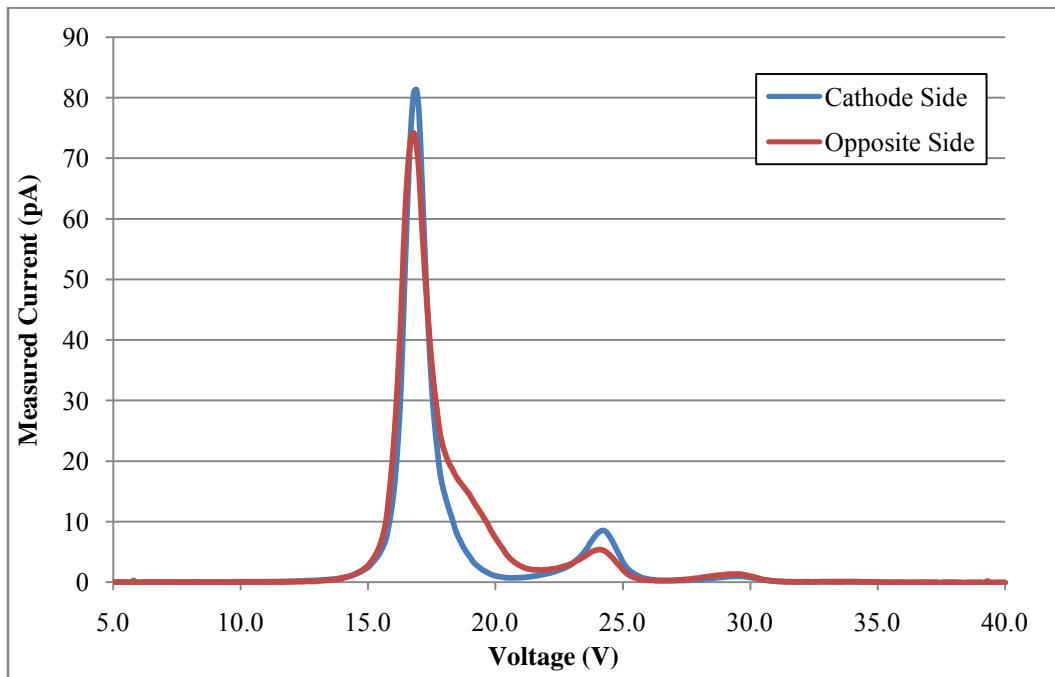


Figure 72. ExB Data for Externally-Mounted CeB₆

Figure 72 shows the ExB data from both the cathode side and opposite side channel locations for the externally-mounted CeB₆ cathode. The tallest peak indicates singly-ionized xenon, the second peak indicates doubly-ionized xenon, and the third peak, triply-ionized xenon. In some of the traces, quadruply-ionized xenon was detected, but its presence could not be seen in all tests since the magnitude of the collected current

barely exceeded the noise floor. As such, only singly-, doubly-, and triply-ionized xenon ions are considered in this analysis.

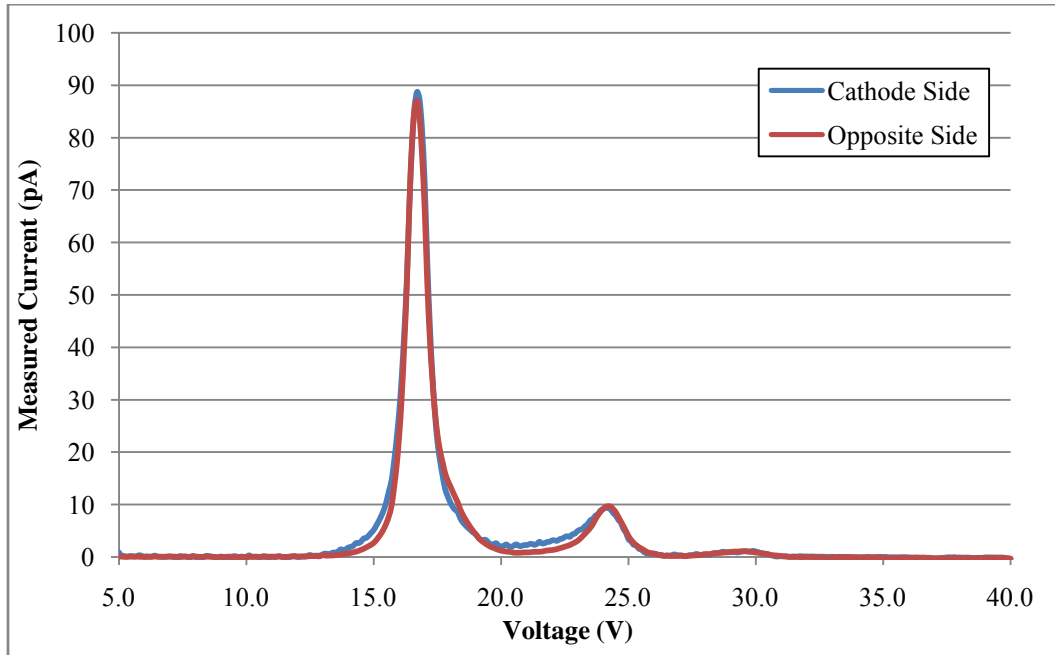


Figure 73. ExB Data for Externally-Mounted LaB₆

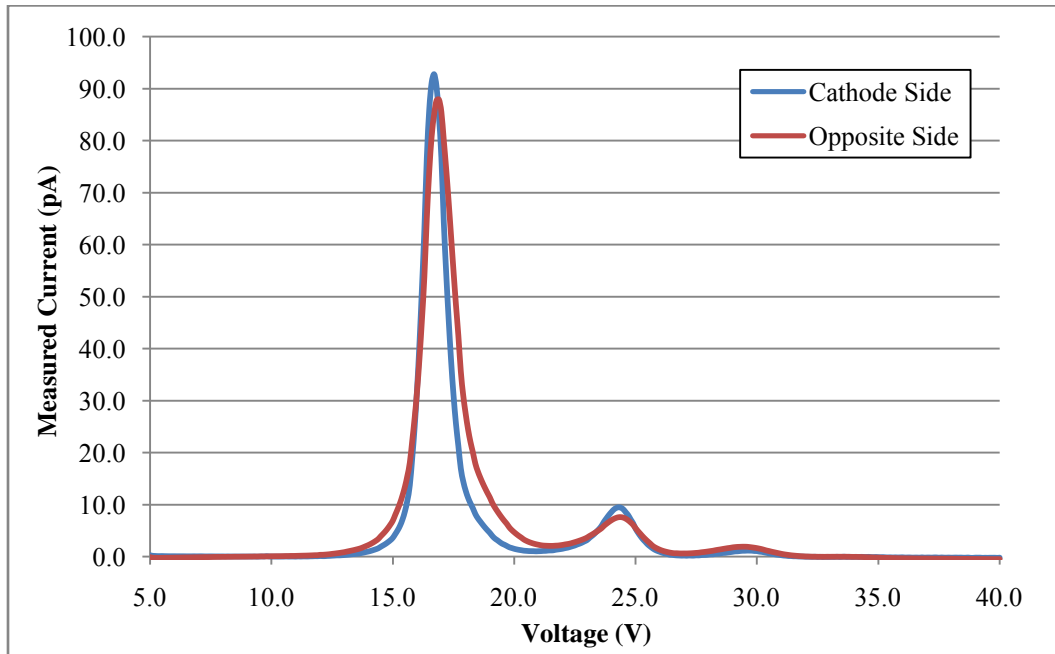


Figure 74. ExB Data for Externally-Mounted Tungsten

Figure 72 through Figure 74 compare the traces from the cathode side to the opposite side of the channel for the three externally-mounted cases. In all three cases the peak for both the singly- and doubly-ionized xenon is higher on the cathode side. Multiply-ionized particles are a loss mechanism since the ion carries multiple charges, but has the same mass as a singly-ionized particle. It would be better to singly-ionize more propellant, than to have multiply-ionized particles in the beam. The multiply-ionized particles, however, will have a higher velocity due to their higher charge state, for a given potential.

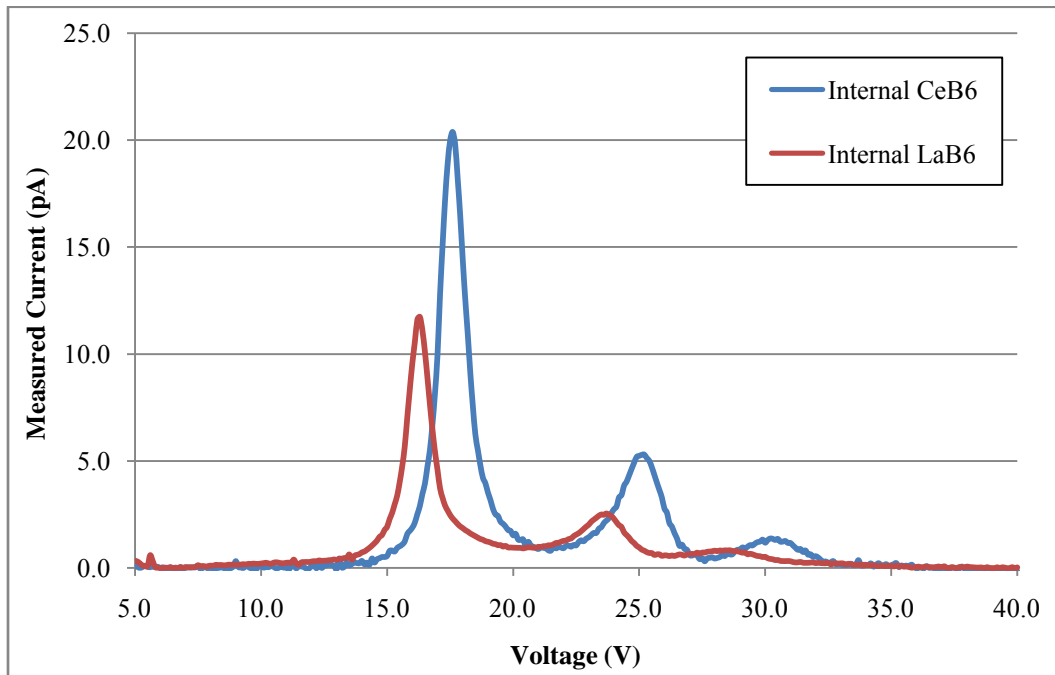


Figure 75. ExB Data for Internally-Mounted Cathodes

There is only a single trace for each of the internally-mounted cases. Figure 75 compares the measured current for internally-mounted CeB_6 and LaB_6 . The absolute magnitude of the peaks is less important than the relative difference between them, however the large difference in magnitude between the internally-mounted cases and the

externally-mounted cases may indicate a measurement or alignment issue. A comparison can be made between the internal and external cases by normalizing the measured current and plotting them on the same set of axes.

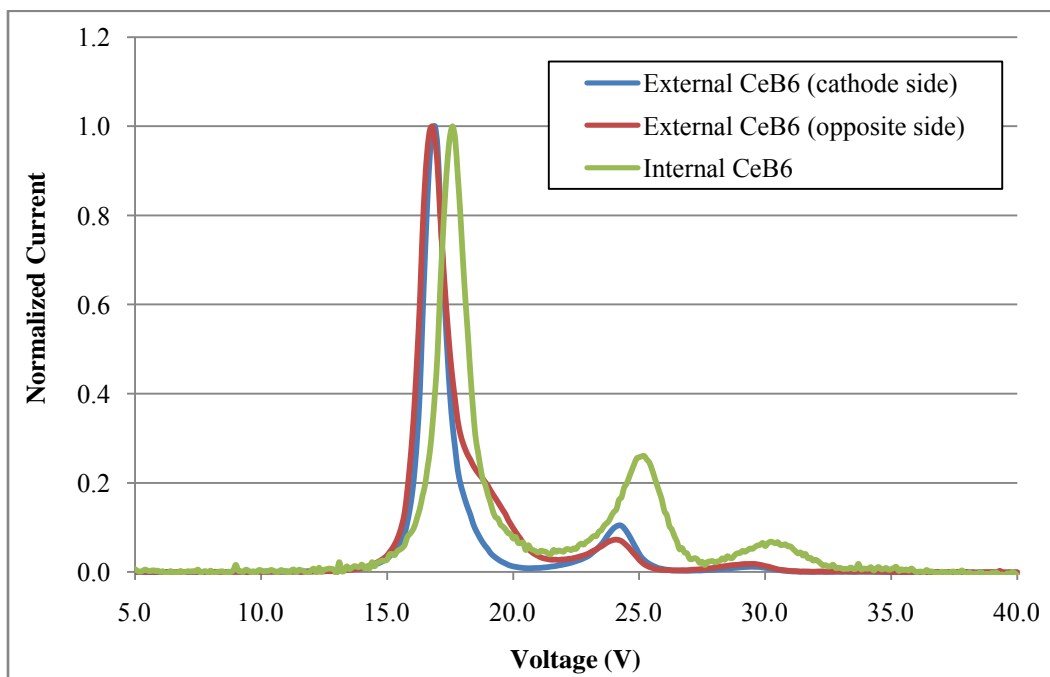


Figure 76. Normalized ExB Data for CeB₆

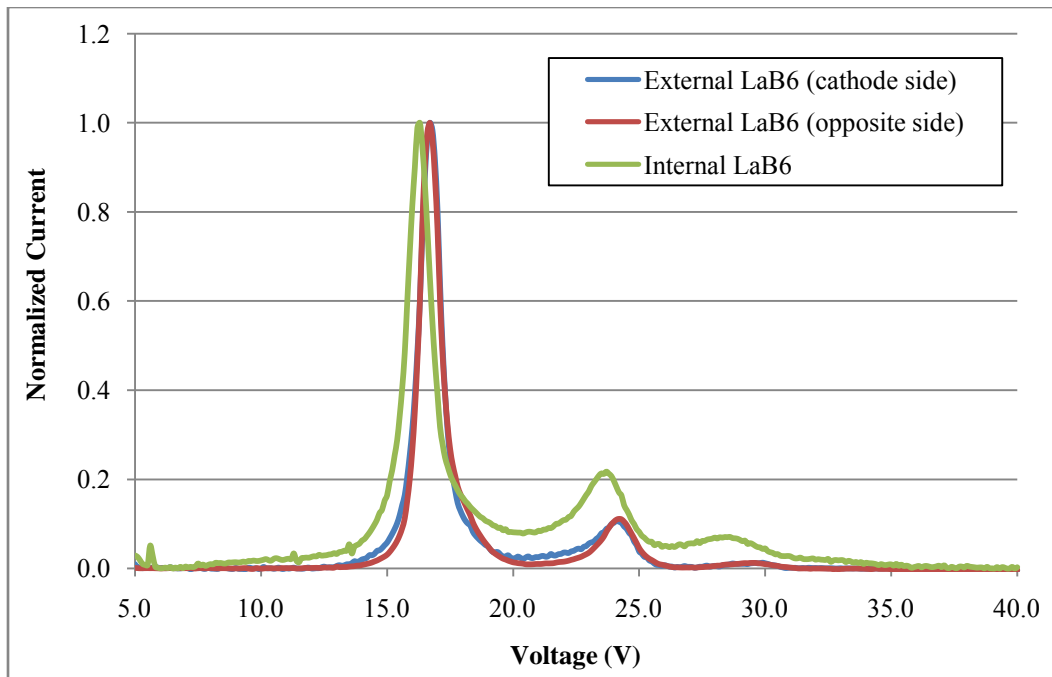


Figure 77. Normalized ExB Data for LaB₆

Figure 76 and Figure 77 show a very interesting trend. Both cases where internally-mounted cathodes were used show significantly higher concentrations of multiply-ionized xenon. This is the first data that would indicate reduced thruster performance with an internally-mounted cathode.

In order to determine the species fractions for the xenon ions, a FWHM analysis was performed on the data. Table 5 lists the percentages of each ionization level for the xenon propellant. The percent of multiply-ionized propellant for the internally-mounted cathode is considerably higher than for the external cases. These numbers overall are significantly different than the results obtained by Hofer, et al. when investigating performance differences based on cathode geometry. [10] Their results did show a slight increase in multiply-ionized propellant with an internally-mounted cathode, but it was only 2%. Their research, however, involved a high-power Hall thruster, 8 kW class, so

there may be variability since the operating conditions were significantly different from those in this work. Additionally, only one location in the plume was analyzed to determine ionization species fractions. In Hofer's work the ExB data was taken on centerline. Ekholm, et al., using a Busek BHT-600 W Hall thruster, showed relatively constant ion species fractions through a range of angles, but Pollard, et al. showed the fraction of multiply-charged ions to be higher, ~20% for xe^{+2} , at angles of 30 degrees and higher off axis. [55] [58] Pollard's work also utilized a high-power, 4 kW class, Hall thruster.

Table 5. Ion Species Fractions

Insert Material	Measurement Location	Ion Species Fraction		
		xe^{+}	xe^{+2}	xe^{+3}
CeB ₆ (edge-mount)	cathode side	0.812	0.150	0.038
	opposite side	0.782	0.189	0.028
LaB ₆ (edge-mount)	cathode side	0.806	0.158	0.036
	opposite side	0.820	0.143	0.037
Impreg. W (edge-mount)	cathode side	0.828	0.133	0.040
	opposite side	0.804	0.157	0.039
CeB ₆ (center-mount)	(n/a)	0.587	0.233	0.180
LaB ₆ (center-mount)	(n/a)	0.669	0.213	0.118

Taking the voltage from the ExB data where the maximum current was measured for each species of ion, we can calculate a better value for the velocity of the ions and take into account the velocity variability due to charge state. The velocity is given by;

$$v = \frac{\Delta\phi}{B \cdot d} \quad (23)$$

where $\Delta\phi$ is the voltage at which the current peaks, and B and d are properties of the ExB probe itself. Using equation (20) the potential between the location where the ion was created and the collimator of the ExB probe can be determined as well.

Table 6. Ion Velocity (km/s) for Externally-Mounted Cathodes

	Cathode Insert Material and Channel Side					
	CeB ₆ (cathode)	CeB ₆ (opposite)	LaB ₆ (cathode)	LaB ₆ (opposite)	Impreg. W (cathode)	Impreg. W (opposite)
Singly-ionized (xe ⁺)	20.7	20.6	20.5	20.5	20.5	20.7
Doubly-ionized (xe ⁺²)	29.7	29.5	29.5	29.7	29.8	29.9
Triply-ionized (xe ⁺³)	36.2	36.2	36.6	36.3	36.3	36.0

Table 7. Ion Velocity (km/s) for Internally-Mounted Cathodes

	Cathode Insert Material	
	CeB ₆	LaB ₆
Singly-ionized (xe ⁺)	21.6	20.0
Doubly-ionized (xe ⁺²)	30.9	29.0
Triply-ionized (xe ⁺³)	37.0	35.4

Looking at the velocities calculated in Table 6 and Table 7, the values are all reasonably consistent for each test case. The internally-mounted CeB₆ case again shows the highest performance with respect to the velocity of singly-ionized xenon particles and the internally-mounted LaB₆ shows the lowest performance.

V. Conclusions and Recommendations

Conclusions of Research

There are a number of ways to look at the data presented and beyond that, the performance of a given thruster. Beyond improving efficiency, which is always a driver for innovation, performance can be looked at in several ways for a thruster. Both thrust and specific impulse (I_{sp}) can be used to classify the performance of a thruster. With EP a choice generally needs to be made between these two performance metrics. High thrust can provide a large ΔV in a shorter period of time, whereas a high I_{sp} will yield a greater economy for the available propellant. Many of the EP thrusters being developed today are designed to be dual-mode thrusters than can operate either at a high thrust setting or a high I_{sp} setting depending on the mission requirements.

Table 8 summarizes the results of this work. Based on the numbers, it appears as though the externally-mounted boride-based cathodes provided both the highest thrust and highest I_{sp} . An explanation of these results follows.

Table 8. Efficiency and Performance Results

	Cathode Insert Material and Geometry				
	CeB ₆ (edge-mount)	LaB ₆ (edge-mount)	Impreg. W (edge-mount)	CeB ₆ (center-mount)	LaB ₆ (center-mount)
Electrical Eff. (η_o)	0.950	0.938	0.973	0.967	0.951
Mass Utilization Eff. (η_m)	0.882	0.900	0.841	0.889	0.879
Alpha Correction (α)	0.937	0.936	0.941	0.842	0.879
Gamma Correction (γ)	0.928	0.925	0.934	0.834	0.865
Beam Current Eff. (η_b)	0.784	0.807	0.747	0.791	0.789
Beam Voltage Eff. (η_v)	0.896	0.866	0.915	0.910	0.892
Total Efficiency (η_T)	0.507	0.505	0.488	0.431	0.440
I_{sp} (seconds)	1659	1660	1608	1515	1537
Thrust (mN)	44.79	44.80	43.40	40.89	41.50

The electrical utilization efficiencies have been carried over from the power consumption calculations without any adjustments. Both the mass utilization efficiency and beam current efficiency require a value for the beam current in order to be determined. Since the entire beam current was not quantified in this work, these values can only be used to make comparisons between the five cases presented here. The integrated beam current used for the calculations was the beam current measured at 60 cm as that was the midpoint of the Faraday data. The mass utilization efficiency was calculated using;

$$\eta_m = \frac{I_b}{e} \frac{M}{\dot{m}_p} \quad (24)$$

where M is the mass of the xenon ions and \dot{m}_p is the total mass flow rate of the propellant. The beam voltage efficiency was taken directly from the Langmuir data.

To determine the value for α , the correction factor for multiply-charged ions, equation (14) was expanded to include triply-ionized xenon. The significantly higher fractions of multiply-ionized propellant measured for the internally-mounted cathodes were the most significant efficiency loss observed relative to the externally-mounted cathodes. Again, the value for α was calculated from ExB data take at one location in the plume and it may vary significantly depending on the location where the data was taken. To determine the value for γ , the angle calculated from the Faraday data using the FWHM method was used. This is not the true thrust half-angle for the thruster, but the relative comparisons between the five cases are still valid.

The total efficiencies were calculated using equation (7) and average just under 50%, which is typical for Hall thrusters in this class. The I_{sp} values were calculated as follows;

$$I_{sp} = \frac{\gamma \eta_m}{g} \sqrt{\frac{2eV_b}{M}}. \quad (25)$$

The I_{sp} values calculated have a degree of error due to the assumptions made above, but, again, are valid for comparisons between the five cases. It is interesting to note that the boride-based cathodes have similar I_{sp} values for each of their respective geometries.

Finally, the thrust was calculated using the following equation;

$$T = \gamma \sqrt{\frac{2M}{e}} I_b \sqrt{V_b} \quad (26)$$

which is subject to the previously stated assumptions as well. These numbers provide a good basis for comparison as well. Mirroring the trend for I_{sp} , the boride-based cathodes showed similar performance based on geometry.

The most surprising result was the internally-mounted CeB_6 cathode having both the lowest I_{sp} and the lowest thrust. The author also expected the impregnated tungsten's performance to exceed that of the externally-mounted boride-based cathodes. The loss mechanism of multiply-ionized propellant significantly impacted the performance of the internally-mounted cathodes. The γ term, which is used to determine the values of thrust and I_{sp} , is squared in the total efficiency equation and is significantly lower for the internally-mounted cathodes. For the internally-mounted LaB_6 cathode both the increased multiply-ionized propellant fractions and the larger thrust angle contributed to the reduction in the value of γ , however, for the internally-mounted CeB_6 it was solely the

increase in the fractions of the multiply-ionized propellant that resulted in the efficiency loss. If the multiply-ionized propellant losses from the ExB data are neglected the efficiency of the internally-mounted CeB₆ exceeds all the other cases by approximately 3%. Neglecting the ExB data for the remaining cases, the LaB₆ cathodes in both geometries demonstrate the next highest efficiencies, followed by the externally-mounted CeB₆ and then the tungsten.

Recommendations for Future Research

The possible avenues available to further the research begun here are quite varied. The place to begin would be to expand the operating envelope of the thruster from one operating condition to a range of operating conditions. Since the BHT-1500-C used in this work was operated at less than its rated power, the performance measured is likely sub-optimal. In order to operate the thruster throughout its full range, modifications will need to be made to the SPASS lab. More pumping capacity to handle the higher propellant flow rates and larger power supplies to deliver the increased discharge power will be required. Work is currently in progress to add additional cryo-pumps to the existing vacuum chamber that may allow higher propellant flow rates without exceeding $\sim 1 \times 10^{-5}$ torr.

The discharge power is not the only operating parameter that can be varied. The magnet power and keeper power can also be varied to see what effect they have on performance. Better measurements of the input power would allow for a more precise determination of the electrical utilization efficiency. As the operating condition is varied, the performance and efficiency will likewise change. The instruments used in this study can again be utilized to obtain data on the plume. To get ground-truth numbers for thrust,

however, a thrust stand would need to be used. The SPASS lab has a thrust stand that should be used to determine the thrust for the BHT-1500-C for both the operating condition used in this work and for a range of additional operating conditions up to the limit of the vacuum chamber.

The data taken in this work has provided some insight into the effect of cathode insert material and geometry on thruster performance and efficiency, but higher fidelity data is needed to provide a basis for comparison outside of this work. A true measure of beam current and better ion species fraction data would be the place to start. Knowing the true total beam current would allow comparison against other Hall thrusters in this class and a better determination of mass utilization efficiency and beam current efficiency. The ExB data for the internally-mounted cathodes is somewhat suspect and a more robust set of data may yield different results.

Finally, the cathodes themselves can be tested. Varying the keeper power and flow to the cathodes would allow for the identification of the optimal operating condition for the cathodes. Varying the cathode position beyond the two tested in this work would be possible as well, as in the work done by McDonald and Gallimore. [40] Thermal analysis of both the cathode and the thruster itself could help identify possible loss mechanisms of each. If time and lab requirements allow, an extended lifetime test should be conducted on the thruster and cathode combination using a boride-based cathode to determine the consumption rate of the cathode and any wear effects on the thruster or cathode. Finally, other cathode designs can be tested with the thruster in an effort to achieve maximum performance or efficiency.

Appendix A. Thruster Operating Procedures

The following procedures were used for the operation of the BHT-1500-C Hall thruster and the cathode being tested with it.

1. Ensure vacuum chamber pressure is below 1×10^{-6} torr.
2. Purge xenon propellant lines;
 - a. Ensure xenon gas bottle valve is closed.
 - b. Turn on MKS four-channel readout.
 - c. Open flow controllers to anode and cathode.
 - d. Open propellant regulator valve.
 - e. Once flow rate drops below 1 sccm, close all valves/secure flow controllers.
3. Condition Cathode
 - a. Turn on heater power supply and set maximum voltage to 13 V.
 - b. Set current to 2.5 A for 15 minutes. (40 minutes for tungsten)
 - c. Increase current by 2.5 A every 15 minutes until at 10 A. (40 minutes for tungsten)
 - d. Once at 10 A for 15 minutes, increase current to 11.25 A and allow voltage to stabilize.
4. Prepare Propellant Lines
 - a. Open xenon bottle valve.
 - b. Set propellant regulator valve to 20 psi.
 - c. Open mass flow controller to cathode with 3 sccm flow rate set.

5. Light Cathode

- a. Turn on power to the keeper power supply.
- b. Ensure output is set to 1.0 A and 650 V.
- c. Depress “output” button to apply the potential to the keeper.
- d. Cathode ignition is indicated by a drop in keeper voltage.

6. Light Thruster

- a. Turn on power supply for PPU.
- b. Turn on PPU.
- c. Launch BPU-600 Host Simulator software.
- d. Set discharge voltage to 300 V.
- e. Open mass flow controller to anode with 25 sccm flow rate set.
- f. Activate discharge power from Host Simulator. (A purple glow discharge will be seen on the face of the thruster.)

7. Collimate Plume

- a. Turn on power to magnet power supply or set 2.07 A for magnet power in the Host Simulator software and activate it.
- b. Set maximum voltage to 6.5 V on power supply.
- c. Slowly increase current to 2.07 A on power supply and observe plume. (A highly collimated plume of blue plasma will now emanate from the face of the thruster.)

8. Secure Heater: turn off the heater power supply.

9. Allow thruster to stabilize and conduct testing. Ensure chamber pressure remains below $\sim 1 \times 10^{-5}$ torr.

10. Securing Thruster

- a. Secure power to the anode, magnets, and keeper.
- b. Secure xenon flow to the anode and cathode.
- c. Close xenon bottle valve and regulator.
- d. Close Host Simulator software and secure power to the PPU.
- e. Turn off all power supplies.

11. If bringing the vacuum chamber back to atmospheric pressure, ensure nitrogen is used to back-fill the chamber to help mitigate any chance of insert poisoning.

Appendix B. Faraday Probe Data

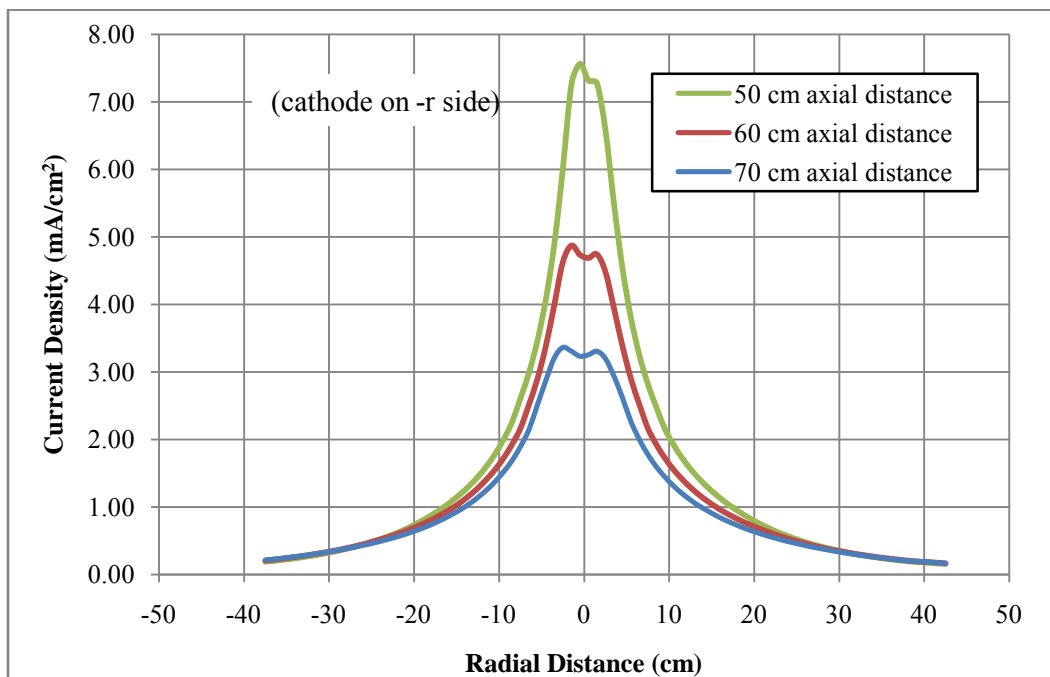


Figure 78. Current Density for Externally-Mounted CeB_6

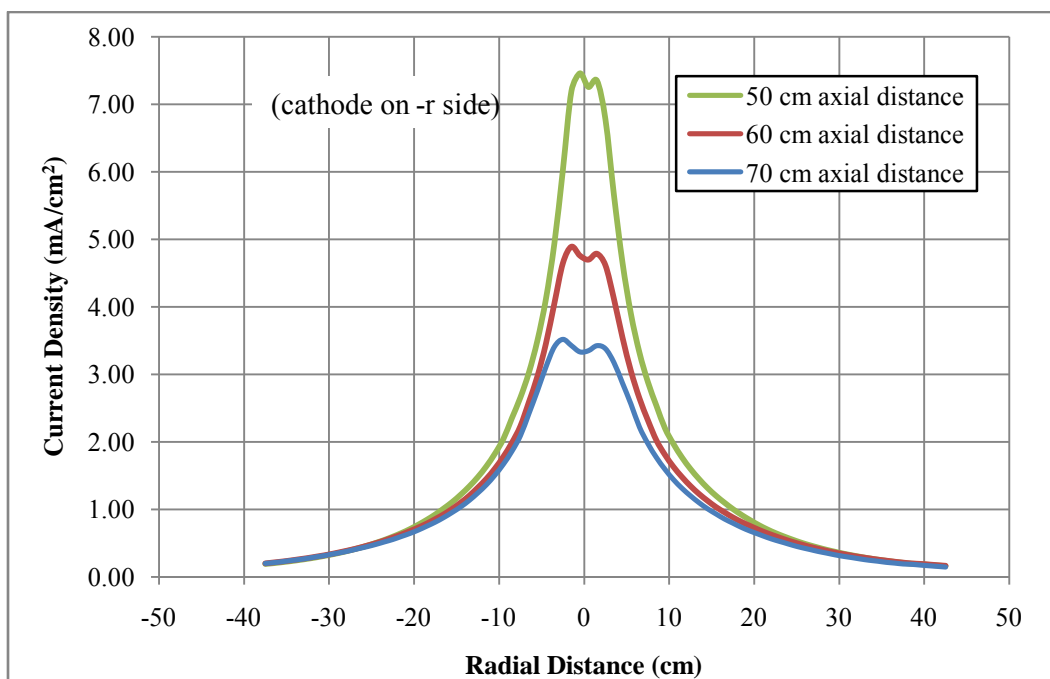


Figure 79. Current Density for Externally-Mounted LaB_6

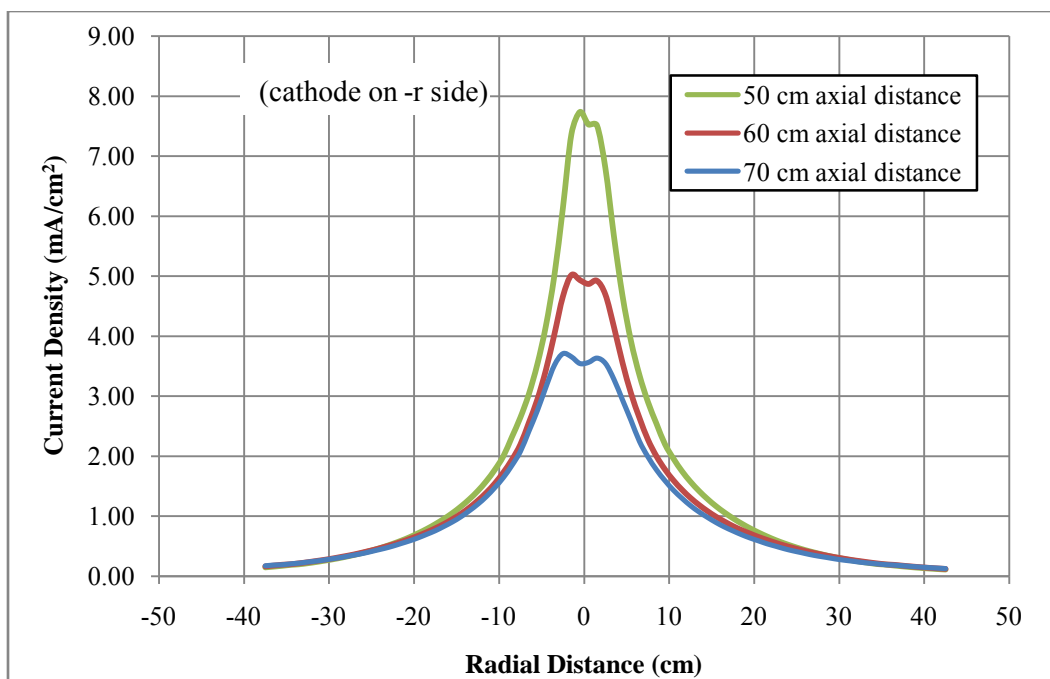


Figure 80. Current Density for Externally-Mounted Tungsten

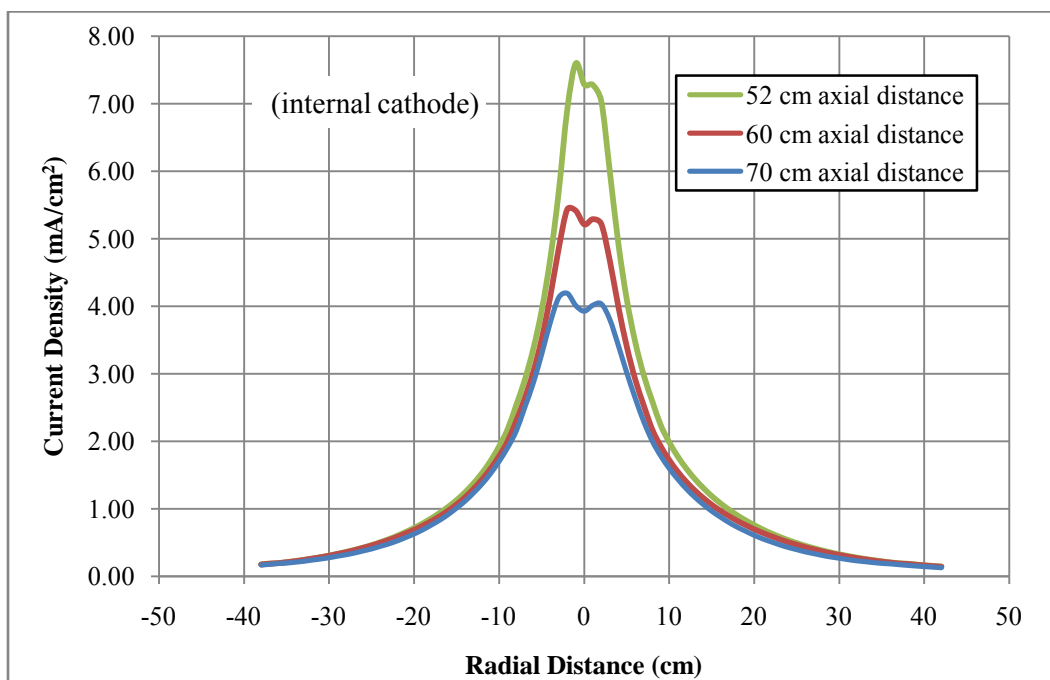


Figure 81. Current Density for Internally-Mounted CeB₆

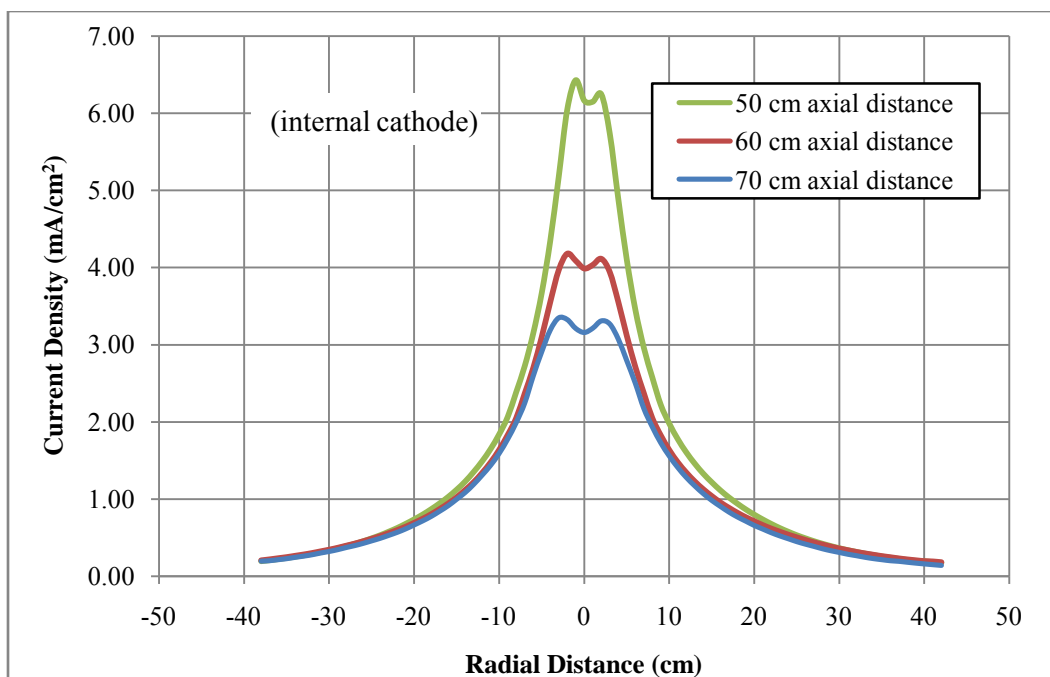


Figure 82. Current Density for Internally-Mounted LaB₆

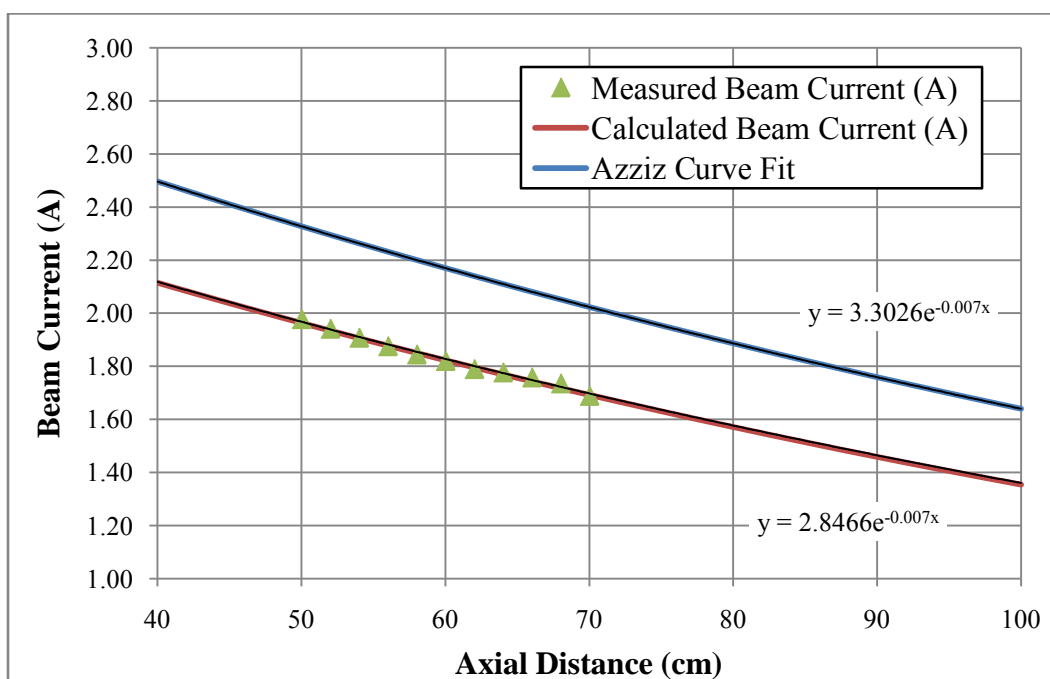


Figure 83. Total Beam Current vs. Axial Distance for Externally-Mounted LaB₆

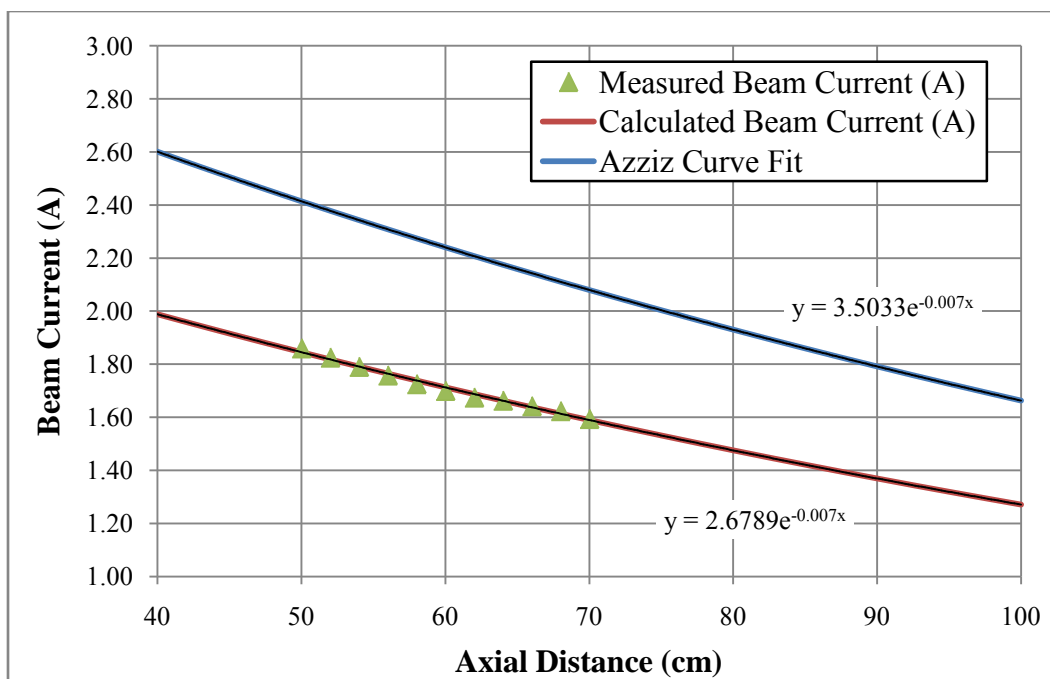


Figure 84. Total Beam Current vs. Axial Distance for Externally-Mounted Tungsten

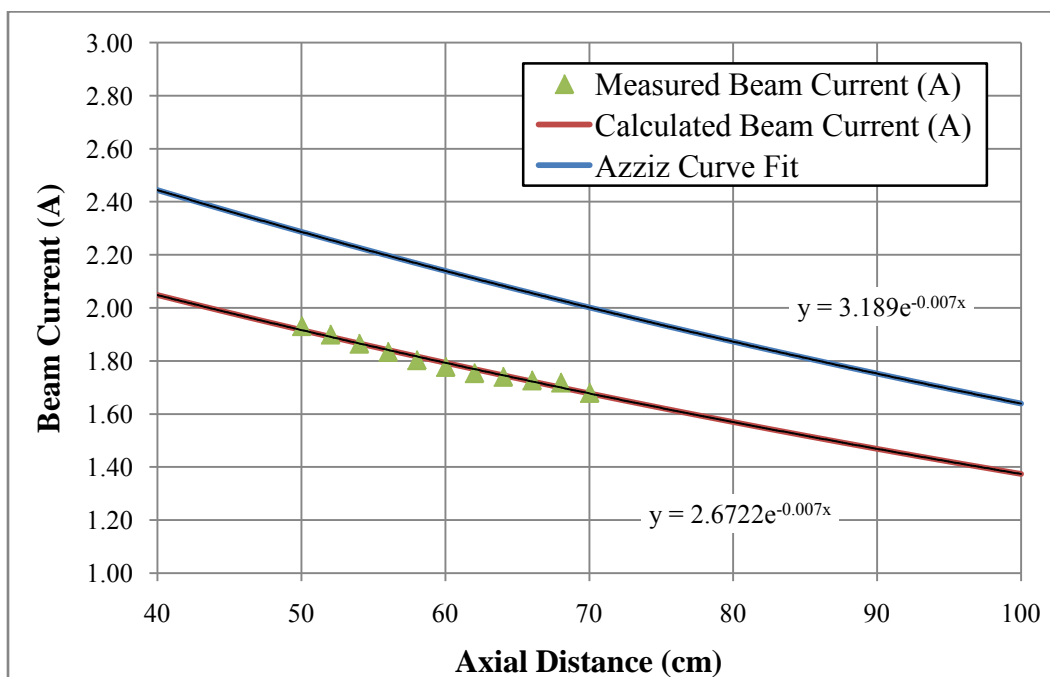


Figure 85. Total Beam Current vs. Axial Distance for Internally-Mounted LaB₆

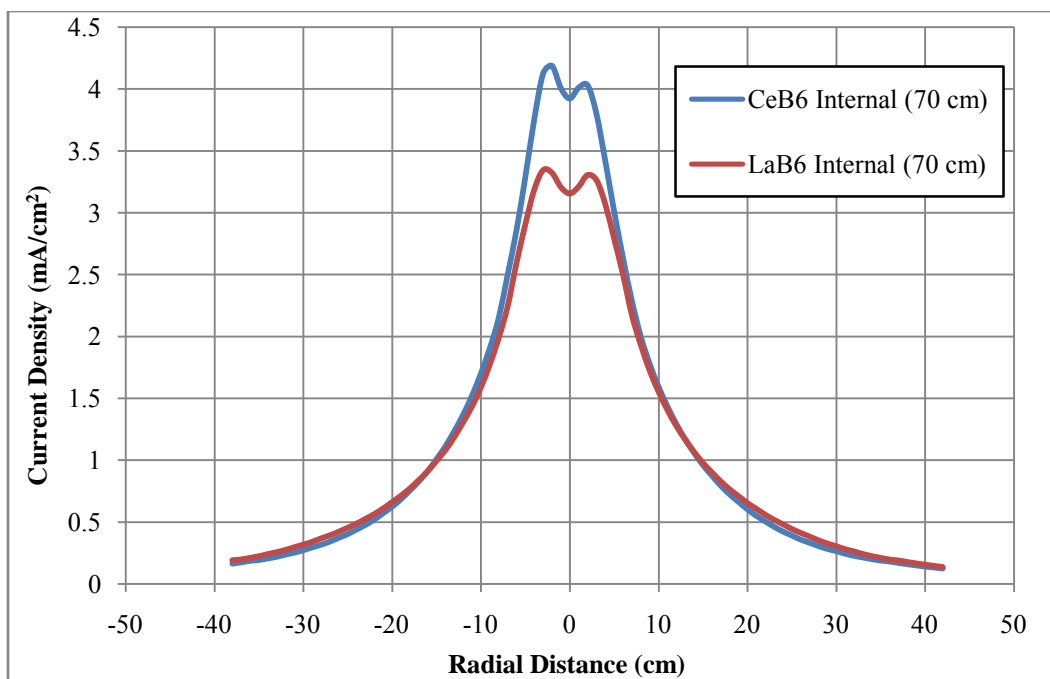


Figure 86. Current Density with Internally-Mounted Cathodes at 70 cm Axial Distance

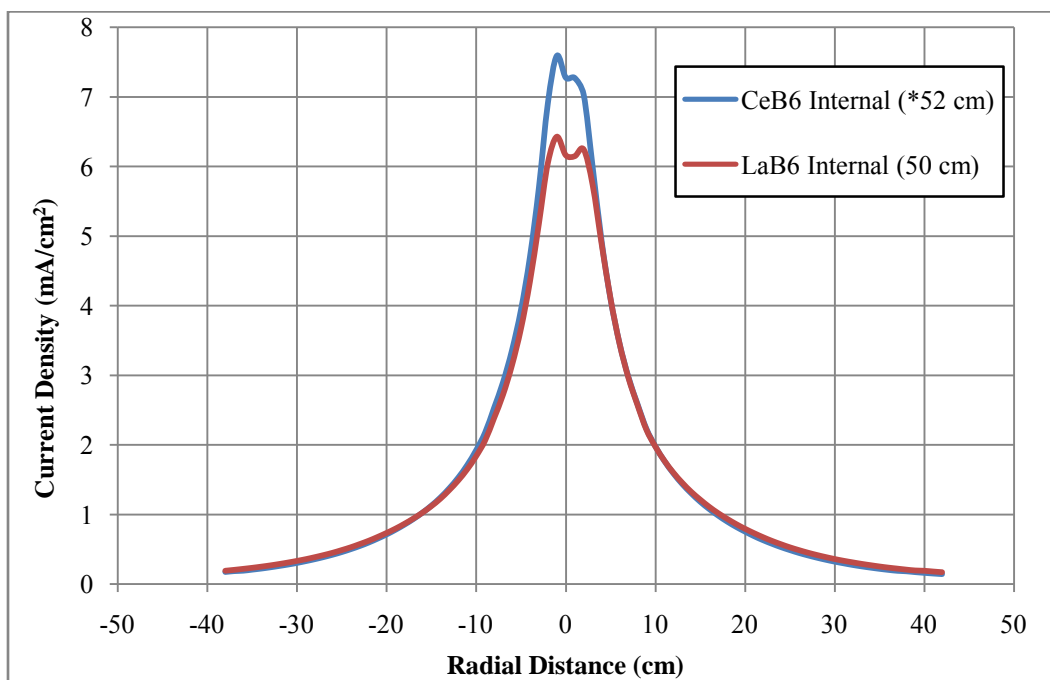


Figure 87. Current Density with Internally-Mounted Cathodes at 50 cm Axial Distance

Appendix C. Langmuir Probe Data

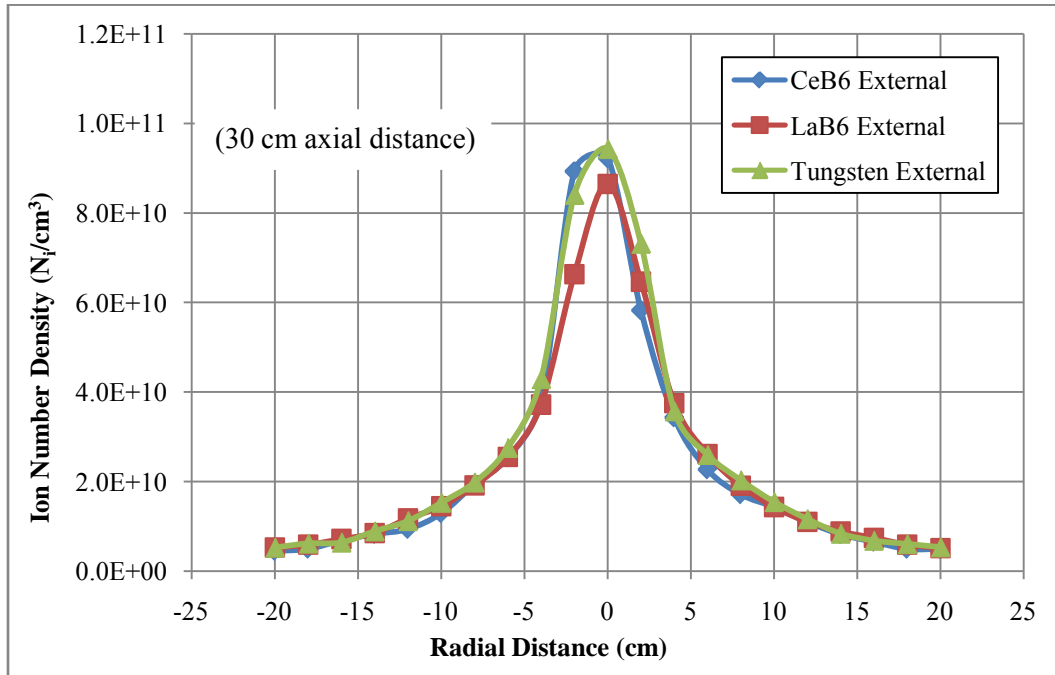


Figure 88. Ion Number Density with Externally-Mounted Cathodes at 30 cm Axial Distance

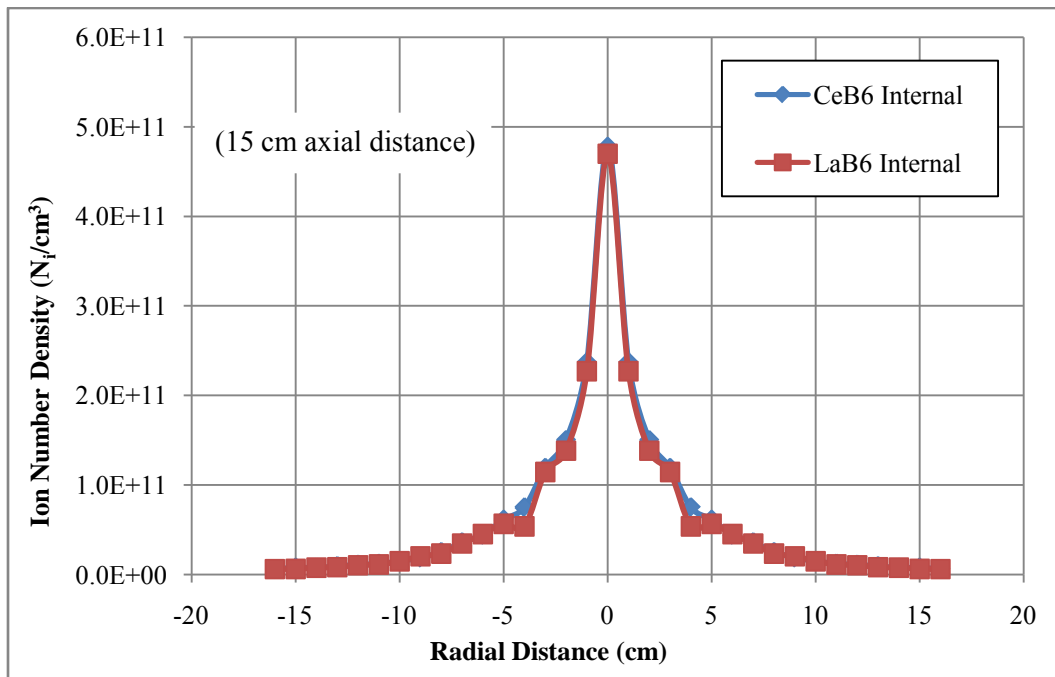


Figure 89. Ion Number Density with Internally-Mounted Cathodes at 15 cm Axial Distance

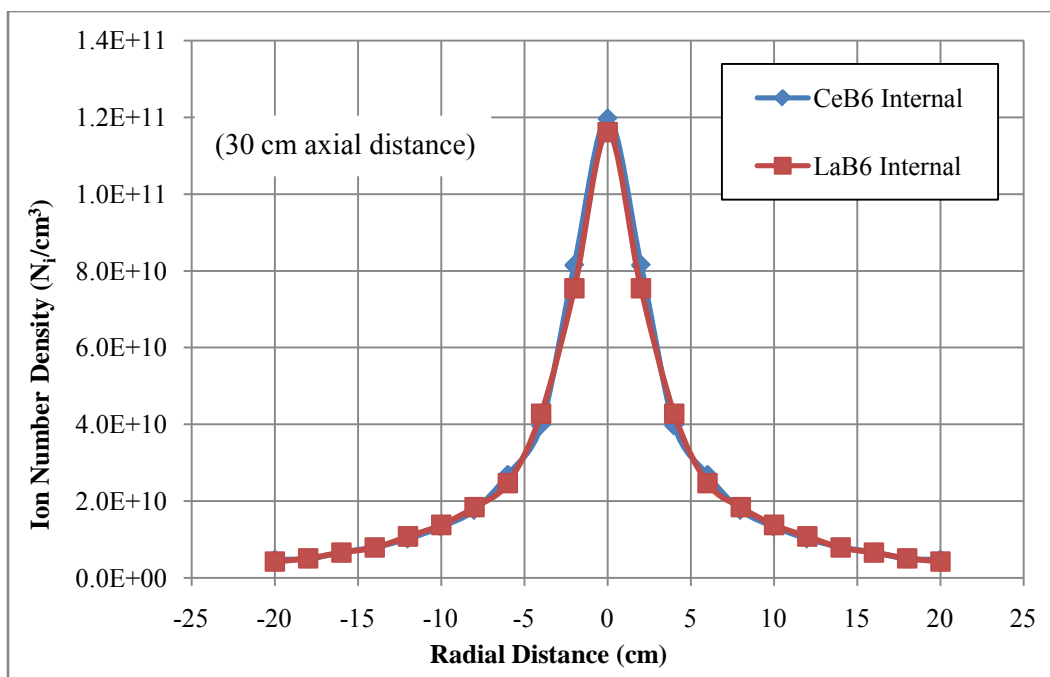


Figure 90. Ion Number Density with Internally-Mounted Cathodes at 30 cm Axial Distance

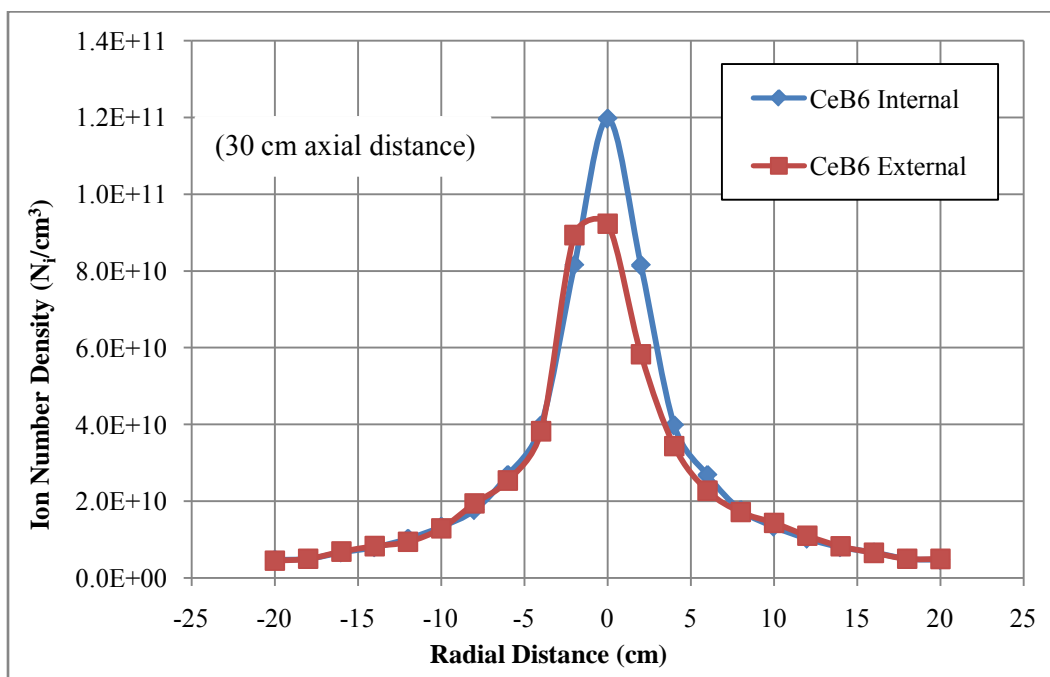


Figure 91. Ion Number Density with CeB₆ cathode at 30 cm Axial Distance

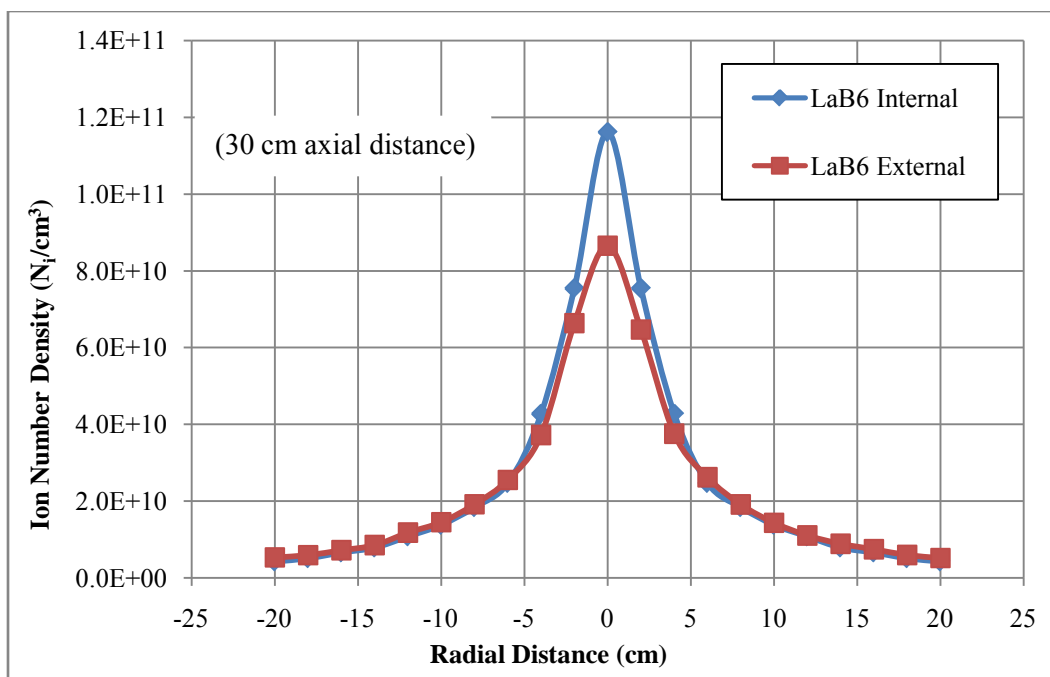


Figure 92. Ion Number Density with LaB₆ cathode at 30 cm Axial Distance

Appendix D. ExB Probe Data

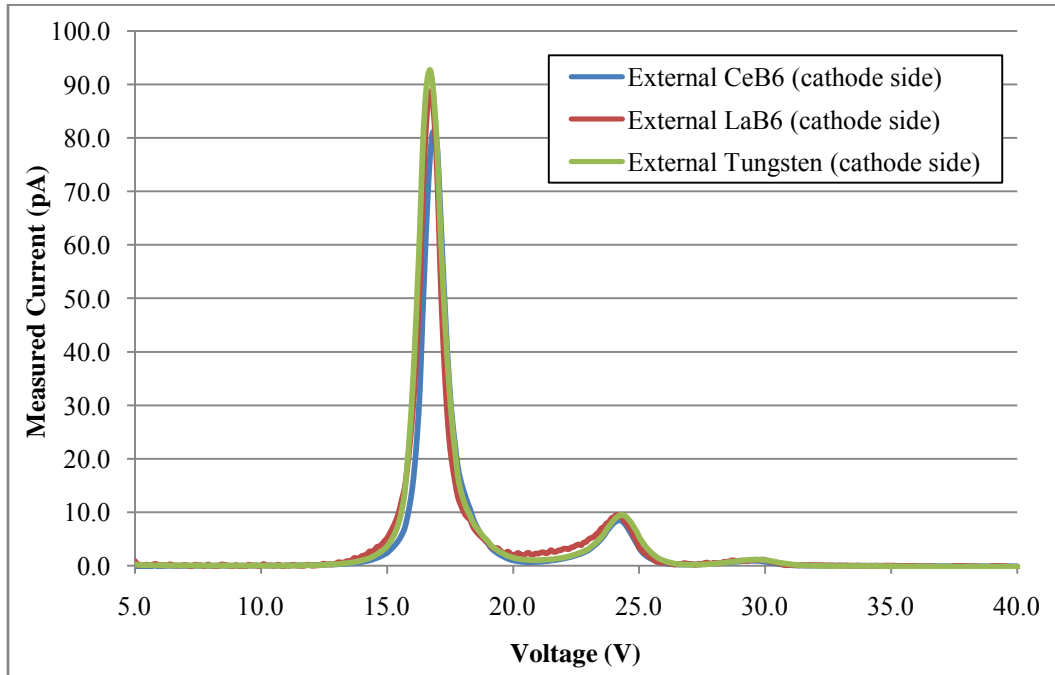


Figure 93. Cathode Side ExB Data for Externally-Mounted Cases

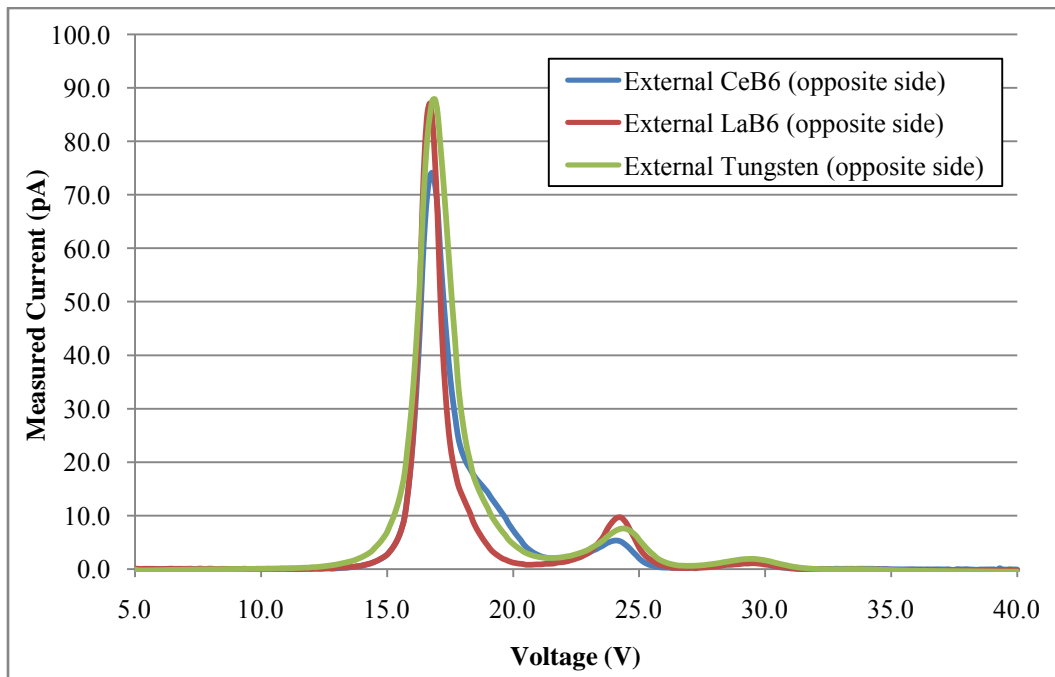


Figure 94. Opposite Side ExB Data for Externally-Mounted Cases

Table 9. Ion Generation Potential (V) for Externally-Mounted Cathodes

	Cathode Insert Material and Channel Side					
	CeB ₆ (cathode)	CeB ₆ (opposite)	LaB ₆ (cathode)	LaB ₆ (opposite)	Impreg. W (cathode)	Impreg. W (opposite)
Singly-ionized (xe ⁺)	291.8	288.4	285.0	285.0	285.0	291.8
Doubly-ionized (xe ⁺²)	299.2	296.7	296.7	299.2	301.7	304.2
Triply-ionized (xe ⁺³)	296.4	296.4	304.5	298.4	298.4	294.4

Table 10. Ion Generation Potential (V) for Internally-Mounted Cathodes

	Cathode Insert Material	
	CeB ₆	LaB ₆
Singly-ionized (xe ⁺)	316.5	271.5
Doubly-ionized (xe ⁺²)	324.4	287.0
Triply-ionized (xe ⁺³)	310.6	284.5

Bibliography

- [1] M. Blair and D. DeGeorge, "Overview of the Integrated High Payoff Rocket Propulsion Technology (IHPRT) Program," in *51st International Astronautical Congress*, Rio de Janeiro, 2000, pp. 1-10.
- [2] John R. Brophy, James Sovey, Tom Bond, Mike Matranga, and Duff Bushway, "Ion Propulsion System (NSTAR) DS1 Technology Validation Report," NASA Jet Propulsion Laboratory, Pasadena, n.d.
- [3] National Aeronautics and Space Administration. (2008, April) NASA-DAWN. [Online]. http://dawn.jpl.nasa.gov/mission/dawn_fact_sheet.pdf
- [4] NASA Glenn Research Center. (2007, March) GRC - NSTAR Ion Thruster. [Online]. <http://www.grc.nasa.gov/WWW/ion/past/90s/nstar.htm>
- [5] Dan M. Goebel and Ira Katz, *Fundamentals of Electric Propulsion: Ion and Hall Thrusters*. Pasadena, CA: Jet Propulsion Laboratory, 2008.
- [6] Busek Space Propulsion. (2007, January) Busek Co. Inc. [Online]. <http://www.busek.com/releases/2007-01-BusekPR.pdf>
- [7] Astronautix.com. (n.d.) SPT-100 Hall. [Online]. <http://www.astronautix.com/engines/spt0hall.htm>
- [8] Dan M. Goebel, Ron M. Watkins, and Kristina K. Jameson, "LaB6 Hollow Cathodes for Ion and Hall Thrusters," *Journal of Propulsion and Power*, vol. 23, no. 3, pp. 552-558, June 2007.
- [9] Dustin J. Warner, "Advanced Cathodes for Next Generation Electric Propulsion Technology," Air Force Institute of Technology, Dayton, Thesis AFIT/GA/ENY/08-M07, 2008.
- [10] Richard R. Hofer, Lee K. Johnson, Dan M. Goebel, and Dennis J. Fitzgerald, "Effects of an Internally-Mounted Cathode on Hall Thruster Plume Properties," in *42nd AIAA/ASME/SAE/ASEE Joint Propulsion Conference and Exhibit*, Sacramento, 2006, pp. 1-23.

- [11] M. Martinez-Sanchez and J. E. Pollard, "Spacecraft Electric Propulsion - AN Overview," *Journal of Propulsion and Power*, vol. 14, no. 5, pp. 688-699, September-October 1998.
- [12] Busek Co. Inc. (2006) Busek Co. Inc. - Hall Effect Thrusters. [Online].
<http://www.busek.com/halleffect.html>
- [13] Ronald W. Humble, Gary N. Henry, and Wiley J. Larson, Eds., *Space Propulsion Analysis and Design*, 1st ed. New York, NY: McGraw Hill, 1995.
- [14] Wiley J. Larson and James R. Wertz, Eds., *Space Mission Analysis and Design*, 3rd ed. New York, NY: Springer, 1999.
- [15] R. L. Sackheim and D.C. Byers, "Status and Issues Related to In-Space Propulsion Systems," *Journal of Propulsion and Power*, vol. 14, no. 5, pp. 669-675, September-October 1998.
- [16] Robert S. Jankovsky, David H. Manzella, and Richard R. Hofer, "NASA's Hall Thruster Program," in *37th AIAA Joint Propulsion Conference*, Salt Lake City, 2001, pp. 1-14.
- [17] John R. Brophy, "NASA's Deep Space 1 ion engine," *Review of Scientific Instruments*, vol. 73, no. 2, pp. 1071-1078, February 2002.
- [18] John R. Brophy et al., "The Ion Propulsion System for Dawn," in *39th AIAA/ASME/SAE/ASEE Joint Propulsion Conference and Exhibit*, Huntsville, 2003, pp. 1-8.
- [19] Christopher R. Koppel and Denis Estublier, "The SMART-1 Hall Effect Thruster Around the Moon: In Flight Experience," in *The 29th International Electric Propulsion Conference*, Princeton, 2005, pp. 1-9.
- [20] David Manzella, David Oh, and Randall Aadland, "Hall Thruster Technology for NASA Science Missions," in *41st Joint Propulsion Conference and Exhibit*, Tuscon, 2005, pp. 1-13.

- [21] Kevin E. Witzberger and David Manzella, "Performance of Solar Electric Powered Deep Space Missions Using Hall Thruster Propulsion," in *41st AIAA/ASME/SAE/ASEE Joint Propulsion Conference and Exhibit*, Tuscon, 2005, pp. 1-21.
- [22] John R. Brophy and David H. Rodgers, "Ion Propulsion for a Mars Sample Return Mission," in *36th AIAA/ASME/SAE/ASEE Joint Propulsion Conference and Exhibit*, Huntsville, 2000, pp. 1-8.
- [23] John R. Brophy and Muriel Noca, "Electric Propulsion for Solar System Exploration," *Journal of Propulsion and Power*, vol. 14, no. 5, pp. 700-707, September-October 1998.
- [24] John R. Brophy, "Advanced Ion Propulsion Technology for Solar System Exploration," in *33rd AIAA/ASME/SAE/ASEE Joint Propulsion Conference and Exhibit*, Seattle, 1997, pp. 1-16.
- [25] V. V. Zhurin, H. R. Kaufman, and R. S. Robinson, "Physics of Closed Drift Thrusters," *Plasma Sources Science Technology*, pp. R1-R20, August 1999.
- [26] E. Y. Choueiri, "Fundamental Deifference Between the two Hall Thruster Variants," *Physics of Plasmas*, vol. 8, no. 11, pp. 5025-5033, November 2001.
- [27] Richard Wirz, Dan Goebel, Colleen Marrese, and Juergen Mueller, "Development of Cathode Technologies for a Miniature Ion Thruster," in *39th AIAA/ASME/SAE/ASEE Joint Propulsion Conference and Exhibit*, Huntsville, 2003, pp. 1-11.
- [28] AP*Tech. (2007, July) High Performance Elcetron Emitters (LaB6 CeB6). [Online]. <http://www.kore.co.uk/aptech.htm>
- [29] Kimball Physics, Inc. (n.d.) Kimball Physics Emitters (Cathodes, Filaments, Ion Sources) Product Guide. [Online]. http://www.kimphys.com/cathode/cath_prod.htm
- [30] Dan M. Goebel and Ron M. Watkins, "LaB6 Hollow Cathodes for Ion and Hall Thrusters," in *41st AIAA/ASME/SAE/ASEE Joint Propulsion Conference & Exhibit*, Tuscon, 2005, pp. 1-9.

- [31] Matthew T. Domonkos, Alec D. Gallimore, Jr., George J. Williams, and Michael J. Patterson, "Low-Current Hollow Cathode Evaluation," in *35th AIAA/ASME/SAE/ASEE Joint Propulsion Conference and Exhibit*, Los Angeles, 1999, pp. 1-25.
- [32] Michael J. Patterson, "Robust low-Cost Cathode for Commercial Applications," in *43rd AIAA/ASME/SAE/ASEE Joint Propulsion Conference and Exhibit*, Cincinnati, 2007, pp. 1-11.
- [33] Dennis L. Tilley, Gary F. Willmes, Roger M. Myers, and Richard D. Smith, "Flight Hollow Cathode for Hall Thruster Applications," in *34th AIAA/ASME/SAE/ASEE Joint Propulsion Conference and Exhibit*, Cleveland, 1998, pp. 1-10.
- [34] James E. Polk, "The Effect of Reactive Gases on Hollow Cathode Operation," in *42nd AIAA/ASME/SAE/ASEE Joint Propulsion Conference and Exhibit*, Sacramento, 2006.
- [35] Dustin J. Warner, Richard D. Branam, William A. Hargus, and Dan M. Goebel, "Low Current Cerium Hexaboride and Lanthanum Hexaboride Hollow Cathodes," in *46th AIAA Aerospace Sciences Meeting and Exhibit*, Reno, 2008, pp. 1-11.
- [36] L. W. Swanson and D. R. McNeely, "Work Functions of the (001) Face of the Hexaborides of Ba, La, Ce, and Sm," *Surface Sciences*, vol. 83, pp. 11-28, 1979.
- [37] D. L. Jacobson and E. K. Storms, "Work Function Measurement of Lanthanum - Boron Compounds," *IEEE Transactions on Plasma Science*, vol. PS-6, no. 2, June 1978.
- [38] Paul R. Davis, Mark A. Gesley, Gregory A. Schwind, Lynwood W. Swanson, and Joseph J. Hutta, "Comparison of Thermionic Cathode Parameters of Low Index Single Crystal Faces of LaB₆, CeB₆, and PrB₆," *Applied Surface Science*, vol. 37, pp. 381-394, April 1989.
- [39] H. E. Gallagher, "Poisoning of LaB₆ Cathodes," *Journal of Applied Physics*, vol. 40, no. 1, pp. 44-51, January 1969.

- [40] M. S. McDonald and A. D. Gallimore, "Cathode Positioning and Orientation Effects on Cathode Coupling in a 6-KW Hall Thruster," in *JANNAF 6th Modeling and Simulation/4th Liquid Propulsion/3rd Spacecraft Propulsion Joint Subcommittee Meeting*, Orlando, 2008.
- [41] Jason D. Sommerville and Lyon B. King, "Effect of Cathode Position on Hall-Effect Thruster Performance and Cathode Coupling Voltage," in *43rd AIAA/ASME/SAE/ASEE Joint Propulsion Conference and Exhibit*, Cincinnati, 2007, pp. 1-11.
- [42] Vladimir Kim, "Main Physical Features and Processes Determining the Performance of Stationary Plasma Thrusters," *Journal of Propulsion and Power*, vol. 14, no. 5, pp. 736-743, September-October 1998.
- [43] Jesse A. Linnell and Alec D. Gallimore, "Efficiency Analysis of a Hall Thruster Operating with Krypton and Xenon," *Journal of Propulsion and Power*, vol. 22, no. 6, pp. 1402-1412, November-December 2006.
- [44] Y. Raitses and J. Ashkenazy, "Propellant Utilization in Hall Thrusters," *Journal of Propulsion and Power*, vol. 14, no. 2, pp. 247-253, March-April 1998.
- [45] PHPK Technologies, *CBST 6.0 Scroll Compressor*. Columbus, OH: PHPK Technologies/CVI, n.d.
- [46] PHPK Technologies, *TorrMaster TM500 Cryopump Instruction Manual*. Columbus, OH: PHPK Technologies/CVI, n.d.
- [47] Kurt J. Lesker Company, *300 Series Convection Vacuum Gauge User's Manual*, 114th ed. Clairton, PA: Kurt J. Lesker Company, 2005.
- [48] Extorr, Inc., *Instruction Manual Extorr XT Series RGA*. New Kensington, PA: Extorr, 2006.
- [49] Kurt J. Lesker Company, *Series 979 Atmosphere to Vacuum Transducer Operation and Maintenance Manual*, 100014438th ed. Clairton, PA, 2003.
- [50] Busek Co. Inc., *BHT-HD-1500 Hall Thruster Operating and Maintenance Manual*. Natick, MA: Busek Co. Inc., 2008.

- [51] Russell H. Martin, Casey C. Farnell, and John Williams, "Direct and Remote Measurements of Plasma Properties nearby Hollow Cathodes," in *The 29th International Electric Propulsion Conference*, Princeton, 2005, pp. 1-26.
- [52] Jesse A. Linnell and Alec D. Gallimore, "Internal Langmuir Probe Mapping of a Hall Thruster with Xenon and Krypton Propellant," in *42nd AIAA/ASME/SAE/ASEE Joint Propulsion Conference and Exhibit*, Sacramento, 2006, pp. 1-18.
- [53] Dan M. Goebel, Kristina K. Jameson, Ron M. Watkins, and Ira Katz, "Hollow Cathode and Keeper-Region Plasma Measurements Using Ultra-Fast Miniature Scanning Probes," in *40th AIAA/ASME/SAE/ASEE Joint Propulsion Conference and Exhibit*, Fort Lauderdale, 2004, pp. 1-12.
- [54] Y. Raitses, N. J. Fisch, K. M. Ertmer, and C. A. Burlingame, "A Study of Cylindrical Hall Thruster for Low Power Space Applications," in *36th AIAA/ASME/SAE/ASEE Joint Propulsion Conference and Exhibit*, Huntsville, 2000, pp. 1-10.
- [55] James E. Pollard et al., "Ion Flux, Energy, and Charge-State Measurements for the BPT-4000 Hall Thruster," in *37th AIAA/ASME/SAE/ASEE Joint Propulsion Conference and Exhibit*, Salt Lake City, 2001, pp. 1-12.
- [56] Scientific Systems, *Smart Probe Automated Langmuir Probe Plasma Diagnostic Product Manual*. Kilbarrack, Ireland: Scientific Systems Ltd., n.d.
- [57] Casey Farnell, "AFIT Beam Profiler Overview," Colorado State University, Ft. Collins, Instrument Manual 2007.
- [58] Jared M. Ekholm, William A. Hargus, and C. William Larson, "Plume Characteristics of the Busek 600 W Hall Thruster," in *42nd AIAA/ASME/SAE/ASEE Joint Propulsion Conference and Exhibit*, Sacramento, 2006, pp. 1-10.
- [59] Casey Farnell and John D. Williams, "Faraday Probe Operating Manual," Colorado State University, Ft. Collins, Instrument Manual 2007.
- [60] Casey Farnell and John D. Williams, "ExB Probe Operating Manual," Colorado State University, Ft. Collins, Instrument Manual 2007.

- [61] Yassir Azziz, "Experimental and Theoretical Characterization of a Hall Thruster Plume," Massachusetts Institute of Technology, Cambridge, PhD Dissertation 2007.
- [62] Brian E. Beal, "Clustering of Hall Effect Thrusters for High-Power Electric Propulsion Applications," University of Michigan, Ann Arbor, PhD Dissertation 2004.

Vita

LCDR John E. Rotter, USN is a native of St. Louis, Missouri. He graduated from Iowa State University with a Bachelor of Science degree in Aerospace Engineering in 1995 and was commissioned an Ensign in the United States Navy. Following flight school and his designation as a Naval Aviator, he completed two operational tours flying the P-3C “Orion” aircraft in numerous theaters. He also served for one tour as a primary instructor pilot in the T-34C “Turbo Mentor”.

In 2007 LCDR Rotter was redesignated as an Aerospace Engineering Duty Officer. Following his graduation from AFIT, LCDR Rotter will begin working at the National Reconnaissance Office.

LCDR Rotter is married and has three children. He has been published in *Approach* magazine, which is published by the Naval Safety Center in Norfolk, Virginia.

REPORT DOCUMENTATION PAGE				Form Approved OMB No. 074-0188	
<p>The public reporting burden for this collection of information is estimated to average 1 hour per response, including the time for reviewing instructions, searching existing data sources, gathering and maintaining the data needed, and completing and reviewing the collection of information. Send comments regarding this burden estimate or any other aspect of the collection of information, including suggestions for reducing this burden to Department of Defense, Washington Headquarters Services, Directorate for Information Operations and Reports (0704-0188), 1215 Jefferson Davis Highway, Suite 1204, Arlington, VA 22202-4302. Respondents should be aware that notwithstanding any other provision of law, no person shall be subject to a penalty for failing to comply with a collection of information if it does not display a currently valid OMB control number.</p> <p>PLEASE DO NOT RETURN YOUR FORM TO THE ABOVE ADDRESS.</p>					
1. REPORT DATE (DD-MM-YYYY) 26-03-2009		2. REPORT TYPE Master's Thesis		3. DATES COVERED (From - To) March 2008 - March 2009	
4. TITLE AND SUBTITLE An Analysis of Multiple Configurations of Next-Generation Cathodes In A Low Power Hall Thruster				5a. CONTRACT NUMBER	
				5b. GRANT NUMBER	
				5c. PROGRAM ELEMENT NUMBER	
				5d. PROJECT NUMBER 09-173	
6. AUTHOR(S) Rotter, John E., LCDR, USN				5e. TASK NUMBER	
				5f. WORK UNIT NUMBER	
7. PERFORMING ORGANIZATION NAMES(S) AND ADDRESS(S) Air Force Institute of Technology Graduate School of Engineering and Management (AFIT/ENY) 2950 Hobson Way, Building 640 WPAFB OH 45433-8865				8. PERFORMING ORGANIZATION REPORT NUMBER AFIT/GA/ENY/09-M07	
9. SPONSORING/MONITORING AGENCY NAME(S) AND ADDRESS(ES) Air Force Research Lab/Space and Missile Propulsion Div. Att: Mr. Michael Huggins 1 Ara Rd. Edwards, AFB CA 93524				10. SPONSOR/MONITOR'S ACRONYM(S) AFRL/RZS	
				11. SPONSOR/MONITOR'S REPORT NUMBER(S)	
12. DISTRIBUTION/AVAILABILITY STATEMENT APPROVED FOR PUBLIC RELEASE; DISTRIBUTION UNLIMITED.					
13. SUPPLEMENTARY NOTES					
14. ABSTRACT <p>The research presented here is an effort to integrate an existing hollow cathode design with a low power production Hall thruster in multiple geometries. Both externally- and internally-mounted cathodes were fabricated and operated in conjunction with a Busek BHT-1500 Hall thruster. Three insert materials were evaluated; Cerium Hexaboride (CeB6), Lanthanum Hexaboride (LaB6), and impregnated tungsten. The thruster was operated at a single operating condition for all testing. The operating specifications for the discharge were 300 V and 2.25 A, giving a total power of 675 W.</p> <p>The boride-based cathodes were tested in both geometries while the tungsten-based cathode was only tested in an external configuration. A Faraday probe was used to measure current density in the plume and a single Langmuir probe was used to characterize the plasma. The charge state of the ions was measured with an ExB probe. All assembly and testing occurred at the Air Force Institute of Technology's (AFIT) Space Propulsion Analysis and System Simulation (SPASS) lab facility.</p> <p>The thruster's performance with the externally-mounted boride-based cathodes installed demonstrated the highest levels of efficiency and performance. The thruster's performance with the tungsten-based cathode installed was slightly less than with the externally-mounted boride-based cathodes. The lowest thruster performance occurred with the internally-mounted cathodes installed. The primary loss mechanism observed was an increase in multiply-ionized propellant with the internally-mounted cathodes.</p>					
15. SUBJECT TERMS SPACE PROPULSION/HALL THRUSTERS/CATHODES					
16. SECURITY CLASSIFICATION OF:			17. LIMITATION OF ABSTRACT	18. NUMBER OF PAGES	19a. NAME OF RESPONSIBLE PERSON
a. REPORT	b. ABSTRACT	c. THIS PAGE			Richard D. Branam, Lt. Col., USAF
U	U	U	UU	151	19b. TELEPHONE NUMBER (Include area code) (937) 255-6565x7485 (richard.branam@afit.edu)